Journal of the Meteorological Society of Japan

EARLY ONLINE RELEASE

The DOI for this manuscript is

DOI:10.2151/jmsj.2024-004

J-STAGE Advance published date: November 2nd, 2023

The final manuscript after publication will replace the preliminary version at the above DOI once it is available.

The JRA-3Q Reanalysis

Yuki KOSAKA[1]**, Shinya KOBAYASHI**

Numerical Prediction Development Center, JMA, Tsukuba, Japan

Yayoi HARADA, Chiaki KOBAYASHI, Hiroaki NAOE

Meteorological Research Institute, JMA, Tsukuba, Japan

Koichi YOSHIMOTO, Masashi HARADA, Naochika GOTO

Japan Meteorological Agency, Tokyo, Japan

Jotaro CHIBA

Numerical Prediction Development Center, JMA, Tsukuba, Japan

Kengo MIYAOKA[2]**, Ryohei SEKIGUCHI**

Japan Meteorological Agency, Tokyo, Japan

Makoto DEUSHI, Hirotaka KAMAHORI, Tosiyuki NAKAEGAWA

Meteorological Research Institute, JMA, Tsukuba, Japan

Taichu Y. TANAKA, Takayuki TOKUHIRO[2]

Numerical Prediction Development Center, JMA, Tsukuba, Japan

Yoshiaki SATO[3], Yasuhiro MATSUSHITA, Kazutoshi ONOGI[4]

Japan Meteorological Agency, Tokyo, Japan

February 1, 2023

----

1) Corresponding author: Yuki Kosaka, Office of Earth System Modeling, Numerical Prediction Development Center, JMA, 1-1 Nagamine, Tsukuba-shi, Ibaraki 305-0052 JAPAN
Email: yuki-kosaka@met.kishou.go.jp
Tel: +81-29-853-8562
2) Present affiliation: Meteorological Research Institute, JMA, Tsukuba, Japan
3) Present affiliation: Numerical Prediction Development Center, JMA, Tsukuba, Japan
4) Present affiliation: Research Center for Advanced Science and Technology, the University of Tokyo, Tokyo, Japan

Abstract

The Japan Meteorological Agency (JMA) has developed the third Japanese global atmospheric reanalysis, the Japanese Reanalysis for Three Quarters of a Century (JRA-3Q). The objective of JRA-3Q is to improve quality in terms of issues identified in the previous Japanese 55-year Reanalysis (JRA-55) and to extend the reanalysis period further into the past. JRA-3Q is based on the TL479 version of the JMA global Numerical

Weather Prediction (NWP) system as of December 2018 and uses results of developments in the operational NWP system, boundary conditions, and forcing fields achieved at JMA since JRA-55. It covers the period from September 1947, when Typhoon Kathleen brought severe flood damage to Japan, and uses rescued historical observations to extend its analyses backwards in time about 10 years earlier than JRA-55. This paper describes the data assimilation system, forecast model, observations, boundary conditions, and forcing fields used to produce JRA-3Q as well as the basic characteristics of the JRA-3Q product. The initial quality evaluation revealed major improvements from JRA-55 in the global energy budget and representation of tropical cyclones (TCs). One of the major problems in JRA-55—global energy imbalance with excess upward net energy flux at the top of the atmosphere and at the surface—has been significantly reduced in JRA-3Q. Another problem—a trend of artificial weakening of TCs—has been resolved through the use of a method that generates TC bogus based on the JMA operational system. There remain several problems such that volcanic-induced stratospheric warming is smaller than expected. This paper discusses the causes of such problems and possible solutions in future reanalyses.

Keywords reanalysis, data assimilation, numerical weather prediction

1. Introduction

The objective of long-term reanalysis is to produce a homogeneous, high-quality climate dataset spanning at least the previous several decades. Reanalysis products are widely used in research in academic fields such as meteorology, climatology, and oceanography, as well as in applied fields such as agricultural meteorology and renewable energy. The products are also used by the Japan Meteorological Agency (JMA) as fundamental datasets for investigating past weather disasters, improving seasonal forecasts, and analyzing extreme weather events. Major numerical weather prediction (NWP) centers and meteorological research institutes have made an effort to create and improve long-term reanalyses (for a detailed list, see https://reanalyses.org/). Recent state-of-the-art atmospheric reanalyses include the fifth generation of the European Centre for Medium-Range Weather Forecasts (ECMWF) atmospheric reanalysis (ERA5; Hersbach et al. 2020), the Modern-Era Retrospective Analysis for Research and Applications, version 2 (MERRA-2; Gelaro et al. 2017), and the National Centers for Environmental Prediction (NCEP) Climate Forecast System Reanalysis (CFSR; Saha et al. 2014). Over the course of generations, the quality and usefulness of reanalysis products have steadily improved because of increases of their resolution and extension of the period of time they cover, upgrades of their data-assimilation methods, improvement in availability and quality of past observations, and improvement of the quality of their boundary conditions and atmospheric forcing fields. However, to create homogeneous, high-quality reanalysis products remains a major challenge because there have been many abrupt changes in observing systems and large uncertainties exist in observations, boundary conditions, and atmospheric forcing fields in addition to inadequate preparation of past observations. There is thus a need for further improvement (see, for example, Buizza et al. 2018; Chen et al. 2021).

In Japan, the JMA and the Central Research Institute of Electric Power Industry developed the first long-term reanalysis product, the Japanese 25-year Reanalysis (JRA-25; Onogi et al. 2007), and the JMA developed the second reanalysis product, the Japanese 55-year Reanalysis (JRA-55; Kobayashi et al. 2015, Harada et al. 2016). The comprehensive improvements in JRA-55 includes elimination of the cold bias in the lower stratosphere, which was one of the major problems in JRA-25, as well as improvements in the representation of the surface downward longwave radiation flux and the temporal homogeneity of the temperature analysis fields. Remaining issues include a warm bias in the upper troposphere, a cold bias in the lower troposphere, a negative bias of precipitable water in convective regions, excessive precipitation over the tropics, a large upward imbalance in the global mean net energy fluxes at the top of the atmosphere and at the surface, and an unrealistic long-term trend in the intensity of analyzed tropical cyclones (TCs). In addition, an intercomparison between a JRA-55 sub-product assimilating conventional observations only (JRA-55C, Kobayashi et al. 2014) and another sub-product of JRA-55C with high-resolution sea surface temperature (SST) data (JRA-55CHS, Masunaga et al. 2018) has shown that the influence of steep horizontal gradients of SST along the western boundary currents can reach into the middle and upper troposphere. These results imply that use of high-resolution SST datasets would contribute to deepening understanding of the nature of frontal-scale, air-sea interactions (Masunaga et al. 2018).

The Japanese Reanalysis for Three Quarters of a Century (JRA-3Q) is the third long-term reanalysis product developed by the JMA to improve the quality and extend the period of long-term reanalysis products by addressing these issues in JRA-55. JRA-3Q covers the period from September 1947 to the present, extending back in time about 10 years earlier than JRA-55, and uses results of developments in the operational global NWP system, boundary conditions, and forcing fields achieved at JMA since JRA-55. Regarding observations, global, regional, and national governmental and non-profit organizations have rescued, collected, and digitized historical observations in recent years (Stuber et al., 2021), and meteorological and satellite centers have reprocessed past satellite observations using state-of-the-art algorithms to produce high-quality, homogeneous satellite products. The enrichment of observations through these data-rescue activities and satellite data reprocessing has also helped to improve the JRA-3Q product.

This paper describes the overall JRA-3Q specifications and its basic characteristics: we explain the data assimilation system of JRA-3Q in Section 2, the forecast model in Section 3, and the boundary conditions and atmospheric forcing in Section 4. Section 5 describes the data sources, quality control of the observations used, and the method of data selection in JRA-3Q. Section 6 describes the JRA-3Q streams. Section 7 discusses the basic performance of the data assimilation system. Section 8 focuses on two major improvements in quality over the JRA-55 product, the global energy budget and the representation of TCs. Section 9 describes the basic performance of JRA-3Q products. Conclusions are presented in Section 10. The meanings of abbreviations used in this paper are given in Appendix A, and the sources of observational data for JRA-3Q are listed in Appendix B.

2. Data assimilation system

The JRA-3Q data assimilation system performs the components of global atmospheric analyses and land surface/snow-depth/screen-level analyses, as illustrated in Fig. 1, which shows the flow of data between components. The atmospheric, screen-level, and land surface analyses are performed every 6 hours (00, 06, 12, 18 UTC), and the snow-depth analysis is performed daily at 18 UTC.

The forecast model uses the previous atmospheric and land surface analyses as the initial condition for the forecast, and a model integration starting from that initial condition produces a background field, which is the best estimate of the current state prior to using observations. Then atmospheric/land surface/snow-depth/screen-level analyses are performed separately using the background field and observations. The resulting atmospheric/land surface analyses are used as the initial condition for the next forecast cycle. Here, 'first guess' is also used as an interchangeable term with 'background'.

Table 1 shows an overview of the JRA-3Q data assimilation system, including a comparison with JRA-55. The JRA-3Q data assimilation system is based on a low-resolution (TL479) version of the JMA’s global data assimilation system as of December 2018 (JMA 2019). JRA-3Q benefits from a decade of developments in the operational NWP system since JRA-55 as well as from an increase in resolution compared with JRA-55 made possible by a new supercomputer system with high performance resources that has been in operation since June 2018.

2.1 Atmospheric analysis

The atmospheric analysis component of the JRA-3Q data assimilation system uses four-dimensional variational analysis (4D-Var). To improve computational efficiency, an incremental method (Courtier et al. 1994) is used, wherein the analysis increment, modification amount for first guess, is first calculated by performing one inner loop minimization at a relatively low resolution (TL319L100) and then added to the first guess at the original resolution (TL479L100). The analysis increments are determined in such a way that the cost function defined by equation (2.1.1) is minimized (JMA 2019):

$$J(\Delta \boldsymbol{z}_0) = \frac{1}{2}\Delta \boldsymbol{z}_0{}^T \mathbf{B}^{-1} \Delta \boldsymbol{z}_0 + \frac{1}{2}\sum_{i=1}^{n} (\mathbf{H}_i \Delta \boldsymbol{z}_i - \boldsymbol{d}_i)^T \mathbf{R}_i^{-1} (\mathbf{H}_i \Delta \boldsymbol{z}_i - \boldsymbol{d}_i) + J_C,$$

$$\boldsymbol{d}_i = \boldsymbol{y}_i^O - H_i \boldsymbol{z}_i^b,$$

$$\Delta\boldsymbol{z}_{i+1} = \mathbf{M}_i \Delta\boldsymbol{z}_i \quad (i = 0, \cdots, n-1), \qquad (2.1.1)$$

where $\Delta\boldsymbol{z}$ is the analysis increment, $\boldsymbol{y}^O$ is a vector containing all observations, $\boldsymbol{z}^b$ is the background field, **B** is the background error covariance matrix, **R** is the observation error covariance matrix, $\mathbf{M}$ is the tangent linear model of the nonlinear forecast model, *H* and **H** are the nonlinear observation operator and its tangent linear operator, J_C is the penalty term for suppressing gravity waves, and the subscript i and n are the timeslot and final timeslot, respectively. Note that observations are organized in six time slots with intervals of 0.5 hours for the first slot, 1.5 hours for the last slot, and 1 hour for the others.

$\boldsymbol{z}$ contains the atmospheric state vector as well as parameters for the variational bias correction (Derber and Wu 1998; Dee and Uppala 2009; JMA 2019) applied to satellite radiances. In JRA-3Q, as in JRA-55, variational bias correction is applied to all satellite radiances, but not to other observations.

a. Background error covariances

The background error covariance matrix is based on the same static background error covariance model as the one used in JRA-55, which transforms analysis variables into control variables, i.e., relative vorticity, unbalanced divergence, unbalanced temperature and surface pressure, and the logarithm of specific humidity in the spectral space on model layers, to reduce correlations among variables (JMA 2019). This background error covariance matrix is basically the same as the matrix used in the JMA operational system as of December 2018, which was statistically calculated from the difference between the 24-hour and 48-hour forecasts at the same valid time for the year 2015 using the National Meteorological Center (NMC) method (Parrish and Derber 1992).

Observations available for JRA-3Q decrease as they go back in time, and consequently errors in the background fields increase. For periods (i), (ii), and (iii), defined below, the background error variances of the control variables, except for the logarithm of specific humidity, are increased by (i) 155%, (ii) 50%, and (iii) 11%, respectively, to account for the increased error in the background fields:

(i) before 1958, when the international network of regular radiosonde observations was established,

(ii) between 1958 and 1972, before the introduction of satellite observations, and

(iii) between January 1973 and July 1998, a time interval during which old-generation satellite observing systems were used.

These scaling factors were obtained by comparing background errors estimated from full observing system experiments with those estimated from experiments assimilating (i) conventional data, limited to once a day at 12 UTC for upper-air observations, and tropical cyclone boguses (TCBs) only, (ii) conventional data with no limitation and TCBs only, and (iii) all observations but radiances from the Advanced Microwave Sounding Units (AMSUs), respectively. These experiments were all conducted for conditions in August 1999 and

January 2000. Background errors were estimated using the method of Desroziers et al. (2005) on observation-minus-background quantities (background departures) and observation-minus-analysis quantities (analysis departure) of radiosonde temperatures and winds from these experiments. It should be noted that these scaling factors do not affect correlation lengths of background error covariances.

b. Radiative transfer model for satellite radiances

Satellite radiances are assimilated by using a fast radiative transfer model, Radiative Transfer for the TIROS Operational Vertical Sounder (RTTOV) version 10.2 (Saunders et al. 2012). The calculation accuracy of RTTOV version 10.2 has generally been improved compared with that of RTTOV version 9.3 (Saunders 2008), which was used in JRA-55, because its resolution of vertical layers is higher and its line-by-line transmittance database used for training the fast radiative transfer model has been refined. Changes in the concentration of greenhouse gases (carbon dioxide, and for some instruments, methane and nitrous oxide as well) over time are considered in radiance calculations for all infrared instruments, whereas in JRA-55, carbon dioxide is treated as a variable only for the Vertical Temperature Profile Radiometer (VTPR). Land surface emissivity atlases (Saunders et al. 2012) are used for calculating radiances from AMSU-A, AMSU-B, the Microwave Humidity Sounder (MHS), the Advanced Technology Microwave Sounder (ATMS), and geostationary meteorological satellites (except for the Geostationary Meteorological Satellite [GMS] and

Multi-functional Transport Satellite [MTSAT]), in contrast to a fixed emissivity of 0.9 in JRA-55. For the other instruments, a fixed land surface emissivity of 0.9 is used in both JRA-3Q and JRA-55.

2.2 Surface analysis

a. Screen-level analysis

Specification of the screen-level analysis is the same in JRA-3Q and JRA-55 (Kobayashi et al. 2015). Screen-level diagnostic variables (such as 2-m air temperature, relative humidity, and 10-m wind) are analyzed separately from the global atmospheric analysis by using univariate 2-D optimal interpolation (2D-OI). Note that the screen-level analysis fields are not used for the subsequent cycles.

b. Land surface analysis

The initial condition for land surface is given by the most recent land surface forecast fields from the atmospheric model, except that a snow-depth analysis field is incorporated into the land surface analysis at 18 UTC every day.

In JRA-55, land surface analysis fields are produced by driving the JMA Simple Biosphere (SiB) model separately from the atmospheric model (an offline mode) instead of using outputs from the SiB model built into the atmospheric model (an online mode) (Kobayashi et al. 2015). A potential advantage of using an offline model is that this framework has the flexibility of using observations as atmospheric forcings and can generate more accurate background fields for land surface analysis than forcings from an atmospheric model. However, this advantage is not actually exploited in JRA-55. The use of an online model in JRA-3Q enables interactions between atmospheric and land surface processes at every model time step and has an advantage in providing more consistent background fields between the atmosphere and land surface.

c. Snow depth analysis

The first guess of snow depth is generated from the snow depth of the model or the satellite snow cover (Fig. 2), and then in situ observations of snow depth are assimilated using 2D-OI. Although this procedure is similar to that used in JRA-55 (Kobayashi et al. 2015), the following two problems—unrealistic analysis near coasts and unintentional increment due to satellite data bias— were resolved.

The first problem is due to a programming defect in the interpolation process of snow depth data in coastal areas (JMA 2015). This defect was fixed to prevent a similar problem in JRA-3Q. Also, a safeguard has been introduced by setting the upper limit of the snow depth analysis to 5 m.

The second problem is that positive increments tend to occur in a region where the satellite snow cover has a negative bias (e.g., near coasts) because the satellite snow cover is not assimilated in the 2D-OI but is instead used to generate the first guess. Those positive increments extend to the surrounding area, where the satellite snow cover does not have a negative bias. The result is an excessive snow depth analysis in that area. To overcome this problem, the method of generating the first guess of snow depth in JRA-3Q has been modified by checking consistency with in situ snow depth observations (Fig. 2).

3. Forecast model

Table 2 compares specifications of the forecast models used for JRA-55 and JRA-3Q. Substantial improvements in parameterizations of physical processes since JRA-55 have led to reduced systematic errors in the radiation budget, surface sensible and latent heat fluxes, and distribution of precipitation. Major changes from the forecast model used in JRA-55 are described in the following subsections.

3.1 Radiation

a. Longwave radiation

The longwave spectrum is divided into 11 bands, in contrast to 9 bands in JRA-55, and then the radiative transfer equation is solved with the two-stream absorption approximation method. In JRA-55, the radiative transfer equation is solved on the assumption that there is no scattering in the atmosphere (broad-band flux emissivity method with a diffusivity approximation) (JMA 2007). The change from the broad-band flux emissivity method to the two-stream absorption approximation method has substantially reduced computation time (Yabu 2013). Calculations of longwave radiation are performed every hour, in contrast to every three hours in JRA-55 (JMA 2019).

For transmission functions, JRA-3Q uses the correlated *k*-distribution method (Fu and Liou 1992) to calculate the absorption bands that substantially contribute to cooling in the middle atmosphere (the 15-μm carbon dioxide band, the 9.6-μm ozone band, and major line absorption bands of water vapor), which reduces computational cost compared to a pre-computed table look-up method (Chou and Kouvaris 1991) used in JRA-55. For other absorption bands, both JRA-3Q and JRA-55 use the *k*-distribution method with scaling approximation (Chou et al. 2001).

The continuous absorption of water vapor is parameterized based on the Mlawer-Tobin-Clough-Kneizys-Davies continuous absorption band model (MT_CKD, Clough et al. 2005), which is the same as the model used in JRA-55. In JRA-3Q, however, the *k*-distribution parameters are calculated from the absorption coefficients based on the MT_CKD model, and then the *k*-distribution method is applied (JMA 2019). Both JRA-3Q and JRA-55 consider the atmosphere to be inhomogeneous and use scaling parameters from Zhong and Haigh (1995).

b. Cloud radiation

In shortwave radiation processes, cloud overlap between different vertical layers is represented assuming the maximum-random overlap (Geleyn and Hollingsworth 1979), in contrast to the random overlap used for JRA-55. The shortwave radiation flux in each column is calculated by the Practical Independent Column Approximation (PICA, Nagasawa 2012) method, which is a simplified, low-computational-cost version of the Independent Column Approximation (ICA) approach based on Collins (2001) (JMA 2019). In longwave radiation processes, cloud overlap between different vertical layers is represented assuming the maximum-random overlap in both JRA-3Q and JRA-55 (JMA 2019).

Cloud properties used in the radiation scheme, such as the cloud cover and cloud water content, account for both stratiform and convective clouds, whereas in JRA-55, such cloud properties account for only stratiform clouds. Cloud properties of stratiform clouds are specified by the cloud scheme and those of convective clouds are diagnosed using the upward convective mass flux calculated in the cumulus convection scheme (JMA 2019).

The cloud optical properties for liquid droplets are parameterized following Lindner and Li (2000) for longwave radiation processes and Dobbie et al. (1999) for shortwave radiation processes, whereas in JRA-55, such cloud properties are parameterized following Hu and Stamnes (1993) for longwave radiation processes and Slingo (1989) for shortwave radiation processes. These refinements have led to improved parameterizations that give a better fit to exact Mie calculations.

In JRA-55, the effective radii of water cloud droplets were based on satellite retrievals and fixed at 10 μm over land and 13 μm over the sea (JMA 2007). However, Nakajima et al. (2010) and Painemal and Zuidema (2011) have pointed out that those satellite retrievals were overestimates. In JRA-3Q, the effective radius is parametrized by a method derived from aircraft observations (Martin et al. 1994), which reduces the overestimation (JMA 2019).

c. Aerosols

Five types of aerosols (sulfate, black carbon, organic carbon, sea salt, and mineral dust) are considered to account for the direct effects of aerosols (Yabu et al. 2017). The three-dimensional monthly mean climatology of aerosol mass concentration was derived from a calculation that makes use of the Model of Aerosol Species in the Global Atmosphere (MASINGAR; Tanaka et al. 2003), and the optical properties for each aerosol type and particle size were pre-computed via a Mie scattering calculation. In JRA-55, the direct effect of aerosols is taken into account by using two vertical profiles of aerosols from the World Meteorological Organization (WMO) (1986), i.e., the tropospheric aerosol profiles for an average rural-continental region (CONT-I) over land and for a relatively clear maritime region (MAR-I) over the sea.

The concentration of each aerosol type was adjusted with a two-dimensional monthly aerosol optical depth climatology based on the Moderate Resolution Imaging Spectroradiometer (MODIS), the Multiple Angle Imaging Spectroradiometer (MISR), and observations made by the Ozone Monitoring Instrument (OMI) (JMA 2019), which is a treatment similar to that in JRA-55 (JMA 2013).

3.2 Cumulus convection

The JRA-3Q forecast model uses a spectral mass-flux convective parameterization scheme based on Arakawa and Schubert (1974) and Moorthi and Suarez (1992) in a way similar to the use of that scheme in JRA-55. Prognostic closure based on Randall and Pan (1993) is used in JRA-3Q, although many modifications have been made to the original scheme. In addition, a triggering mechanism based on the dynamic convective available potential energy (CAPE) generation rate (DCAPE; Xie and Zhang 2000) concept is adopted to suppress excessive convective activity. Convective downdraft, convective momentum transport, and mid-level convection are also included in the scheme (JMA 2019).

In the forecast model used in JRA-3Q, the introduction of the conversion from cloud water content to precipitation in the updraft provides an appropriate height at which precipitation is produced and contributes to reducing the warm bias in the upper troposphere. Formulation for the melting and re-evaporation of precipitation has been refined to enables a more realistic representation of the melting layer, which contributes to the reproducibility of the distribution of cloud-top heights of cumulus clouds and tropical circulation. In addition, the improvement of the convective updraft model below the cloud base increases the rate of heating and thereby reduces the cold bias in the tropical mid-troposphere (Yonehara et al. 2014, 2017, 2018).

3.3 Clouds

A diagnostic scheme proposed by Smith (1990) is used for the calculation of large-scale condensation. The scheme assumes a probability density function (PDF) for sub-grid-scale fluctuations of total water content (water vapor and cloud water). In JRA-55, the width of the PDF was adjusted as a function of the upward mass flux derived from the cumulus convection scheme. As a result, the width of the fluctuation was overestimated, which led to locally unnatural precipitation. JRA-3Q has eliminated this adjustment of the width of the fluctuation.

Furthermore, in JRA-55, not only stratiform precipitation produced in the cloud scheme but also convective precipitation produced in the cumulus convection scheme trapped cloud water and cloud ice in the merging process of precipitation. This treatment was inconsistent because neither scheme considered the overlap between stratus and cumulus clouds, but it proved difficult to abolish this treatment without worsening the prediction skill. In JRA-3Q, the effect of merging precipitation from the cumulus convection scheme has been abolished because of the improvements in other physical processes. As a result, a more appropriate vertical profile of heating rates is achieved, and the dry bias in the middle troposphere is reduced in JRA-3Q.

To represent oceanic stratocumulus clouds in the forecast model, both JRA-55 and JRA-3Q use a scheme based on the strength of the inversion layer estimated from grid point values (Kawai and Inoue 2006). In JRA-3Q, a trigger condition of relative humidity has been added to the scheme to suppress cloud overgeneration due to unintended triggering

(Shimokobe 2012).

In addition, the excessive velocity of falling cloud ice has been corrected, and the dependence on the time integration interval has been reduced in calculating the amount of cloud ice converted to snowfall in JRA-3Q. The result is more realistic values of them in JRA-3Q than in JRA-55. Furthermore, JRA-3Q represents cooling more realistically by refining the re-evaporation process from precipitation to vapor and the melting process from snowfall to precipitation (JMA 2019).

3.4 Boundary layer

The surface fluxes were formulated as bulk formulae in accord with Monin-Obukhov similarity theory, and the equations are solved using the stability functions of Beljaars and Holtslag (1991), whereas in JRA-55, the equations are solved using transfer coefficients based on the stability functions proposed by Louis et al. (1982) (JMA 2007). It has been pointed out that the scheme of Louis et al. (1982) overestimates the transfer coefficients under stable conditions (Beljaars and Holtslag 1991).

Vertical turbulent transports are parameterized by a hybrid method that includes closure of turbulent kinetic energy and a scheme of eddy diffusivity type. The turbulent kinetic energy scheme used is the level-2 turbulence closure scheme of Mellor and Yamada (1974, 1982), and the scheme of eddy diffusivity type uses stability functions based on Han and Pan (2011) (Yonehara et al. 2014, 2017; JMA 2019). In JRA-55, vertical turbulent transports are parameterized based on the level-2 turbulence closure scheme of Mellor and Yamada (1974, 1982) (JMA 2007) and adjusted by setting a lower limit on the diffusion coefficients to mitigate positive feedbacks between buoyant stability and turbulent transport under strongly stable conditions. This lower limit was removed in JRA-3Q.

Screen-level quantities such as 2-m air temperature and humidity as well as 10-m wind above the surface are diagnosed over the sea by vertical interpolation on the assumption that the variables are linear functions of the logarithm of height, but over land they are diagnosed by considering vertical stability. The latter is an update from JRA-55, which uses the same stability-independent interpolation as that used over the sea.

3.5 Non-orographic gravity wave drag

JRA-3Q uses a scheme proposed by Scinocca (2003), in which the momentum-conserving vertical propagation and dissipation processes of momentum are parameterized. The dissipation processes are represented by critical-level filtering and amplitude saturation (JMA 2019). This scheme is more sophisticated than the one in JRA-55, which simply applies Rayleigh friction for layers above 50 hPa (JMA 2013).

3.6 Land surface

The forecast model in JRA-3Q uses land surface processes based on the SiB model (Sellers et al. 1986; Sato et al. 1989a, 1989b) with seven layers for both soil temperature and soil moisture, in contrast to one layer for soil temperature and three layers for soil moisture in JRA-55. In this process, soil temperature is predicted based on the principle of energy conservation and Fourier's law of heat conduction, in contrast to a force-restore method (Deardorff 1978) used in JRA-55. This revision has improved energy conservation in the soil and the phase lag between the surface air temperature and soil temperature during the diurnal cycle. Soil moisture is calculated using a water balance equation in both JRA-3Q and JRA-55.

A new snow scheme with up to four layers has also been introduced that takes into consideration thermal conductivity and heat capacity in addition to albedo (Yonehara et al. 2017), whereas in JRA-55, snow cover is represented simply as ice on grass and bare soil. Other land surface characteristics, such as the albedo of bare soil and distribution of types of vegetation have also been updated (Yonehara et al. 2014, 2018).

4. Boundary conditions and forcing fields

4.1 SST

The SST specified as the lower boundary condition of the forecast model is the Merged Satellite and In-Situ Data Global Daily Sea Surface Temperature (MGDSST; Kurihara et al. 2006) with a resolution of 0.25° based on satellite observations since June 1985 and the Centennial In Situ Observation-based Estimates of the Variability of SSTs and Marine Meteorological Variables Version 2 (COBE-SST2; Hirahara et al. 2014) with a resolution of 1° based on in situ observations until May 1985. To enable evaluation of changes in product characteristics following the switch from COBE-SST2 to MGDSST, a sub-product using COBE-SST2 (JRA-3Q-COBE) was also produced for the period from June 1985 to December 1990.

Although JRA-55 used COBE-SST (Ishii et al. 2005), JRA-3Q uses COBE-SST2, which has a new method to correct observations for bias. To improve the representation of spatiotemporal variability of SST in areas where in situ observations are scarce, COBE-SST2 employs a reconstructive method using an empirical orthogonal function defined from the SST analysis based on in situ observations and satellite observations (1961–2005).

In MGDSST, after multiple satellite observations are divided into specific spatiotemporal scales using a Gaussian filter, an optimal interpolation method is used to obtain the SST analysis for each scale, and then the final SST product is obtained by combining them. Note that the in situ observations are used only for bias correction of the satellite observations. Because the MGDSST has a higher resolution (0.25°resolution) than the COBE-SST (1° resolution), steep horizontal gradients of SST, such as the gradients near the western boundary currents, can be represented more realistically with MGDSST than with COBE-SST.

In addition, it should be noted that there is special data processing in the lake area, as described in subsection 9.5.

4.2 Sea ice

The sea ice concentration (SIC) analysis used in the preparation of each SST dataset presented in Subsection 4.1 is specified as a lower boundary condition of the forecast model.

In COBE-SST2, the SIC analysis was carried out by combining the NASA sea ice estimation algorithm (Cavalieri et al. 1984, 1991) and the bootstrap method (Comiso et al. 1997) for the period since 1978, when satellite observations are available. Because satellite observations are not available prior to 1978, the SIC analysis in the Arctic for that time uses the SIC products from Walsh and Chapman (2001) corrected by the SIC climatology from satellite observations (1979–1988), and the analysis in the Antarctic region uses the satellite-observed SIC climatology. While COBE-SST, which is adopted in JRA-55, used SIC products (Walsh and Chapman 2001) that are not sufficiently represented in some ocean regions, the SIC in the Sea of Okhotsk has been filled with satellite-observed SIC climatology in COBE-SST2.

MGDSST uses the SIC analysis created for COBE-SST, which is the same as that used for JRA-55 (Kobayashi et al. 2015) and based on microwave imager sea ice retrievals by Matsumoto et al. (2006).

To use the analysis of COBE-SST2 and MGDSST as the lower boundary for the forecast model, it is necessary to convert the analysis grid into the grid of the forecast model. If the extent of sea ice before the conversion reaches the sea-land boundary, the extent of sea ice after the conversion may not reach the sea-land boundary because of slight differences of the sea-land grid between the ocean analysis and the forecast model. To resolve this problem, the sea grid adjacent to the land grid is extrapolated from the SIC analysis.

In the forecast model, the sea ice process is represented by a model that deals with ice heat transfer by discretizing the ice slab of 1.5 m thickness into four vertical layers. In JRA-55, the sea ice process is represented by a one-layer model with a 2-m-thick ice slab, but the temperature of the top 0.05 m of ice is the only prognostic variable. Consequently, in JRA-55, most of the heat exchanged with the atmosphere is used to increase or decrease the temperature of the top 0.05 m of ice. This problem was solved with the multi-layer model in JRA-3Q.

The model used in JRA-3Q accounts for tiling between sea ice and open water, which is an update from the previous model in JRA-55 that assumes no mixed states within a grid—completely covered by sea ice or ice-free, categorized with a sea-ice concentration threshold of 55%.

The surface-roughness lengths over sea ice are 1.0×10^{-3} for momentum and 5.0×10^{-4} m for heat (Yonehara et al. 2017; JMA 2019). The latter was changed from the value in JRA-55, which was set to the same as for momentum (JMA 2013).

4.3 Ozone

The ozone distributions that are used in the JRA-3Q (JRA-3Q Ozone) were produced separately from the JRA-3Q data assimilation system. The JRA-3Q Ozone data are required as the forcing field for the radiation processes in the forecast model and as input data for the radiative transfer calculations in the data assimilation of satellite radiances. The JRA-3Q Ozone data were calculated using the TL159L64-resolution version of the global chemistry climate model (CCM) developed at the Meteorological Research Institute (MRI) (hereafter referred to MRI-CCM2.1) (Deushi and Shibata 2011; Yukimoto et al. 2019). The model was developed based on version 1: MRI-CCM1 (Shibata et al., 2005), which was used to calculate JRA-55 Ozone (Kobayashi et al. 2015). MRI-CCM2.1 updated several important issues by adding detailed tropospheric chemistry processes (Deushi and Shibata 2011) and improving stratospheric chlorine and bromine chemistry processes (Yukimoto et al. 2019). As a result, the ozone biases in MRI-CCM2.1 considerably reduced compared with those found in MRI-CCM1, which had a positive ozone bias in the troposphere and a negative ozone bias in the middle and upper stratosphere from 20 hPa to 1 hPa.

It is noteworthy that representations of ozone-depleting substances (ODSs) such as chlorofluorocarbons and halons in the calculation of JRA-3Q Ozone were improved compared with those used in the calculation of JRA-55 Ozone. The mixing ratios of ODSs were treated as prognostic variables in MRI-CCM2.1, and their surface concentrations were specified based on forcing data of the Coupled Model Intercomparison Project Phase 5 (CMIP5) historical experiment and the Representative Concentration Pathways (RCPs) 6.0 scenario experiment (Taylor et al. 2012 and references therein). In contrast, the mixing ratios of ODSs were not treated as prognostic variables in MRI-CCM1. Instead, the time evolution of the total chlorine and bromine atoms in inorganic source gases was computed in advance using an off-line, one-dimensional chemistry model. The computed one-dimensional (i.e., globally uniform) vertical profile was prescribed to the MRI-CCM1 as a function of altitude and time. This prescribed total chlorine and bromine was used for the calculation of net chemical productions of the total reactive chlorine and bromine (Kobayashi and Shibata 2011).

In JRA-3Q Ozone, MRI-CCM2.1 was driven by the JRA-55 wind data with a nudging technique (Kobayashi and Shibata 2011) to reproduce the meteorological fields observed since 1958. This treatment — using previous wind products for computing ozone transport — is similar to that in JRA-55. Before 1958, wind data from a JRA-3Q preliminary experiment were used for the nudging. (cf. JRA-25/JCDAS winds were used for JRA-55 Ozone.) The satellite observations of total ozone were assimilated into the model using a nudging technique (JMA 2019) for the period since 1979. Satellite Level-2 total column ozone datasets were collected and merged with correction of intersatellite biases using ground-based total ozone observations (Naoe et al. 2020). No ozone observation data were assimilated prior to 1979. Accordingly, a bias correction for the modeled ozone mixing ratios was performed for that period. The model bias was estimated from two experiments with and without the assimilation of satellite total ozone data for the period 1980–1984. A similar model bias correction was also conducted for the period before 1958. The model bias during that time was estimated from two experiments nudged towards the JRA-55 wind and the JRA-3Q preliminary experimental wind for the period 1961–1965. Above the vertical level of 1 hPa, another kind of model bias correction was applied for the whole JRA-3Q period, during which time the model bias was estimated with respect to the Stratosphere-Troposphere Processes and Their Role in Climate (SPARC) Halogen Occultation Experiment (HALOE)/Microwave Limb Sounder (MLS) climatological monthly means for 1991–1997 (Randel et al. 1998).

4.4 Long-lived greenhouse gases

The greenhouse gases considered in the forecast model used in JRA-3Q and JRA-55 are carbon dioxide (CO_2), methane (CH_4), nitrous oxide (N_2O), and the CFCs (trichlorofluoromethane [CFC-11], dichlorodifluoromethane [CFC-12], and chlorodifluoromethane [HCFC-22]). Table 3 lists the data sources for each substance. JRA-3Q uses CO_2, CH_4, and N_2O data compiled by the World Data Centre for Greenhouse Gases (WDCGG) for the period from the 1980s to 2016; during other periods, JRA-3Q uses historical forcings and the Shared Socioeconomic Pathway (SSP) 2-4.5 forcing scenario for the Coupled Model Intercomparison Project Phase 6 (CMIP6; Eyring et al. 2016) conducted for the Intergovernmental Panel on Climate Change (IPCC) Sixth Assessment Report (AR6). For CFCs, the 2014 updated version of the A1 scenario from the WMO/United Nations

Environment Programme (UNEP) Scientific Assessment of Ozone Depletion is primarily used. Each dataset contains annual average values of greenhouse gas concentrations, and JRA-3Q uses daily values obtained by linear interpolation of the annual values.

5. Observations

5.1 Data sources

Because the period prior to 1958 was not covered by the previous Japanese reanalyses, observational datasets for that period were collected from the following data sources for use in the JRA-3Q production (Table B1).

Near-surface observations over land were obtained from the Hadley integrated surface dataset (HadISD) v3.1.0.201911p (Dunn 2019), which was compiled from the National Centers for Environmental Information (NCEI) Integrated Surface Database (ISD; Smith et al. 2011) by selecting stations with long-term observations and quality-controlling the data. For near-surface observations over the sea, marine meteorological data from ships and buoys were obtained from the International Comprehensive Ocean-Atmosphere Data Set (ICOADS) Release 3.0 (Freeman et al. 2017). In addition, surface pressures were obtained from the International Surface Pressure DataBank (ISPD) version 4 (Compo et al. 2019), which was created to be the observational input for the National Oceanic and Atmospheric Administration (NOAA)/Collaborative Institute for Research in Environmental Sciences

(CIRES) 20th Century Reanalysis (20CR) and has also been widely used for other studies.

Upper-air observations were obtained from the Integrated Global Radiosonde Archive (IGRA) version 2 (Durre et al. 2016), which is collected and maintained by the NCEI. In addition, upper-air observations were also acquired from the Comprehensive Historical Upper-Air Network (CHUAN) version 1.7 (Bronnimann and Stickler 2013), which contains rescued and digitized data before the International Geophysical Year (IGY; 1957–1958). These two datasets, however, may contain overlaps that are difficult to identify. Preliminary investigation found that IGRA version 2 generally contains more observed variables than CHUAN version 1.7 for stations where there is overlap. Accordingly, IGRA was preferred over CHUAN, and CHUAN data were used only for stations in Japan where there were no overlaps.

There are few Japanese stations included in these datasets, especially prior to the early 1950s. For example, although more than 10 Japanese stations had already started upper-air observations by 1947, data from only two of those stations extend back to 1947 in IGRA version 2. Additional data were therefore obtained from land surface observations at nine stations in Japan and radiosonde observations at Tateno, one of the upper-air observation stations in Japan. Those data were digitized by the MRI from the original observation registers. In addition, radiosonde observations in Japan from September to October 1947 were digitized from monthly reports (Central Meteorological Observatory 1948).

Observations for the period from 1958 are based on those used for JRA-55 (Kobayashi et al. 2015). Newly available observations, such as reprocessed or recalibrated satellite climate data records (CDRs), were also collected and used to the extent possible (Fig. 3, Table B1). For example, JRA-3Q uses atmospheric motion vectors (AMVs) from the GMS-5 and MTSATs that were newly reprocessed by the JMA Meteorological Satellite Center (MSC) using a derivation algorithm for the Himawari-8 satellite (Abe et al. 2021).

TCBs used in JRA-3Q were newly generated for all TC basins with the JMA's typhoon bogussing method (JMA 2019). To generate TCBs, information including the position of a TC, its central pressure, and radius of 15 m s^{-1} winds is needed. In the western North Pacific, such tropical cyclone information was obtained from the International Best Track Archive for Climate Stewardship (IBTrACS; Knapp et al. 2010) for the period prior to 1951, and the JMA's tropical cyclone information has been used for the subsequent time period. In the other regions, such tropical cyclone information was basically obtained from IBTrACS until 2021 and has been received from tropical cyclone centers thereafter. It should be noted that there are multiple agencies that provide TC information for each TC basin and IBTrACS is a collection of TC track and intensity estimates from many sources (details on how TC information is selected for JRA-3Q is given in Subsection 5.3).

Furthermore, JRA-3Q uses airport observations, zenith total delays (ZTDs) from the ground-based Global Navigation Satellite System (GNSS) and radiances from hyperspectral infrared sounders, which were introduced into the JMA operational system after JRA-55. The GNSS ZTDs were reprocessed by the MRI for the period 1994–2014 and those operationally received have subsequently been used. The difference between the time of the transmission and the time of reception includes not only the delay due to the distance between the satellite and the receiver but also the delay of propagation due to atmospheric conditions. Because the GNSS ZTD is related to the integrated water vapor above the station, assimilation of the ZTD has a positive impact on the accuracy of the analysis of the water vapor field in the lower troposphere.

5.2 Quality control and data selection

Observations may contain "poor” data for a variety of reasons, including instrument malfunction and human error. If such erroneous data are used for data assimilation, the quality of the reanalysis product can be significantly degraded, and the data assimilation process may terminate abnormally in some cases. It is therefore important to detect low-quality data before data assimilation and correct or eliminate those data in a set of quality control (QC) and data selection steps.

In general, the first step of data assimilation involves the use of QC processes to automatically exclude erroneous observations that are inconsistent with other observations or that deviate significantly from the first guess (Onogi et al. 2007). In addition, observations that are found to be of low quality as a result of offline QC are blacklisted in advance to prevent them from being used for data assimilation.

In addition to "poor" data, observations unsuitable for assimilation are excluded, such as those that are far less accurate than background, those whose spatial representativeness considerably differs from that of background, or for which background equivalents cannot be generated with sufficient accuracy. Observations are thinned to reduce computational costs and to avoid the effects of observation error correlation that is not accounted for in the JRA-3Q data assimilation system.

The following subsections explain the principal changes that have been made in the QC and data selection methods for each type of observation since JRA-55. Details on the quality control and data selection methods in JRA-55 have been described by Kobayashi et al. (2015).

a. Conventional data

The QC for conventional data is basically the same as in JRA-55 and consists of a climatological check, track check, consistency check, and gross error check (Onogi et al. 2007).

For the period from July 2015, JRA-3Q assimilates surface pressures from airport observations, which was newly introduced into the operational NWP system after JRA-55 (Kosaka 2016). Surface pressures from airport observations are used based on Ingleby (2014), and the data are assimilated with the same priority as other surface pressures. Note that bias correction is not applied to any surface pressures.

JRA-3Q completely excludes surface pressures in tropical latitudes of the Amazon River basin and Africa for the following reason. A preliminary experiment with JRA-3Q showed that there were discrepancies between surface pressures from land stations and airport observations versus the background field in the Amazon River basin, which is similar to what occurred in the preliminary experiment with JRA-55. Once the land surface was dried up, a feedback mechanism that reinforced positive increments of surface pressure in the data assimilation system was maintained, as indicated in JRA-55 by Kobayashi et al. (2015). When observations of surface pressure over the Amazon River basin were used for the data assimilation, artificial anticyclonic circulation was produced in the lower troposphere, and the resultant dry bias was apparent in the Amazon River basin. That dry bias further reinforced the discrepancies with the background field in the preliminary experiments. The same mechanism that reinforced feedback was also apparent in tropical Africa.

Radiosonde temperature records contain numerous discontinuities arising from factors such as modifications in radiosonde instruments. It is crucial to remove the discontinuities before using these records for climate applications. In JRA-3Q, bias correction of radiosonde temperatures is applied with RICH with solar elevation dependence (RISE; Haimberger et al. 2012), which estimates biases either by comparisons with radiosonde temperatures or by comparison with background departures of surrounding radiosonde stations. In contrast, JRA-55 uses the Radiosonde Observation Correction Using Reanalysis (RAOBCORE) (Haimberger et al. 2008, Haimberger et al. 2012), which estimates biases based on a comparison of radiosonde temperatures with backgrounds from the ECMWF 45-year Reanalysis (ERA-40; Uppala et al. 2005) and ERA-Interim (Dee et al. 2011), and thus the bias correction is dependent on the homogeneity of the reanalyses.

Numerous aircraft observations over the continental United States were thinned to one-fiftieth by preliminary screening for the period from 29 May 2014 in both JRA-3Q and JRA-55. As with JRA-55, aircraft temperatures are not assimilated in JRA-3Q. In the JMA's operational NWP system, bias corrections are applied to aircraft temperatures using one-month statistics for each aircraft identifier. However, this bias correction method cannot be applied for reanalysis because the identifiers for older aircraft observations are often unknown.

Table 4 shows the data counts, rates of rejection due to QC, and rates of use of each type of conventional observation for the year 2017 in JRA-3Q and JRA-55. The data counts in Table 4 do not include data excluded by blacklisting or preliminary screening. In JRA-3Q, there is a slight decrease in the rate of use of surface pressures from land stations, commercial or research vessels, or buoys compared with their rate of use in JRA-55. This difference is due to the new use of surface pressures from airport observations with the same priority as other surface pressures. For each type of observation, the rate of rejection has tended to be lower in JRA-3Q than in JRA-55. Because there is no change in the source of observation data or QC method in JRA-3Q, improved accuracy of the first guess may have resulted in the lower rate of rejection by the gross error check.

b. Ground-based GNSS zenith total delays (ZTDs)

In the QC for GNSS ZTDs, JRA-3Q does not use ZTDs with stations at an elevation above 5000 m or with data for which the absolute value of the difference between the elevation and the model surface exceeds 300 m. In the climatological check, ZTDs less than 1000 mm or greater than 3000 mm are rejected. In the spatial consistency check, ZTDs are rejected if the absolute value of the background departure is greater than 50 mm and the absolute value of the difference between the background departure of the station and the average of background departure at neighboring stations within 100 km is greater than 50 mm.

c. Satellite radiances

1) Infrared sounders

For newly introduced hyperspectral infrared sounders (Okagaki 2015), channels within a CO_2 absorption band sensitive to temperature are used for assimilation from the Atmospheric Infrared Sounder (AIRS) on *Aqua*, the Infrared Atmospheric Sounding Interferometer (IASI) on the Meteorological Operational satellite (Metop) satellites, and the Cross-track Infrared Sounder (CrIS) on the Suomi-NPP and *NOAA-20* satellites. Infrared radiation is strongly absorbed by clouds, but it is difficult for the current data assimilation system to fully account for cloud effects. The split window method (Inoue 1985) is thus used to detect clouds, and the CO_2 slicing method (Eyre and Menzel 1989) is used to estimate cloud-top height.

The use of infrared sounders other than hyperspectral infrared sounders is basically the same as in JRA-55 (Kobayashi et al. 2015), except that the thinning interval for radiances from the High Resolution Infrared Radiation Sounder (HIRS) and Stratospheric Sounding Unit (SSU) was reduced from 250 km in JRA-55 to 125 km in JRA-3Q.

2) Microwave imagers

The QC for radiances from the 19, 24, 37, and 89 GHz vertical polarization channels on the new GPM Microwave Imager (GMI) and Micro-Wave Radiation Imager (MWRI) is the same as that on other microwave imagers. For snow depth analysis, new retrievals from the Advanced Microwave Scanning Radiometer-2 (AMSR-2) as well as retrievals from the Special Sensor Microwave/Imager (SSM/I) and the Special Sensor Microwave Imager Sounder (SSMIS) used in JRA-55 are used in JRA-3Q to estimate daily snow cover.

3) Microwave sounders

JRA-3Q assimilates newly available radiances from tropospheric temperature-sounding channels of ATMS and humidity-sounding channels of the Special Sensor Microwave Water Vapor Profiler (SSM/T-2), SSMIS, ATMS, Sondeur Atmospherique du Profil d'Humidite

Intertropicale par Radiometrie (SAPHIR), and GMI (Tables 5 and 6) in addition to the microwave sounders used in JRA-55 (Kobayashi et al. 2015).

For SSM/T-2, there are periods during which the method of rain detection used for the AMSU-B / MHS cannot be applied because of a failure of window channels. Cloud detection is therefore performed using two criteria: a viewing-angle-dependent threshold on the brightness temperature from the upper tropospheric humidity channel (at 183.31 ± 1.0 GHz) (T_1^{b}) and a threshold based on the difference between the brightness temperature from the middle tropospheric humidity channel (at 183.31 ± 3.0 GHz) (T_3^{b}) and T_1^{b} (Kobayashi et al. 2017).

Radiances from the SSMIS humidity-sounding channels are calibrated with the unified preprocessing scheme (Bell et al. 2008) and assimilated only under clear-sky conditions over the ocean (Murakami and Kazumori 2017). Cloud/rain detection is performed using a combination of the 37-, 91-, and 183-GHz channels, which have large sensitivities to cloud liquid particles, snow crystals, and ice crystals, respectively.

Because SAPHIR has no window channels available for cloud detection, cloud-affected radiances are detected and screened out using empirical cloud-detection thresholds for background departures of the humidity-sounding channels. Radiances from SAPHIR over land are also removed to avoid surface signal contamination under dry atmospheric conditions (Kazumori 2016b).

Radiances from the GMI humidity-sounding channels (183.31 ± 3 and 183.31 ± 7 GHz) are assimilated after screening out cloud-affected data by using background departures of the window channel (166 GHz) (Kazumori 2016a).

Radiances from AMSU-B and MHS over land are assimilated in addition to those over the ocean using an atlas of land-surface emissivity and hourly forecasts of land-surface temperature from the forecast model (Kazumori 2012). In JRA-55, the radiance simulation for channels that have a large sensitivity to the surface is not sufficiently accurate because the surface emissivity over land is fixed at 0.9, and the atmospheric temperature at the lowest model level from the short-range forecast is used as a substitute for the temperature of the land surface. JRA-3Q has solved this problem and assimilated radiances from AMSU-B and MHS over both land and ocean, which in JRA-55 were limited to the ocean area.

For the Microwave Sounding Unit (MSU), the thinning interval was reduced from 250 km in JRA-55 to 125 km in JRA-3Q.

4) Clear-sky radiances (CSRs)

JRA-3Q takes advantage of improvements in the use of CSRs (Okabe 2019). Specifically, except for the GMS-5 and MTSATs, the surface emissivity atlas of the University of Wisconsin (Borbas and Ruston 2010) is used to improve the accuracy of radiative transfer calculations (see subsection 2.1.b). For *Himawari-8*, the Geostationary Operational Environmental Satellite (GOES) 16, and the Meteosat Second Generation (MSG) satellite, surface temperatures are retrieved from the CSRs of the infrared window channel instead of using the first guess. The CSRs from the upper-middle tropospheric water vapor channels of *Himawari-8* and *GOES 16* as well as the mid-tropospheric water-vapor channel of MSG are then assimilated in addition to the CSRs from the upper-tropospheric water-vapor channel, which are already assimilated in JRA-55. The CSRs at altitudes above 4000 m in model elevation are excluded because the difference between the model elevation and the actual elevation is too large for the radiative transfer calculation to be sufficiently accurate and because there is little water vapor information in the CSRs in the high-elevation region. In JRA-55, the CSRs from *Himawari-8* were assimilated hourly, whereas other CSRs were assimilated every two hours. In JRA-3Q, all CSRs are now assimilated hourly.

d. Atmospheric Motion Vectors (AMVs)

The low Earth orbit–geostationary (LEO-GEO) AMV (Lazzara et al. 2014) developed by the Cooperative Institute for Meteorological Satellite Studies (CIMSS) has recently been assimilated into the operational NWP system (Yamashita 2014) and is used in JRA-3Q. The LEO-GEO AMV is calculated using a composite of images observed by polar-orbiting satellites and images observed by geostationary meteorological satellites. It can cover a data gap in the latitudinal band of ~60°. Such a gap cannot be filled by polar-orbiting satellites or geostationary meteorological satellites alone. The QC of this AMV is based on the QC of other AMVs, which is already used in the operational system.

e. Scatterometer ocean surface winds

The data selection method has been changed for the Active Microwave Instrument (AMI) and Advanced Scatterometer (ASCAT) so that their data could be used even for winds stronger than 15 m s^{-1}. For AMI and ASCAT, JRA-55 did not use winds stronger than 15 m s^{-1} (Kobayashi et al. 2015) because the first guess had a positive bias against winds from ASCAT in regions where the winds were strong. This bias prevented effective use of winds in those regions. Later, as the JMA global NWP system was improved, the accuracy of wind forecasts over the ocean was improved, and the positive bias of the first guess in the above-mentioned regions of strong winds was reduced.

f. GNSS–Radio Occultation (GNSS-RO) bending angles

The assimilated variable of GNSS Radio Occultation (GNSS-RO) observation has been switched from refractivity in JRA-55 (JMA 2013) to bending angle in JRA-3Q (Owada and Moriya 2015, Owada et al. 2018). Bending angles are assimilated with the one-dimensional bending angle observation operator included in the software Radio Occultation Processing Package (ROPP) version 8.0, which was developed by the Radio Occultation Meteorology Satellite Application Facility (ROM SAF). In JRA-55, refractivities were not used at altitudes above 30 km because they were derived using climatological atmospheric profiles and therefore considered to be affected by those profiles (Healy 2008). This altitude restriction was removed following the switch of the assimilated variable to bending angle. In addition, because the derivation of refractivity requires not only an observation at the target altitude but also information from above that altitude, the errors of the refractivities within the same profile are correlated with each other. The refractivities in each profile were therefore thinned at 500-m vertical intervals. In contrast, because no such correlations between errors have been found for bending angles (Rennie 2010), the method of data selection has been modified so that no vertical thinning is performed.

5.3 Tropical cyclone bogussing

To improve the accuracy of TC analysis, JRA-3Q assimilates TCBs instead of 6-hourly wind profile retrievals surrounding tropical cyclones (TCRs, Fiorino 2002). The latter were assimilated in JRA-55, but resulted in an artificial downward trend in the global average of 10-m maximum wind speeds near the center of TCs in JRA-55. That trend was attributed to an artificial downward trend of the wind speed in the TCRs (Kobayashi et al. 2015).

In the method of TCBs, a characteristic TC structure is first estimated using TC information such as central position, central pressure, and 15 m s^{-1} gale-force wind radius, and then pseudo-observation (i.e., TC bogus) data are generated based on that TC structure. TC bogus data consisting of mean sea level pressure and winds at 850 hPa and 300 hPa are assimilated together with other observations. Many meteorological centers provide TC information, and Table 7 lists the specific agencies that provided data in each area for JRA-3Q.

Note that even for the same TC, the radius of gale-force winds varies greatly depending on the agency that provided the data. Because the JMA typhoon bogus generation method was developed based on JMA's best track data, adequate TCBs cannot be generated using the radii of gale-force winds reported by other centers. The reported radius of the gale-force winds is therefore used only with JMA data; otherwise, with data from other centers, the radius of the gale-force winds is estimated from the central pressure by using the following regression equation based on JMA's best track data:

$$R_{15} = -4.335 \times P + 4566.5,$$

where R_{15} is the 15 m s^{-1} gale-force wind radius (km) and P is the central pressure (hPa). The regression equation was also used for JMA's best track data if the gale-force wind radius was not available, which is typically the case prior to 1977.

It should also be noted that TC information does not include central pressures for some periods. In that case, the central pressure is estimated using the equation of Atkinson and Holliday (1977) as follows:

$$V = 6.7(1010 - P)^{0.644},$$

where V is the maximum sustained 1-min wind speed (m s^{-1}).

5.4 Changes in input observations

Figure 4 shows time series of monthly mean counts of conventional observations assimilated in the atmospheric analysis component of JRA-3Q and JRA-55 in five latitudinal bands. For the period before the IGY, most of the assimilated observations were conventional surface pressures, and the other observations, including upper-air observations, were few in number compared with the period after the IGY. The number of upper-air observations gradually increased from year to year after the IGY, mainly in the mid- to high latitudes of the Northern Hemisphere and the tropics; however, the number of such observations remained small in the polar region and mid-latitudes of the Southern Hemisphere even after the IGY. In addition, the number of surface pressures has increased in the mid- to high latitudes of the Northern Hemisphere since 2015 compared with the number in JRA-55 because of the assimilation of surface pressures from airport observations. However, the number of surface pressures assimilated in the tropics after the IGY is smaller in JRA-3Q than in JRA-55 because of the complete exclusion of surface pressures over tropical Africa and the Amazon basin in JRA-3Q, as described in Subsection 5.2.a.

Figures 5 and 6 show the global monthly mean counts of aircraft observations, ground-based remote sensing observations, and satellite observations assimilated in the atmospheric analysis component of JRA-3Q and JRA-55. The use of new reprocessed data with extended period back in the past made scatterometer and GNSS-RO observations available from about five years earlier in JRA-3Q than in JRA-55. The increase in the number of assimilated GNSS-RO observations, compared with the number assimilated in JRA-55, is remarkable. This increase is due mainly to the improved method of assimilation of the GNSS-RO observations in the operational NWP system, as described in Subsection 5.2.f. For satellite radiances, the number of assimilated observations has also increased in JRA-3Q compared with JRA-55, especially before 2000. This increase is due to a reduction of the thinning interval for radiances from HIRS, SSU, and MSU (see Subsections 5.2.c.1 and 5.2.c.3 for details) as well as to the enrichment of satellite observations of humidity through the introduction of SSM/T-2 and the use of reprocessed microwave imagers and humidity sounders. Furthermore, JRA-3Q assimilates new observations such as ground-based GNSS ZTDs and hyperspectral sounder radiances. As a result, the number of observations assimilated in JRA-3Q has increased overall compared with the number assimilated in JRA-55.

6. Production

In JRA-3Q, the period covered is divided into three streams to shorten the production time: Stream A (from 1991 onward), Stream B (October 1959 to December 1990), and Stream C (September 1947 to September 1959). The production of Stream A is continuing on a near-real time basis. It must be noted that the period from May 2013 to December 2021 was recalculated to correct a problem caused by inappropriate TCBs in areas other than the western North Pacific.

As a result, the combined dataset shown in Fig. 7 has three discontinuities: 1 October

1959, 1 January 1991, and 1 January 2022. Details of the products from the JRA-3Q system are given in JMA (2022a, 2022b).

7. Basic performance of the data assimilation system

7.1 Two-day forecast scores

Figure 8 shows time series of root mean square (RMS) errors of two-day forecasts of the geopotential height at 500 hPa averaged over the extratropical Northern and Southern Hemispheres, and Fig. 9 shows those for the wind vector in the upper and lower troposphere averaged over the tropics, in JRA-3Q, JRA-55, JRA-25, and the JMA operational system, verified against their own analyses. The comparison is not made using a common standard because the forecasts were carried out using their own forecast models. Nevertheless, it can provide useful insights into the consistency of the analyses and forecasts, the impact of changes in observing systems, and the temporal consistency of each product.

The decrease in the RMS errors from JRA-25 to JRA-55 to JRA-3Q apparent in Figs. 8 and 9 shows that there was a steady improvement in the performance of the JMA data assimilation systems. The improvement of the forecast scores has arguably been brought about to some extent by the increased number and improved quality of observations such as reprocessed satellite data. In particular, the RMS errors of the geopotential height at 500 hPa in JRA-3Q were reduced significantly in the extratropical Southern Hemisphere during the 1990s. This reduction was most likely due to the reduced thinning interval for radiances from HIRS, SSU, and MSU (see Subsections 5.2.c.1 and 5.2.c.3 for details) and adjusted background error variances (Subsection 3.2.a). The smaller variations of the forecast scores across periods and regions in JRA-3Q versus JRA-55 indicate that the JRA-3Q product is more homogenous than the JRA-55 product.

In contrast, during the pre-satellite period (until 1972), the forecast scores of both JRA-3Q and JRA-55 gradually deteriorated in the extratropical Southern Hemisphere and tropics, despite the expansion of the observing system. The low RMS errors in these regions during this earlier period most likely resulted from the fact that observations were too few to have a significant effect on data assimilation. In such a case, the RMS error is not an appropriate indicator of analysis quality, and the smallness of RMS errors should be interpreted as the lack of quality of the verifying analysis. Thus, the sparseness of the observations available for this period remains a challenging issue for data assimilation.

7.2 Background fits to observations

Because background departures are basically independent of the prescribed parameters of a data assimilation system such as background and observation error, their statistics can provide useful information for evaluating the performance of the forecast model and biases in observations. We compare in Fig. 10 time series of global means and RMS of the background departures of radiosonde temperatures used in JRA-3Q, JRA-55, and JRA-25.

The time series of global mean departure at levels near 250 hPa (Fig. 10c) show that the warm bias in the upper troposphere is significantly diminished in JRA-3Q compared with JRA-55. At levels near 850 hPa, the positive global mean departures in JRA-25, JRA-55, and JRA-3Q suggest a cold bias in the lower troposphere. Nevertheless, the reduction of the global mean departures in JRA-3Q indicates that the cold bias has been mitigated (Fig. 10g). The RMS departures of JRA-3Q in the troposphere (Figs. 10d, f, h) also demonstrate moderately improved consistency with radiosonde temperatures from the 1980s compared with those of JRA-55.

At levels near 30 hPa, in contrast, the sharp increases exhibited by the global mean departures in JRA-3Q after large volcanic eruptions, specifically in 1982 (El Chichón) and 1991 (Mt. Pinatubo), suggest a diminished representation of volcanic-induced temporal warming in the stratosphere (Fig. 10a). Because the forecast models of JRA-25, JRA-55, and JRA-3Q do not take into account interannual variations of volcanic aerosols, the difference in the representation of warming was most likely caused by a difference in the impact of radiosonde observations, which are important observations for constraining model biases and anchoring variational bias correction applied to satellite radiances. In the middle troposphere prior to the late 1970s and in the stratosphere, there is also a slight deterioration in the consistency of radiosonde temperatures in JRA-3Q compared with JRA-55. These deteriorations are most likely because the background error covariances used for JRA-3Q are basically the same as those used for the operational system, which have been optimized for the current, enhanced observing system. Such background error covariances are characterized by shorter horizontal correlation lengths than the ones used for JRA-55 (Fig. 11), which means that observations have a shorter spatial effect on the assimilation system in JRA-3Q and might explain why errors in background fields were insufficiently corrected in past periods of sparse observations. Further studies are required to examine whether such sparse observations would still be able to constrain a systematic model error in the case of increased horizontal correlation lengths.

The very large global mean and RMS departures during the 1940s are due primarily to a decreased accuracy of background fields. It must be noted that temporal variations of mean and RMS departures during this period are greater than those during later periods, which might be partly attributed to larger statistical uncertainties because upper-air observations during this period are available in very small numbers and located in limited areas in the Northern Hemisphere.

8. Major improvements from JRA-55

8.1 Global energy budget

The global energy budget is affected by increasing concentrations of greenhouse gases, changing concentrations of aerosols, and associated feedbacks and is of great interest along with the intensity and temporal variation of the water cycle. In atmospheric reanalysis, the temporal conservation of energy is not guaranteed because analysis increments are added through data assimilation processes. However, evaluating the global mean energy budget of the reanalysis can provide useful insights regarding the performance of the data assimilation system, especially the physical processes of the forecast model used in the system, as well as the performance of reanalysis products as driving fields for ocean and land surface models. With the recent improvement of satellite observations, radiation at the top of the atmosphere (TOA) has been accurately measured. Wild et al. (2013) have estimated the global mean energy budget and ranges of uncertainty at the TOA and the Earth's surface using satellite and surface observations and the results of the simulations performed in CMIP5. We evaluated various JRA-3Q energy fluxes using revised values of these estimates (Forster et al. 2021, Wild et al. 2015, 2019; hereafter referred to as W19) which are assessed based on multiple lines of evidence, including the satellite observations used in these estimates (CERES-EBAF Edition 4.0, Loeb et al. 2018, Kato et al. 2018) and the air-sea flux dataset (OAflux, Yu 2019).

Table 8 shows the components of the global mean annual energy budgets for TOA from W19, reanalyses (JRA-25, JRA-55, JRA-3Q, and ERA5), and CERES-EBAF. The values of both the TOA solar incoming and reflected radiation from JRA-3Q are within the ranges of uncertainty of W19, and the net absorbed solar radiation from JRA-3Q exceeds that from JRA-55 by 3 W m^{-2}. The TOA outgoing thermal (longwave) radiation of JRA-3Q is closer to the estimated value of W19 than that of JRA-55, but it still has a bias of about 10 W m^{-2}.

Figure 12 compares the spatial distributions of the radiation fluxes from JRA-3Q and JRA-55 with those from CERES-EBAF. There is an excessive reflection of solar radiation over low-latitude oceans and an under-estimation over mid- and high-latitude oceans in the reanalyses, but the excessive reflections are reduced over the tropical regions in the JRA-3Q. The reduction in excess reflection is most likely due to the change in the cloud overlap assumption for shortwave radiation in the forecast model used in JRA-3Q (Subsection 3.1b) and resulting improved representation of optical depth of clouds. The improvement in the other regions may also be attributed to improved representation of low-level clouds due to improvements in the oceanic stratocumulus scheme and other factors. The spatial distribution of outgoing longwave radiation shows an excess bias in areas of active convection in the vicinity of the maritime continent, Central Africa and Amazonia, but the bias from satellite observations is smaller in JRA-3Q than in JRA-55. This reduction of bias is most likely attributable to the improved scheme for cloud ice fall and conversion to precipitation (Subsection 3.3). As a result, the global mean net flux at the TOA from JRA-3Q is -5.5 W m^{-2}, about half the corresponding flux from JRA-55. Although this estimate is an improvement over JRA-55, it still indicates a cooling of the climate system. The estimate from ERA5 ($+0.7$ W m^{-2}) is within the range of uncertainties of W19, which indicates a net energy gain corresponding to the current anthropogenic climate change. Future Japanese reanalyses should improve the radiation components, in particular outgoing longwave, and resulting global energy budget.

Figure 13 shows the evolution of the global mean energy flux at the TOA. The time series of reflected solar and outgoing longwave radiation of JRA-3Q and CERES-EBAF are in good agreement for the period 2002–2012. The reflected solar radiation of JRA-55 shows jumps in the 1970s and mid-2000s that are probably due to the impact of changes in observing systems. The forecast model used in JRA-55 has a dry bias in the regions of deep convection, which makes JRA-55 particularly susceptive to changes in satellite humidity observing systems. Such susceptibility has been greatly decreased due to a significant reduction or elimination of the dry bias in JRA-3Q (see Subsection 9.2 for details). Meanwhile, the time series of reflected solar radiation from JRA-3Q does not show the impact of stratospheric aerosols caused by volcanic eruptions. In contrast, the time series from ERA5 represents these impacts as spike-like increases in the mid-1960s, mid-1980s, and early 1990s. In addition, the incoming solar radiation of CERES-EBAF shows temporal variations that correspond to sunspot cycles, but JRA-3Q does not. Incorporation of the effects of volcanic eruptions and sunspot cycles by taking account of interannual variations of volcanic aerosols and solar constants in the forecast model should be addressed in future Japanese reanalyses.

Table 9 shows the components of the global mean annual mean energy budgets at Earth's surface from W19, reanalyses, and CERES-EBAF. The global mean radiative fluxes and sensible heat flux of JRA-3Q are all within the ranges of uncertainty of W19. The latent heat flux is excessive by about 7 W m^{-2} compared with the W19 estimation. As a result, the net energy flux at the Earth's surface amounts to −4.4 W m^{-2} in JRA-3Q, which differs from the W19 estimate (0.6 W m^{-2}) by about −5 W m^{-2}. The net energy flux over the ocean in JRA-3Q is −6.5 W m^{-2}, significantly closer to the estimate of Wild et al. (2015) (+0.8 W m^{-2}) compared with the estimate of −15.9 W m^{-2} in JRA-55. This better agreement is due to overall improvements in parameterizations of physical processes. The negative value in JRA-3Q indicates global cooling of the ocean, whereas the estimate of Wild et al. (2015) is positive, indicating ocean heat uptake resulted from anthropogenic global warming. According to Valdivieso et al. (2017), many of the reanalysis systems that were part of the Ocean/Coupled Reanalysis Intercomparison Project showed positive values, albeit with a large spread compared to the uncertainty of W19. Improving the surface energy balance is another issue that should be considered in future Japanese reanalyses.

Figure 14 shows the spatial distributions of annual mean energy fluxes at the Earth's surface. There is less bias of each energy flux in the tropics in JRA-3Q than in JRA-55. In particular, the negative biases in net radiation flux near the maritime continent in JRA-55 are changed to positive biases in JRA-3Q. This resulted in a reduced bias on average over the entire tropical ocean. This change of the spatial pattern is most likely due to improved estimates of downward solar radiation associated mainly with the improved cloud radiation scheme. Improved net radiation fluxes in Australia, South Africa, southern South America, the western United States, and the Middle East are most likely attributable to the updated bare soil albedo (Subsection 3.6).

8.2 Tropical cyclones

To address the issue of unrealistic long-term weakening trend of TCs in JRA-55 (Kobayashi et al. 2015), JRA-3Q changed from the TCR calculation method used in JRA-55 to the TCB generation method based on the JMA operational system (Subsection 5.3). This subsection describes the evaluation results for the representation of TCs in JRA-3Q in terms of detection rate, maximum wind speed. For the evaluation, the observational best tracks produced by the Joint Typhoon Warning Center (JTWC) (Chu et al. 2002) and the National Hurricane Center (NHC, Landsea and Franklin 2013) were used because those sources of data have a high rate of recording of maximum wind speeds. Different best tracks were used for each area of the ocean to calculate detection rates: Those of JTWC were used for the western North Pacific, the North Indian Ocean, and the Southern Hemisphere, and those of NHC were used for the eastern North Pacific and North Atlantic. Note that the best track data used for the evaluation is not the same as that used for TCB generation.

Figure 15 shows the rates of TC detection in JRA-3Q and JRA-55 calculated by the method of Hatsushika et al. (2006). As mentioned above, the rate of detection in JRA-55 has been declining since the late 1980s. In contrast, because the weakening trend seen in

JRA-55 has been resolved in JRA-3Q, the rate of detection in JRA-3Q generally exceeds 90% throughout the analysis period. This improved detection rate is mainly attributed to the use of JMA's own TCBs, which appropriately estimate and capture the strength of TCs regardless of the availability of gale-force wind radius and central pressure (as described in section 5.3). It should also be noted that the JRA-55 TCR has an issue with the estimation method during periods when gale-force wind radius data are not available (Kobayashi et al. 2015).

JRA-3Q also assures long-term consistency in terms of maximum wind speeds, compared with JRA-55 (Fig. 16). The best track shows no long-term trend of changes, but a temporary strengthening is apparent from the late 1950s to the early 1960s, and there is a sharp strengthening in the 2000s. The best track data are not necessarily produced with a frozen algorithm nor based on observations of temporary consistent quality, therefore these variations might be unrealistic. In contrast, a more stable trend throughout the period compared to the best track is apparent in JRA-3Q. However, it should be noted that the maximum wind speeds of TCs in JRA-3Q are about 50–60% of the best track wind speed, which is mainly due to difference of spatial representativeness. This figure demonstrates improved consistency of JRA-3Q as well as indicates the limitations of the representation performance of tropical cyclones in global atmospheric reanalyses at present.

9. Basic characteristics of JRA-3Q

9.1 Temporal consistency of temperature analysis

In recent reanalyses, the representation of trends is generally improved compared to the previous generation of reanalyses because the methods to correct for bias of satellite radiances are more sophisticated (e.g., Simmons et al. 2014, 2017). In contrast, state-of-the-art systems cannot successfully assimilate past sparse data, resulting in lowered temporal consistency (e.g., Simmons et al. 2020) if background error covariances are optimized for the current enhanced observing systems. Because JRA-3Q is expected to be used in a wide range of disciplines, including studies of multidecadal variability and climate change, it is very important to assess its temporal consistency. Here, we compare low-frequency variability and trends apparent in JRA-3Q with those in JRA-55 and independent observational datasets.

a. Surface

Figure 17 shows global monthly mean surface temperature anomalies in JRA-3Q, JRA-55, ERA5, and independent observational datasets. The independent observational datasets are the Met Office Hadley Centre/Climatic Research Unit global temperature dataset (HadCRUT5 analysis; Morice et al. 2021), NOAA Global Surface Temperature Dataset (NOAAGlobalTemp; Huang et al. 2020), Goddard Institute for Space Studies Surface Temperature (GISTEMP; Lenssen et al. 2019), and Berkeley Earth (Rohde and Hausfather 2020). It must be noted that the global mean surface air temperatures in JRA-

3Q and JRA-55 were calculated using analysis fields over land and background fields over the ocean, because analysis fields over the ocean were most likely to be affected by biases of observations of air temperature from ships (Simmons et al. 2004). In fact, the use of analysis fields over the ocean raises global mean surface air temperature anomalies by about 0.1 K for the period from the 1970s to the 1980s (not shown).

In JRA-3Q, ERA5 and all the independent observational datasets but GISTEMP, the top three warmest years coincide, with the higher years being 2016, 2020 and 2019. All datasets are agreed on the three years but with a different order 2016, 2019 and 2020 in JRA-55 and 2020, 2016 and 2019 in GISTEMP. Difference between JRA-3Q and JRA-55 in their rankings of the warmest years is mainly due to differences in anomalies over the polar regions and Africa, especially over the Arctic Ocean where JRA-55 had larger positive anomalies in the case of the year 2019. There are also relatively large differences among the datasets before the late 1970s, mainly because of differences in temperature estimates over sea ice and Antarctica, where observations were sparse. The difference between JRA-55 and JRA-3Q might also be related to the introduction of tiling between sea ice and open water in the forecast model (see Subsection 4.2 for details). Background temperatures over sea ice have become more sensitive to changes in SIC in JRA-3Q. Therefore, the temporal consistency of SICs should be improved for better representation of low-frequency variability in temperature over sea ice.

b. Lower troposphere to lower stratosphere

Figure 18 compares global monthly mean temperature anomalies in JRA-3Q, JRA-55, and independent observational datasets for four layers from the lower troposphere to the lower stratosphere. The independent observational datasets are the Hadley Centre's radiosonde temperature products (HadAT2, Thorne et al. 2005) and MSU and AMSU microwave temperature sounder products from the Remote Sensing Systems (RSS) v4.0 (Mears and Wentz 2016, 2017), the University of Alabama in Huntsville (UAH) v6.0 (Spencer et al. 2017), and NOAA v4.1 (Zou and Wang 2011).

The JRA-3Q time series displays variations very similar to those in the radiosonde and microwave temperature sounder products, except for periods after large volcanic eruptions. In particular, the cooling trend of the lower stratosphere is underestimated in JRA-55, whereas the trends almost coincide in JRA-3Q and HadAT2 (Fig. 18a). Ozone data and the bias correction process for radiosonde temperatures are possible factors relevant to the improved representation of the stratospheric cooling trend. JRA-55 used climatological monthly mean ozone data until 1978, whereas JRA-3Q uses the ozone reanalysis data generated by MRI-CCM2.1 for the entire period (see Subsection 4.3 for details). Radiosonde temperatures in JRA-3Q are bias-corrected with RISE v1.7.2, whereas the temperatures in JRA-55 were bias-corrected until 2006 with RAOBCORE V1.4, which shows a rather small cooling trend in the lower stratosphere (Haimberger et al. 2012).

c. Middle to top stratosphere

Figure 19 compares global monthly mean temperature anomalies of JRA-3Q, JRA-55, and independent observational datasets for the middle, upper, and top stratosphere. Here we used the following latest independent observational datasets: the Stratospheric Sounding Unit (SSU) and MLS stratospheric temperature products from the National Center for Atmospheric Research (NCAR) (Randel et al. 2016) and the SSU and AMSU-A stratospheric temperature products from NOAA v3.0 (Zou and Qian 2016). The previous versions of independent observational datasets based on the SSU data have large uncertainties (Thompson et al. 2012), and those datasets are not available after mid-2006 because of the termination of SSU observations. In the latest versions, reprocessing of the SSU records has reduced their uncertainties, and the datasets have been extended from 2006 onward using stratospheric temperatures from more recent satellite instruments (Maycock et al. 2018).

Trends represented in JRA-3Q from the 1980s are generally consistent with those in the two satellite-based datasets. The JRA-55 time series exhibits unrealistic variations, especially the warming in the upper stratosphere during the period from the late 1950s to the 1960s. The unrealistic variations in JRA-55 were most likely caused by a cold bias of the forecast model that was not constrained because of the paucity of radiosonde observations that reached above 10 hPa during that period. In JRA-3Q, such unrealistic variations have been diminished, most likely because of a reduced cold bias in the upper stratosphere in the forecast model.

However, the low-frequency variability is considerably smaller in JRA-3Q than in the two satellite-based datasets, and even weaker than in JRA-55 because of the fact that the interannual variations of volcanic aerosols and solar constants are not taken into account, and climatological water vapor concentrations are used for the stratosphere in the radiation schemes of both JRA-3Q and JRA-55. In addition, as discussed in Subsection 7.2, the background error covariances used in JRA-3Q are optimized for the current enhanced observing system, and their characterization by shorter horizontal correlation lengths than the ones used in JRA-55 might explain why the model bias is insufficiently constrained where observations are sparse. To improve the representation of stratospheric temperature variability, it is essential to incorporate the above-mentioned missing factors into the forecast model and to optimize the background error covariances in response to changes in observing systems.

9.2 Temporal consistency of humidity analysis

The mid-tropospheric dry bias in JMA Global Spectral Models (GSMs) has been a major issue for many years. It has been pointed out that JRA-55 shows a large moistening increment in layers above 850 hPa (Kobayashi et al. 2015). Furthermore, the recently conducted SPARC Reanalysis Intercomparison Project (Fujiwara et al. 2017) critically assessed the stratospheric water vapor in JRA-55, and concluded that it was excessive and not recommended for use in scientific studies (Davis et al. 2017). This subsection, therefore, discusses the results of quality assessment and long-term homogeneity of water vapor analysis in the troposphere and stratosphere.

Figure 20 compares the zonal-mean specific humidity of JRA-3Q with other reanalyses. The comparison shows that water vapor in the tropical mid-troposphere is greater in JRA-3Q than in JRA-55 (Fig. 20a) but generally similar to that in ERA5 (Fig. 20b) and less than that in MERRA-2 (Fig. 20c). The implication is that the dry bias in the middle troposphere has been reduced in JRA-3Q. This is confirmed from observations as in Fig. 21, which compares JRA-55 and JRA-3Q with the water vapor dataset estimated from GNSS-RO (Kursinski et al. 1997) in the equatorial region (5S–5N). In the middle troposphere, JRA-55 is drier than GNSS-RO, whereas JRA-3Q increases water vapor compared with JRA-55, and the drying bias is generally eliminated, except above 6000 m. In the lower troposphere, however, both JRA-55 and JRA-3Q show the distinct wet bias, which might be related to the excessive surface latent heat flux (as pointed out in Subsection 8.1) and physical processes in the boundary layer. The causes of the excessive water vapor in the lower troposphere require further investigation.

Figure 22 shows a time series of the 12-month running-mean specific humidity in the equatorial region from different reanalysis products. At the 600-hPa pressure level in the middle troposphere (Fig. 22a), JRA-55 has the second lowest specific humidity after the NCEP/ National Center for Atmospheric Research (NCAR) after 1990 and the lowest specific humidity because of a further decrease before 1990, whereas the specific humidity of JRA-3Q is moderately stable among the reanalyses. In the lower troposphere (Fig. 22b), JRA-3Q belongs to a group of reanalyses with a greater amount of humidity, but its interannual variability from the 1950s to the 1960s is generally consistent with that of 20CRv3 (Slivinski et al. 2019).

Interannual variations of the increment of the specific humidity in the troposphere, which can be used to examine the impact of observations on the analysis, are compared between JRA-3Q and JRA-55 in Fig. 23. The increments of specific humidity in JRA-3Q (Fig. 23a) is generally smaller compared with JRA-55 (Fig. 23b), which suggests that discrepancies between the observations and the first guess are smaller in JRA-3Q. In contrast, clear moistening increments are apparent above the 850 hPa level in JRA-55 throughout the period of analysis. The moistening increment increased at the 700–850 hPa levels after the introduction of radiances from the VTPR in the early 1970s. Furthermore, as pointed out by Kobayashi et al. (2015), an increase in the moistening increment is apparent in the upper layers above 500 hPa with the increase of satellite humidity observations from around 1997, but no such trend is apparent in JRA-3Q. These results suggest that there has been a significant reduction or elimination of the dry bias in the middle troposphere of the forecast model and that JRA-3Q is less susceptible to changes of the observing system than JRA-55; as a result, its homogeneity is improved.

As noted at the beginning of this subsection, the quality of stratospheric water vapor in JRA-55 has been identified as a critical issue by climate researchers, so stratospheric water vapor is also discussed here. In a time-height cross section of stratospheric specific humidity averaged over the equatorial region, JRA-55 clearly shows artificial increases or decreases of stratospheric specific humidity; in particular, it shows larger amounts of stratospheric water vapor from 1973 to 1980 and after 2003 compared with the other periods (Fig. 24b). JRA-3Q does not indicate such large amounts (Fig. 24a), except for the increase after 2013. The excessive moisture in JRA-55 was resulted from the above-mentioned large increment that affect the stratosphere through the background error covariance. Because the increment of moistening in the troposphere is smaller in JRA-3Q, such a large increment of moistening no longer occurred in the stratosphere. Reduced background bias in terms of moisture is most likely the main factor that contributed to the relatively stable interannual variation of stratospheric specific humidity.

9.3 Precipitation

Precipitation is one of the most important variables for understanding the mechanisms of the water cycle in the climate system. However, it has been pointed out that the use of precipitation from reanalysis products requires considerable caution because it depends strongly on the performance of the forecast models in the data assimilation system (Bosilovich et al. 2011; Trenberth et al. 2011). Japanese long-term reanalyses have suffered problems about representation of precipitation such as excessive bias, especially in the tropics, and poor quality prior to the late 1980s (Onogi et al. 2007; Kobayashi et al. 2015). The results of precipitation quality assessment, mainly in the tropics, are therefore discussed here.

Figure 25a shows time series of the 12-month running mean of tropical precipitation in various reanalyses and observational datasets. Precipitation in long-term reanalyses is often excessive compared to that in the Global Precipitation Climatology Project (GPCP, Adler et al. 2003, black line) and Tropical Rainfall Measuring Mission (TRMM, Huffman et al. 2007, gray line) observational datasets. The most extreme excesses are seen in the JRA-55 (dark purple line) and ERA-40 (light blue line) data. The JRA-3Q (red line) reduces the excess bias of JRA-55 by about 30%. During the 1950s and 1960s, JRA-3Q shows a smaller decrease in precipitation than JRA-55, and its temporal variability is similar to that of the 20CRv3 (pink line), which was produced using surface pressure observations only. The independent observational dataset, GPCP (black line), generally shows a smaller long-term trend and fluctuation compared with those of reanalyses. These comparisons indicate that the quality of precipitation is more homogeneous in JRA-3Q than in JRA-55. The spatial anomaly correlation coefficients with the GPCP (Fig. 25b) are higher for JRA-3Q than for the JRA-55 throughout the analysis period. In addition, the anomaly correlations with the observational dataset for all long-term reanalysis products are smaller in the 1980s compared with the period after the late 1990s. However, JRA-3Q correlation coefficients always exceed 0.4 and are higher than the JRA-55 correlation coefficients. It should be noted that the anomaly correlations for 20CRv3, also declined during the 1980s. This interesting result suggests that not only the evolution of the satellite observations used in the long-term reanalysis but also other factors such as quality change in GPCP influence the anomaly correlation. However, further research is needed to clarify this quantitatively.

Figure 26 examines the spatial distribution of the precipitation bias against GPCP by decade. The precipitation biases are excessive in the tropics, especially in the Intertropical Convergence Zone (ITCZ) in both JRA-3Q and JRA-55 reanalyses, but they are smaller in JRA-3Q than in JRA-55. There is also a localized underestimation bias around Kalimantan (Borneo Island) in JRA-55 that is reduced in JRA-3Q. Furthermore, during the 1980s, JRA-55 shows a clear excess bias in central Africa (Fig. 26e), which is significantly reduced in JRA-3Q (Fig. 26a).

Figure 27 illustrates the latitudinal distribution of the zonal mean precipitation bias against GPCP by decade to quantify the decadal changes in the excess precipitation bias. Both JRA-3Q and JRA-55 have a common excess bias maximum in the latitudinal zone corresponding to the ITCZ, slightly north of the equator, although the excess bias of JRA-

3Q is about half that of JRA-55 (Figs. 27a and b). The largest increase of the precipitation bias in both JRA-3Q and JRA-55 occurs from the 1990s to the 2000s (Fig. 27c), but the increase in JRA-3Q (0.35 increase, red line in Fig. 27c) is about 60% that of JRA-55 (0.55 increase, purple line in Fig. 27c). We confirm that the inter-annual variations are more stable in JRA-3Q than in JRA-55, and that there is less excess bias in the former, particularly in the tropics. That excess bias had been considered as an issue in JRA-55. These improved results in JRA-3Q can be attributed mainly to the improved parameterization of physical processes in the forecast model, as described in Section 3.

9.4 Representation of past weather prior to the International Geophysical Year (IGY) (1957–1958)

The inclusion of the pre-1957 period is a novelty of JRA-3Q in Japanese reanalyses. This period is important in that a number of disasters occurred in Japan that caused significant damage. It is also a period when international regular radiosonde observations had not yet been established on a global basis, and there are few available observations prior to 1957. It is therefore important to carefully check the quality of the reanalysis data before using them. In this subsection, we discuss the representation of pre-IGY weather.

Figure 28 shows the coverage of surface pressures and upper-level observations used in JRA-3Q for each year. In 1959, the number of surface pressures doubled compared with 1947, so that they covered most of the Northern Hemisphere and also spread to the

Southern Hemisphere, including Africa and South America. A similar trend can be seen for upper-level observations. There were almost no upper-level observations in 1947, but in 1959 upper-level observations covered most areas of the Northern Hemisphere, with comparable numbers of observations in 1959 and 2020.

Figure 29 shows the time series of background departures of surface pressure from land stations. The RMS of background departure decreased with time in Fig. 29, which indicates that the consistency between the observations and the first guess tended to improve. This improvement is likely the result of the steady increase in the number of various observations described in Subsection 5.3. The JRA-3Q has also a smaller RMS than the JRA-55 except before the late 1960s, meaning that consistency with surface pressure observations basically improved. The deterioration of the RMS before the late 1960s is probably due to the fact that the background error covariance of JRA-3Q has a shorter horizontal correlation length than that of JRA-55, which means that the first guess could not be adequately corrected in the period of sparse observations. In addition, the RMS was about twice as large in 1947, before the IGY, as it was in 1959. This result implies that there were issues with the quality of the reanalysis products, especially in the 1940s.

In the following subsections, we describe two examples of representative extreme weather events before the IGY: Typhoon Kathleen which brought heavy rainfall in September 1947 and Typhoon Marie (also known as the Toyamaru Typhoon in Japan) which brought strong wind in September 1954, and we then examine their representation in JRA-3Q. Figure 30 shows relevant geographical names in Japan.

a. Typhoon Kathleen

Typhoon Kathleen passed over the southern tip of the Boso Peninsula on 15 September 1947. Kathleen activated a front that had been stalled near Japan and it resulted in heavy rainfall in the Kanto and Tohoku regions. In the southern Kanto region, the Tone River and the Arakawa River burst their banks, and many homes were flooded from eastern Saitama Prefecture to Tokyo. The disaster caused by this flooding became a lesson of the history for flood control policies in the Tokyo metropolitan area (e.g., Cabinet Office 2021).

Figure 31 shows mean sea level pressures in the JRA-3Q, 20CRv3, and CERA-20C (Laloyaux et al. 2018) reanalyses at 06 UTC on 14 September 1947, when Typhoon Kathleen approached Japan, along with a weather map analyzed at that time. JRA-3Q and 20CRv3 both show Typhoon Kathleen in almost the same position as the weather map analyzed at that time. In CERA-20C, however, the low-pressure area corresponding to Typhoon Kathleen is less well represented, and its position is shifted to the south compared with the weather map. CERA-20C assimilates the best tracks from IBTrACS but Laloyaux (2016) has pointed out that many of them were rejected by the CERA-20C data assimilation system. The weaker representation of Typhoon Kathleen in CERA-20C suggests that such rejection may also have occurred in this case.

Figure 32 shows time series of three-hour accumulated precipitation at Tokyo, Hamamatsu, Maebashi, and Sendai stations in the JRA-3Q, 20CRv3, and CERA-20C reanalyses and in the observations. The reanalysis results are generally consistent with the observations, in that each shows precipitation maxima between 14 and 15 September, but they differ in the details. In the reanalyses, precipitation tends to be underestimated, the timing of the peak of precipitation at Tokyo is about half a day earlier than the observed peak, and the temporal variation of precipitation at Hamamatsu is not well represented. These discrepancies may be due to the coarse temporal and spatial resolution of the reanalyses, and a lack of available observations may have compromised their quality. To improve representation of extreme weather events, it will be necessary to increase the spatiotemporal resolution of reanalyses and to further enrich past observations by using additional rescued data.

b. Typhoon Marie

Typhoon Marie (known as the Toyamaru Typhoon in Japan) made landfall in Kagoshima at a very high translation speed, moved across eastern Kyushu and the Chugoku region, and then moved into the Sea of Japan and approached Hokkaido while developing further. The continued development of Typhoon Marie even after it entered the Sea of Japan resulted in wind speeds of 30 m s^{-1} or higher over western Japan, Tohoku, and Hokkaido. Typhoon Marie's strong winds sank five Seikan ferry ships, including the ferry Toyamaru, which provided transport between Hakodate and Aomori, and it killed more than one thousand passengers.

Figure 33 shows mean sea level pressure for the reanalyses and the weather map for 00 UTC on 26 September 1954, when Typhoon Marie crossed the Japanese archipelago. Each reanalysis clearly represents the typhoon and is generally consistent with the weather map analyzed at that time.

Figure 34 shows time series of 10-m wind speeds at Kumamoto, Hiroshima, Tsuruga, and Hakodate stations. Each of the reanalyses generally reproduced the peak wind speed seen on 25 and 26 September. The small differences in mean sea level pressure and 10-m wind speeds between the JRA-3Q, 20CRv3, and CERA-20C reanalyses suggest that Typhoon Marie was accurately represented.

9.5 Impact of switching SST datasets

Because the SST datasets used in JRA-3Q switched from COBE-SST2 to MGDSST in June 1985, it is very important to assess the impact of this switch on the characteristics of the JRA-3Q products. This subsection illustrates the impacts on precipitation and latent heat fluxes by comparing JRA-3Q with JRA-3Q-COBE (details of this sub-product are given in Subsection 4.1).

Figure 35 shows horizontal SST gradients and precipitations from JRA-3Q and JRA-3Q-COBE in the western North Pacific and western North Atlantic domains averaged over 1986–

1990. Because JRA-3Q used a higher resolution SST dataset than JRA-3Q-COBE during this period, the horizontal SST gradients along the western boundary currents are steeper in JRA-3Q than in JRA-3Q-COBE. In the western North Pacific domain, JRA-3Q shows greater precipitation in the east of Japan than JRA-3Q-COBE, as in the previous study of Masunaga et al. (2018), which demonstrated the impact of different ocean boundary conditions on precipitation in atmospheric reanalyses. In the western North Atlantic domain, JRA-3Q shows greater precipitation along the eastern coast of the North American continent than JRA-3Q-COBE. The difference is about half the standard deviation of the interannual variability of precipitation. In these regions of large precipitation differences, impacts on vertical motion reach the middle and upper troposphere, and different strength of upward motion—stronger in JRA-3Q than in JRA-3Q-COBE (not shown)—is also consistent with the previous study of Masunaga et al. (2018).

The impacts of differences in the specifications of MGDSST and COBE-SST2 are also apparent over lakes. Figure 36 compares the latent heat fluxes of JRA-3Q and JRA-3Q-COBE in northern North America averaged over 1986–1990. The latent heat fluxes over lakes are larger in JRA-3Q than in JRA-3Q-COBE. The difference amounts to about 30 W m^{-2} over the Great Lakes, which is comparable to the difference in the Gulf Stream region. In the original MGDSST, analyses of lake surface temperatures over the Great Lakes were not generated but instead were left as missing values. As a substitute that takes account of the dependence of surface temperature on latitude and elevation, those missing surface temperatures over lakes in MGDSST have been replaced in JRA-3Q with zonal mean SSTs over the sea at the same latitude after elevation correction. Those temperatures are then used as lower-boundary conditions to calculate the latent heat flux over lakes. In the original COBE-SST2, the surface temperature over major lakes was processed in the analysis so that temperatures become close to the climatology where there are no observations. This difference in specifications of MGDSST and COBE-SST2 is most likely the cause of the difference in the latent heat flux over lakes. It should also be noted that the water temperature (i.e., surface temperature over the sea and lakes) in the JRA-3Q product is the lower-boundary condition used by the JRA-3Q assimilation system and is not identical to the temperature of the original SST datasets, as mentioned above.

Care is needed in using the JRA-3Q products, especially variables that have large sensitivity to lower-boundary conditions, for analyzing low-frequency variability and trends across the two periods (until May 1985 and from June 1985) during which the different SST datasets were used. Impacts on the JRA-3Q products could arise not only from the difference between the SST datasets themselves, but also from the difference in how they are specified as lower-boundary conditions. Comparison between JRA-3Q and JRA-3Q-COBE will provide useful insights regarding impacts on other variables and spatiotemporal scales of interest as well.

10. Conclusions

The JMA has produced the JRA-3Q reanalysis with the state-of-the-art JMA global NWP system to improve the quality and extend the period of long-term reanalysis products by addressing the issues identified in JRA-55. JRA-3Q uses results of developments in the operational global NWP system, in boundary conditions, and in forcing fields since JRA-55. JRA-3Q covers the period from September 1947 and extends about 10 years further back in time than JRA-55, a period during which many typhoons caused serious disasters in Japan. New datasets of past observations have also been assimilated, including rescued historical observations and reprocessed satellite data supplied by meteorological and satellite centers worldwide. The improvement of the data assimilation system over that used for JRA-55 is evidenced by two-day forecast scores and background fits to radiosonde temperatures.

The large upward imbalance in the global mean net energy flux at the TOA and at the surface, one of the major problems of JRA-55, has been significantly reduced. The agreement with observational best estimates is better than was achieved with JRA-55. Although there are still differences, this better agreement is due to overall improvements in parameterizations of various physical processes in the forecast model. Energy and water budgets need to be further improved for better understanding of climate responses to anthropogenic and natural forcings. The artificial decrease in the detection of TCs seen in

JRA-55 has been resolved by the use of a TCB generation method based on the JMA operational system. TC representation has also been improved compared with JRA-55; the central pressures and wind speeds are now more realistic. The representation of the lower-stratospheric cooling trend has been improved, most likely by the use of ozone reanalysis data generated by MRI-CCM2.1 for the entire period as well as by improved bias correction for radiosonde temperatures. The warm bias in the upper troposphere has been significantly reduced, and the cold bias in the lower troposphere has been mitigated. The significant reduction or elimination of the dry bias in the middle troposphere of the forecast model has made JRA-3Q less susceptible to changes and evolutions in the observing system compared with JRA-55 and has thereby improved the homogeneity of humidity analysis. The bias of excess precipitation in the tropics has been reduced, and JRA-3Q shows more stable interannual variations of the precipitation anomalies than JRA-55. For the pre-1957 period, which is first included in Japanese reanalyses, major typhoons, such as Typhoon Kathleen and Typhoon Marie, are clearly represented in the mean sea level pressure field of JRA-3Q, and the pressure fields are generally consistent with the original weather map analyzed at that time.

Several problems have also been identified in our initial quality assessment. Stratospheric warming after major volcanic eruptions is smaller than expected, primarily due to the fact that the interannual variations of volcanic aerosols are not taken into account in the forecast model. In addition, the background error covariances used for JRA-3Q are optimized for the current enhanced observing system with a shorter horizontal correlation length than the ones used for JRA-55, which might be why errors in background fields were not sufficiently corrected where observations were sparse. The latter problem is most likely the main cause of the slight deterioration in the consistency with radiosonde temperatures in the middle troposphere prior to the late 1970s compared with JRA-55. Incorporating forcing in line with actual year-to-year variations and adaptive background error covariances will be a future challenge. It should also be noted that the SST datasets used in JRA-3Q switched from COBE-SST2 to MGDSST in June 1985. Care is needed in using the JRA-3Q products, especially variables that have large sensitivity to lower-boundary conditions, for analyzing low-frequency variability and trends.

Future reanalyses should benefit from the latest NWP techniques, such as ensemble data assimilation and all-sky satellite radiance assimilation, which should enable better use of existing observations, including rain- and cloud-affected radiances. Also, research and development of land and ocean data assimilation needs to be promoted to further improve the quality of land and ocean boundary conditions for reanalyses. Observational constraints on soil wetness, in which JRA-3Q is lacking, should improve the representation of the water cycle over land. Ocean data assimilation has potential advantages over traditional SST analyses in terms of temporal resolution and the ability of such assimilation to produce better estimates in regions where data are sparse. These potential areas of improvement should be explored in future reanalyses.

Data Availability Statement

The JRA-3Q and JRA-55 reanalysis data are provided via collaborative organizations listed in the JRA website (https://jra.kishou.go.jp). The JRA-25 and CFSR reanalysis data are provided from the NCAR website (https://rda.ucar.edu/datasets/). The ERA5, ERA-Interim, CERA-20C, and ERA-40 reanalysis data can be obtained from the ECMWF website (https://www.ecmwf.int/en/forecasts/datasets/browse-reanalysis-datasets). The MERRA-2 and MERRA reanalysis data can be obtained from the NASA website (https://disc.gsfc.nasa.gov/datasets/). The 20CRv3 and NCEP/NCAR reanalysis data can be downloaded from the NOAA Physical Sciences Laboratory website (https://psl.noaa.gov/data/gridded/index.html).

The observational best tracks are available on the JTWC and NHC websites (https://www.metoc.navy.mil/jtwc/jtwc.html; https://www.aoml.noaa.gov/hrd/data_sub/re_anal.html).

The HadCRUT5 analysis and HadAT2 datasets are provided by the Met Office Hadley Centre (https://www.metoffice.gov.uk/hadobs/). The NOAAGlobalTemp dataset is provide by NCEI (https://www.ncei.noaa.gov/products/land-based-station/noaa-global-temp), the

GISTEMP dataset by the NASA Goddard Institute for Space Studies (https://data.giss.nasa.gov/gistemp/), and the Berkeley Earth dataset from https://berkeleyearth.org/data/. The RSS v4.0 microwave temperature sounder product is provided from https://www.remss.com/measurements/upper-air-temperature/ and the UAH v6.0 product from https://www.nsstc.uah.edu/data/msu/v6.0/. The NOAA v4.1 microwave temperature sounder product and NOAA v3.0 stratospheric temperature product are provided by the NOAA National Environmental Satellite Data and Information Service (https://www.star.nesdis.noaa.gov/pub/smcd/emb/mscat/data/). The SSU and MLS stratospheric temperature products are provided by the University Corporation for Atmospheric Research (UCAR) (https://acomstaff.acom.ucar.edu/randel/SSU%20data.html).

The re-processed level-2 dataset estimated from GNSS-RO can be obtained from the UCAR website (https://www.cosmic.ucar.edu/). The GPCP precipitation dataset can be provided from the NOAA Physical Sciences Laboratory website (https://psl.noaa.gov/data/gridded/data.gpcp.html). The TRMM precipitation dataset can be downloaded from the Japan Aerospace Exploration Agency website (https://gportal.jaxa.jp/).

The CERES-EBAF satellite observations used to validate the energy budget are available from https://ceres.larc.nasa.gov/data/; the air-sea flux dataset (OAflux) is available from https://oaflux.whoi.edu/.

Acknowledgments

The JRA-3Q project was conducted in cooperation with the relevant departments of the JMA, and the data assimilation system used in JRA-3Q is based on the results of many years of development of NWP techniques in the Numerical Prediction Division. At MSC, AMV data from GMS and MTSAT were reprocessed. SST and sea ice data were provided by the Climate Prediction Division and the Office of Marine Prediction. The Climate Prediction Division and MRI also contributed to the quality assessment of JRA-3Q.

Observations used in JRA-3Q were provided by many organizations, as shown in Appendix B. For the assimilation of satellite radiances, we used RTTOV-10.2 developed by the European Organisation for the Exploitation of Meteorological Satellites (EUMETSAT) Satellite Application Facility on Numerical Weather Prediction (NWP SAF). The GNSS-RO ROPP-8.0 developed by the EUMETSAT Radio Occultation Meteorology Satellite Application Facility (ROM SAF) was used for bending angle assimilation.

HN and MD were supported by Japan Society for the Promotion of Science KAKENHI grant numbers (JP18K03748, JP20H05171, JP22H04493) and by grant number JP20K04070, respectively.

The members of the Advisory Panel for JRA, chaired by Prof. Toshiki Iwasaki of Tohoku University, provided valuable advice on various aspects related to the reanalysis.

The authors would like to express their deepest gratitude to all those who have contributed to the JRA-3Q project.

Appendix A: Acronyms

20CR	20th Century Reanalysis
2D-OI	Two-dimensional OI
4D-Var	Four-dimensional variational analysis
AIRS	Atmospheric Infrared Sounder
AMI	Active Microwave Instrument
AMSR2	Advanced Microwave Scanning Radiometer-2
AMSR-E	Advanced Microwave Scanning Radiometer for EOS
AMSU	Advanced Microwave Sounding Unit
AMV	Atmospheric motion vector
AR6	Sixth Assessment Report of IPCC
ASCAT	Advanced Scatterometer
ATMS	Advanced Technology Microwave Sounder
AVHRR	Advanced Very High Resolution Radiometer
CAPE	Convective available potential energy
CCM	Chemistry climate model
CDR	Climate data record

CERES-EBAF the Clouds and the Earth's Radiant Energy System (CERES) Energy Balanced and Filled (EBAF)

CFSR Climate Forecast System Reanalysis

CHAMP Challenging Mini-satellite Payload

CHUAN Comprehensive Historical Upper-Air Network

CIMSS Cooperative Institute for Meteorological Satellite Studies

CIRES Cooperative Institute for Research in Environmental Sciences

CLASS Comprehensive Large Array-data Stewardship System

CMIP5 Coupled Model Intercomparison Project Phase 5

CMIP6 Coupled Model Intercomparison Project Phase 6

CM SAF Satellite Application Facility on Climate Monitoring

COBE Centennial In Situ Observation-based Estimates of the Variability of SSTs and Marine Meteorological Variables

CONT-I Tropospheric aerosol profile for an average rural-continental region

COSMIC Constellation Observing System for Meteorology, Ionosphere, and Climate

CrIS Cross-track Infrared Sounder

CSR Clear sky radiance

DCAPE Dynamic CAPE generation rate

DMSP Defense Meteorological Satellite Program

ECMWF	European Centre for Medium-Range Weather Forecasts
EOS	Earth Observing System (NASA)
EPS	Ensemble Prediction System
ERA	ECMWF Reanalysis
ERA-40	A 45-year ERA from September 1957 to August 2002
ERA5	the fifth generation ECMWF reanalysis
ERS	European Remote Sensing Satellite
EUMETSAT	European Organisation for the Exploitation of Meteorological Satellites
FCDR	Fundamental climate data record
GAME	GEWEX Asia Monsoon Experiment
GEO	Geostationary
GEWEX	Global Energy and Water Cycle Experiment
GISTEMP	Goddard Institute for Space Studies Surface Temperature
GMI	GPM Microwave Imager
GMS	Geostationary Meteorological Satellite
GNSS	Global Navigation Satellite System
GNSS-RO	GNSS - Radio Occultation
GOES	Geostationary Operational Environmental Satellite
GPCP	Global Precipitation Climatology Project

GPM	Global Precipitation Measurement
GRACE	Gravity Recovery and Climate Experiment
GSM	Global Spectral Model
HadAT	Hadley Centre’s radiosonde temperature product
HadCRUT	Met Office Hadley Centre/Climatic Research Unit global temperature data set
HadISD	Hadley integrated surface dataset
HALOE	Halogen Occultation Experiment
HIRS	High Resolution Infrared Radiation Sounder
IASI	Infrared Atmospheric Sounding Interferometer
IBTrACS	International Best Track Archive for Climate Stewardship
ICA	Independent Column Approximation
ICOADS	International Comprehensive Ocean-Atmosphere Data Set
IGRA	Integrated Global Radiosonde Archive
IGY	International Geophysical Year
IMH	Institute of Meteorology and Hydrology (Mongolia)
ISD	Integrated Surface Database
IPCC	the Intergovernmental Panel on Climate Change
ISD	Integrated Surface Database
ISPD	International Surface Pressure Databank

ITCZ Inter Tropical Convergence Zone

JCDAS JMA Climate Data Assimilation System

JMA Japan Meteorological Agency

JRA-25 Japanese 25-year Reanalysis

JRA-55 Japanese 55-year Reanalysis

JRA-55C JRA-55 sub-product assimilating Conventional observations only

JRA-55CHS JRA-55C with High resolution SST

JRA-3Q Japanese Reanalysis for Three Quarters of a Century

JRA-3Q-COBE JRA-3Q with COBE-SST2

JSPS Japan Society for the Promotion of Science

JTWC Joint Typhoon Warning Center

LEO Low Earth orbit

MAR-I Tropospheric aerosol profile for a relatively clear maritime region

MASINGAR Model of Aerosol Species in the Global Atmosphere

MERRA-2 Modern-Era Retrospective Analysis for Research and Applications, version 2

Metop Meteorological Operational satellite

MGDSST Merged Satellite and In-Situ Data Global Daily Sea Surface Temperature

MHS Microwave Humidity Sounder

MISR Multi-angle Imaging Spectro-Radiometer

MLS Microwave Limb Sounder

MODIS Moderate Resolution Imaging Spectroradiometer

MRI Meteorological Research Institute (JMA)

MSC Meteorological Satellite Center (JMA)

MSG Meteosat Second Generation

MSU Microwave Sounding Unit

MT_CKD Mlawer–Tobin–Clough–Kneizys–Davies (water vapor continuum absorption model)

MTSAT Multi-functional Transport Satellite

MWRI Micro-Wave Radiation Imager

NASA National Aeronautics and Space Administration

NCAR National Center for Atmospheric Research

NCDC National Climate Data Center

NCEI National Centers for Environmental Information

NCEP National Centers for Environmental Prediction

NHC National Hurricane Center

NMC National Meteorological Center of NOAA

NOAA National Oceanic and Atmospheric Administration

NOAAGlobalTemp NOAA Global Surface Temperature Dataset

NWP Numerical Weather Prediction

NWP SAF Satellite Application Facility on Numerical Weather Prediction

OAflux Objectively Analyzed air-sea Fluxes for the global oceans

ODS Ozone-depleting substance

OI Optimal interpolation

OMI Ozone Monitoring Instrument

OSI SAF Satellite Application Facility on Ocean and Sea Ice

PDF Probability density function

PICA Practical ICA

QBO Quasi-biennial oscillation

QC Quality control

QuikSCAT Quick Scatterometer

RAOBCORE Radiosonde Observation Correction using Reanalyses

RCP Representative Concentration Pathway

RICH Radiosonde Innovation Composite Homogenization

RIHMI All-Russian Research Institute for Hydrometeorological Information

RISE RICH with solar elevation dependence

RMS Root-mean-square

ROM SAF Radio Occultation Meteorology Satellite Application Facility

ROPP	Radio Occultation Processing Package
RSMC	Regional Specialized Meteorological Centre designated by WMO
RSS	Remote Sensing Systems
RTTOV	Radiative Transfer for the TOVS
SAPHIR	Sondeur Atmospherique du Profil d'Humidite Intertropicale par Radiometrie
SCSMEX	South China Sea Monsoon Experiment
SEVIRI	Spinning Enhanced Visible and Infrared Imager
SiB	Simple Biosphere (model)
SIC	Sea ice concentration
SPARC	Stratosphere-Troposphere Processes and Their Role in Climate
SSM/I	Special Sensor Microwave/Imager
SSM/T-2	Special Sensor Microwave Water Vapor Profiler
SSMIS	Special Sensor Microwave Imager Sounder
SSP	Shared Socioeconomic Pathway
SST	Sea surface temperature
SSU	Stratospheric Sounding Unit
Suomi-NPP	Suomi National Polar-orbiting Partnership
SYNOP	Report of surface observation from a fixed land station
S-RIP	SPARC Reanalysis Intercomparison Project

TanDEM-X TerraSAR-X Add-on for Digital Elevation Measurement

TC Tropical cyclone

TCAC Tropical Cyclone Advisory Centre

TCB Tropical cyclone bogus

TCR Wind profile retrieval surrounding tropical cyclones

TCWCTropical Cyclone Warning Centre

TIROS Television and Infrared Observation Satellite

TMI TRMM Microwave Imager

TOA Top of the atmosphere

TOVS TIROS Operational Vertical Sounder

TRMM Tropical Rainfall Measurement Mission

UAH University of Alabama in Huntsville

UCAR University Corporation for Atmospheric Research

UNEP United Nations Environmental Programme

VTPR Vertical Temperature Profile Radiometer

WCRP World Climate Research Programme

WindSat Wind Satellite

WMO World Meteorological Organization

WDCGG World Data Centre for Greenhouse Gases

ZTD Zenith total delay

Appendix B: Observational data sources for JRA-3Q

Table B1 lists the suppliers of observations used in JRA-3Q, the type of data, and the period for which the data were used.

References

Abe, M., K. Shimoji, Y. Kosaka, and S. Kobayashi, 2021: AMV reprocessing activity for JRA-3Q at MSC/JMA. Fifteenth International Winds Workshop, 12–16 April 2021. [Available at https://cimss.ssec.wisc.edu/iwwg/iwwg_meetings.html (Accessed on 13 September 2023).]

Adler, R. F., G. J. Huffman, A. Chang, R. Ferraro, P.-P. Xie, J. Janowiak, B. Rudolf, U. Schneider, S. Curtis, D. Bolvin, A. Gruber, J. Susskind, P. Arkin, and E. Nelkin, 2003: The Version-2 Global Precipitation Climatology Project (GPCP) monthly precipitation analysis (1979–present). *J. Hydrometeor.*, **4**, 1147–1167.

Arakawa, A., and W. H. Schubert, 1974: Interaction of a cumulus cloud ensemble with the large-scale environment, Part I. *J. Atmos. Sci.*, **31**, 674–701.

Atkinson, G.D. and C. R. Holliday, 1977: Tropical Cyclone Minimum Sea Level Pressure/Maximum Sustained Wind Relationship for the Western North Pacific. Mon. Wea. Rev., 105(4), 421-427.

Beljaars, A. C. M. and A. A. M. Holtslag, 1991: Flux parameterization over land surfaces for atmospheric models. J. Appl. Meteor., 30, 327–341.

Bell, W., S. J. English, B. Candy, N. Atkinson, F. Hilton, N. Baker, S. D. Swadley, W. F. Campbell, N. Bormann, G. Kelly, and M. Kazumori, 2008: The assimilation of SSMIS radiances in numerical weather prediction models. IEEE Trans. Geosci. Remote Sens., 46, 884–900.

Borbas, E. E. and B. C. Ruston, 2010: The RTTOV UWiremis IR land surface emissivity module, AS Mission Report NWPSAF-MO-VS-042, EUMETSAT Numerical Weather Prediction Satellite Applications Facility, 24pp.

Bosilovich, M. G., F. R. Robertson, and J. Chen, 2011: Global energy and water budgets in MERRA. *J.Climate*, **24**, 5721–5739.

Bronnimann, S., and A. Stickler, 2013: The Comprehensive Historical Upper Air Network. Research Data Archive at NCAR, Computational and Information Systems Laboratory, doi:10.5065/AHPM-FC10. [Accessed on 29 Aug 2017.]

Buizza, R., P. Poli, M. Rixen, M. Alonso-Balmaseda, M. G. Bosilovich, S. Brönnimann, G. P. Compo, D. P. Dee, F. Desiato, M. Doutriaux-Boucher, M. Fujiwara, A. K. Kaiser-Weiss, S. Kobayashi, Z. Liu, S. Masina, P.-P. Mathieu, N. Rayner, C. Richter, S. I. Seneviratne, A. J. Simmons, J.-N. Thépaut, J. D. Auger, M. Bechtold, E. Berntell, B. Dong, M. Kozubek, K. Sharif, C. Thomas, S. Schimanke, A. Storto, M. Tuma, I. Välisuo, and A.

Vaselali, 2018: Advancing global and regional reanalyses. Bull. Amer. Meteor. Soc., 99, ES139–ES144.

Cabinet Office, 2021: White Paper Disaster Management in Japan, Cabinet Office, Japan, 156pp. [Available at https://www.bousai.go.jp/en/documentation/white_paper/pdf/2021/R3_hakusho_english.pdf (Accessed on 21 September 2023).]

Cavalieri, D. J., P. Gloersen, and W. J. Campbell, 1984: Determination of sea ice parameters from NUMBUS-7 SMMR. J. Geophys. Res., 89 (D4), 5355–5369.

Cavalieri, D. J., J. P. Crawford, M. R. Drinkwater, D. T. Eppler, L. D. Farmer, R. R. Jentz, and C. C. Wackerman, 1991: Aircraft active and passive microwave validation of sea ice concentration from the Defense Meteorological Satellite Program Special Sensor Microwave Imager. J. Geophys. Res., 96 (C12), 21989–22008.

Central Meteorological Observatory, 1948: Aerological data of Japan.

Chen, D., M. Rojas, B.H. Samset, K. Cobb, A. Diongue Niang, P. Edwards, S. Emori, S.H. Faria, E. Hawkins, P. Hope, P. Huybrechts, M. Meinshausen, S.K. Mustafa, G.-K. Plattner, and A.-M. Tréguier, 2021: Framing, context, and methods. In Climate Change 2021: The Physical Science Basis. Contribution of Working Group I to the Sixth Assessment Report of the Intergovernmental Panel on Climate Change [Masson-Delmotte, V., P. Zhai, A. Pirani, S.L. Connors, C. Péan, S. Berger, N. Caud, Y. Chen, L.

Goldfarb, M.I. Gomis, M. Huang, K. Leitzell, E. Lonnoy, J.B.R. Matthews, T.K. Maycock, T. Waterfield, O. Yelekçi, R. Yu, and B. Zhou (eds.)]. Cambridge University Press, Cambridge, United Kingdom and New York, NY, USA, 147–286,

Chou, M.-D., and L. Kouvaris, 1991: Calculations of transmission functions in the infrared CO2 and O3 bands. J. Geophys. Res., 96, 9003–9012.

Chou, M.-D., M. J. Suarez, X.-Z. Liang, and M. M.-H. Yan, 2001: A thermal infrared radiation parameterization for atmospheric studies. Technical report series on global modeling and data assimilation, NASA/TM-2001-104606, 19, National Aeronautics and Space Administration (NASA) Goddard Space Flight Center, USA, 68 pp. [Available at https://ntrs.nasa.gov/ (Accessed on 26 September 2023).].]

Chu, J.-H., C. R. Sampson, A. S. Levine, and E. Fukada, 2002: The joint typhoon warning center tropical cyclone best-tracks, 1945-2000. Naval Research Laboratory Tech. Rep. NRL/MR/7540-02-16, 28 pp. [Available online at https://www.metoc.navy.mil/jtwc/products/best-tracks/tc-bt-report.html (Accessed on 26 September 2023).]

Clough, S. A., M. W. Shephard, E. J. Mlawer, J. S. Delamere, M. J. Iacono, K. Cady-Pereira, S. Boukabara, and P. D. Brown, 2005: Atmospheric radiative transfer modeling: a summary of the AER codes. J. Quant. Spectrosc. Radiat. Transfer, 91, 233–244.

Collins, W. D., 2001: Parameterization of generalized cloud overlap for radiative calculations in general circulation models. J. Atmos. Sci., 58, 3224–3242.

Compo, G. P., et al., 2019: The International Surface Pressure Databank version 4. Research Data Archive at NCAR, Computational and Information Systems Laboratory, doi:10.5065/9EYR-TY90. [Accessed on 17 Mar 2020.]

Comiso, J. C., D. J. Cavalieri, C. L. Parkinson, and P. Gloersen, 1997: Passive microwave algorithms for sea ice concentration: A comparison of two techniques. Remote Sens. Environ., 60, 357–384.

Courtier, P., J.-N. Thépaut, and A. Hollingsworth, 1994: A strategy for operational implementation of 4D-Var, using an incremental approach. Quart. J. Roy. Meteor. Soc., 120, 1367–1387.

Davis, S. M., M. I. Hegglin, M. Fujiwara, R. Dragani, Y. Harada, C. Kobayashi, C. Long, G. L. Manney, E. R. Nash, G. L. Potter, S. Tegtmeier, T. Wang, K. Wargan, and J. S. Wright, 2017: Assessment of upper tropospheric and stratospheric water vapor and ozone in reanalyses as part of S-RIP, *Atmos. Chem. Phys.*, **17**, 12743–12778.

Deardorff, J.W., 1978: Efficient prediction of ground surface temperature and moisture with inclusion of a layer of vegetation. J. Geophys. Res.: Oceans, 83, 1889−1903.

Dee, D. P., and S. Uppala, 2009: Variational bias correction of satellite radiance data in the ERA-Interim reanalysis. Quart. J. Roy. Meteor. Soc., 135, 1830−1841.

Dee, D.P., Uppala, S.M., Simmons, A.J., Berrisford, P., Poli, P., Kobayashi, S., Andrae, U., Balmaseda, M.A., Balsamo, G., Bauer, P., Bechtold, P., Beljaars, A.C.M., van de Berg, L., Bidlot, J., Bormann, N., Delsol, C., Dragani, R., Fuentes, M., Geer, A.J., Haimberger, L., Healy, S.B., Hersbach, H., Hólm, E.V., Isaksen, L., Kållberg, P., Köhler, M., Matricardi, M., McNally, A.P., Monge-Sanz, B.M., Morcrette, J.-.-J., Park, B.-.-K., Peubey, C., de Rosnay, P., Tavolato, C., Thépaut, J.-.-N. and Vitart, F. (2011), The ERA-Interim reanalysis: configuration and performance of the data assimilation system. Q.J.R. Meteorol. Soc., 137: 553-597.

Derber, J. C., and W.-S. Wu, 1998: The use of TOVS cloud-cleared radiances in the NCEP SSI analysis system. Mon. Wea. Rev., 126, 2287–2299.

Desroziers, G., L. Berre, B. Chapnik, and P. Poli, 2005: Diagnosis of observation, background and analysis error statistics in observation space. Quart. J. Roy. Meteor. Soc., 131, 3385–3396.

Deushi, M. and K. Shibata, 2011: Development of a Meteorological Research Institute Chemistry- Climate Model version 2 for the study of tropospheric and stratospheric chemistry. *Pap. Meteor. Geophys*., **62**, 1–46.

Dobbie, J. S., J. Li, and P. Chýlek, 1999: Two- and four-stream optical properties for water clouds and solar wavelengths. J. Geophys. Res., 104, 2067–2079.

Dunn, R. J. H., 2019, HadISD version 3: monthly updates. Hadley Centre Tech. Note. [Available at https://www.metoffice.gov.uk/research/library-and-archive/publications/science/climate-science-technical-notes/ (Accessed on 13 September 2023).]

Durre, I., X. Yin, R. S. Vose, S Applequist, and J. Arnfield, 2016: Integrated Global Radiosonde Archive (IGRA), Version 2. NOAA NCEI, doi:10.7289/V5X63K0Q. [Accessed on 29 Jul 2017.]

Eyre, J. R. and W. P. Menzel, 1989: Retrieval of Cloud Parameters from Satellite Sounder Data: A Simulation Study. J. Appl. Meteor. Climat., 267 – 275.

Eyring, V., S. Bony, G. A. Meehl, C. A. Senior, B. Stevens, R. J. Stouffer, and K. E. Taylor, 2016: Overview of the Coupled Model Intercomparison Project Phase 6 (CMIP6) experimental design and organization, Geosci. Model Dev., 9, 1937–1958.

Fiorino, M., 2002: Analysis and forecasts of tropical cyclones in the ECMWF 40-year reanalysis (ERA40). 25th Conference on Hurricanes and Tropical Meteorology, CA, USA, 261–264.

Forster, P., T. Storelvmo, K. Armour, W. Collins, J.-L. Dufresne, D. Frame, D.J. Lunt, T. Mauritsen, M.D. Palmer, M. Watanabe, M. Wild, and H. Zhang, 2021: The Earth’s Energy Budget, Climate Feedbacks, and Climate Sensitivity. In Climate Change 2021: The Physical Science Basis. Contribution of Working Group I to the Sixth Assessment Report of the Intergovernmental Panel on Climate Change [Masson-Delmotte, V., P. Zhai, A. Pirani, S.L. Connors, C. Péan, S. Berger, N. Caud, Y. Chen, L. Goldfarb, M.I.

Gomis, M. Huang, K. Leitzell, E. Lonnoy, J.B.R. Matthews, T.K. Maycock, T. Waterfield, O. Yelekçi, R. Yu, and B. Zhou (eds.)]. Cambridge University Press, Cambridge, United Kingdom and New York, NY, USA, pp. 923–1054, doi:10.1017/9781009157896.009 (Accessed on 26 September 2023).

Freeman, E., S. D. Woodruff, S. J. Worley, S. J. Lubker, E. C. Kent, W. E. Angel, D. I. Berry, P. Brohan, R. Eastman, L. Gates, W. Gloeden, Z. Ji, J. Lawrimore, N. A. Rayner, G. Rosenhagen, and S. R. Smith, 2017: ICOADS Release 3.0: A major update to the historical marine climate record. Int. J. Climatol. 37, 2211–2237.

Fu, Q., and K. N. Liou, 1992: On the correlated k-distribution method for radiative transfer in nonhomogeneous atmospheres. J. Atmos. Sci., 49, 2139–2156.

Fujiwara, M., and co-authors, 2017: Introduction to the SPARC Reanalysis Intercomparison Project (S-RIP) and overview of the reanalysis systems. *Atmos. Chem. Phys.*, **17**, 1417-1452, https://doi.org/10.5194/acp-17-1417-2017 (Accessed on 26 September 2023).

Gelaro, R., McCarty, W., Suárez, M. J., Todling, R., Molod, A., Takacs, L., Randles, C. A., Darmenov, A., Bosilovich, M. G., Reichle, R., Wargan, K., Coy, L., Cullather, R., Draper, C., Akella, S., Buchard, V., Conaty, A., da Silva, A. M., Gu, W., Kim, G., Koster, R., Lucchesi, R., Merkova, D., Nielsen, J. E., Partyka, G., Pawson, S., Putman, W., Rienecker, M., Schubert, S. D., Sienkiewicz, M., & Zhao, B. (2017). The Modern-Era

Retrospective Analysis for Research and Applications, Version 2 (MERRA-2), J.Climate, 30, 5419-5454.

Geleyn, J.-F., and A. Hollingsworth, 1979: An economical analytical method for the computation of the interaction between scattering and line absorption of radiation. Beitr. Phys. Atmos., 52, 1–16.

Haimberger, L., C. Tavolato, and S. Sperka, 2008: Toward elimination of the warm bias in historic radiosonde temperature records--Some new results from acomprehensive intercomparison of upper-air data. J.Climate, 21, 4587–4606.

Haimberger, L., C. Tavolato, and S. Sperka. 2012: Homogenization of the global radiosonde temperature dataset through combined comparison with reanalysis background series and neighboring stations. J. Climate, 25, 8108–8131.

Han, J. and H.-L. Pan, 2011: Revision of Convection and Vertical Diffusion Schemes in the NCEP Global Forecast System. Weather and Forecasting, 26, 520–533.

Hans I., M. Burgdorf, S. A. Buehler, M. Prange, T. Lang, and V. O. John, 2019: An uncertainty quantified fundamental climate data record for microwave humidity sounders. Remote Sens., 11, 548, doi:10.3390/rs11050548 (Accessed on 26 September 2023).

Harada, Y., H. Kamahori, C. Kobayashi, H. Endo, S. Kobayashi, Y. Ota, H. Onoda, K. Onogi, K. Miyaoka, and K. Takahashi, 2016: The JRA-55 reanalysis: Representation of atmospheric circulation and climate variability, J. Meteor. Soc. Japan, 94, 269–302.

Hatsushika, H., J. Tsutsui, M. Fiorino, and K. Onogi, 2006: Impact of wind profile retrievals on the analysis of tropical cyclones in the JRA-25 reanalysis. J. Meteor. Soc. Japan, 84, 891–905.

Healy, S., 2008: Assimilation of GPS radio occulation measurements at ECMWF. Proceedings of GRAS SAF Workshop on Applications of GPS radio occultation measurements, ECMWF, June 16-18.

Hersbach, H., B. Bell, P. Berrisford, S. Hirahara, A Horányi, J. Muñoz-Sabater, J. Nicolas, C. Peubey, R. Radu, D. Schepers, A. Simmons, C. Soci, S. Abdalla, X. Abellan, G. Balsamo, P. Bechtold, G. Biavati, J. Bidlot, M. Bonavita, G. De Chiara, P. Dahlgren, D. Dee, M. Diamantakis, R. Dragani, J. Flemming, R. Forbes, M. Fuentes, A. Geer, L. Haimberger, S. Healy, R. J. Hogan, E. Hólm, M. Janisková, S. Keeley, P. Laloyaux, P. Lopez, C. Lupu, G. Radnoti, P. de Rosnay, I. Rozum, F. Vamborg, S. Villaume, and J.-N. Thépaut, 2020: The ERA5 global reanalysis. Quart. J. Roy. Meteor. Soc., 146, 1999–2049.

Hirahara, S., M. Ishii, and Y. Fukuda, 2014: Centennial-scale sea surface temperature analysis and its uncertainty. J. Climate, 27, 57–75.

Hu, Y. X., and K. Stamnes, 1993: An accurate parameterization of the radiative properties of water clouds suitable for use in climate models. J. Climate, 6, 728–742.

Huang, B., M. J. Menne, T. Boyer, E. Freeman, B. E. Gleason, J. H. Lawrimore, C. Liu, J. J. Rennie, C. J. Schreck III, F. Sun, R. Vose, C. N. Williams, X. Yin, and H.-M. Zhang, 2020: Uncertainty estimates for sea surface temperature and land surface air temperature in NOAAGlobalTemp Version 5. J. Climate, 33, 1351–1379.

Huffman, G. J., R. F. Adler, D. T. Bolvin, G. Gu, E. J. Nelkin, K. P. Bowman, Y. Hong, E. F. Stocker, and D. B. Wolff, 2007: The TRMM Multisatellite Precipitation Analysis (TMPA): Quasi-global, multiyear, combined-sensor precipitation estimates at fine scales. *J. Hydrometeor.*, **8**, 38–55

Ingleby, B., 2014: Global assimilation of air temperature, humidity, wind and pressure from surface stations. Quart. J. Roy. Meteor. Soc., doi: 10.1002/qj.2372 (Accessed on 26 September 2023)

Inoue, T., 1985: On the Temperature and Effective Emissivity Determination of Semi-Transparent Cirrus Clouds by Bi-Spectral Measurements in the 10 μm Window Region. J. Meteor. Soc. Japan, 63, 88–99.

Ishii, M., A. Shouji, S. Sugimoto, and T. Matsumoto, 2005: Objective analyses of sea-surface temperature and marine meteorological variables for the 20th century using ICOADS and the Kobe collection. Int. J. Climatol., 25, 865–879.

Iwamura, K., and H. Kitagawa, 2008: An upgrade of the JMA operational global NWP model. CAS/JSC WGNE Res. Activ. Atmos. Oceanic Modell., 38, 6.03-6.04. [Available at https://wgne.net/publications/wgne-blue-book/ (Accessed on 13 September 2023).]

JMA, 1961: Official Report of Typhoon Vera. Japan Meteorological Agency.

JMA, 2007: Outline of the operational numerical weather prediction at the Japan Meteorological Agency. Appendix to WMO Technical Progress Report on the Global Data-Processing and Forecasting System and Numerical Weather Prediction, JMA, Japan, 194pp. [Available at https://www.jma.go.jp/jma/jma-eng/jma-center/nwp/nwp-top.htm (Accessed on 13 September 2023).]

JMA, 2013: Outline of the operational numerical weather prediction at the Japan Meteorological Agency. Appendix to WMO Technical Progress Report on the Global Data-processing and Forecasting System (GDPFS) and Numerical Weather Prediction (NWP) Research, JMA, Japan, 188pp. [Available at https://www.jma.go.jp/jma/jma-eng/jma-center/nwp/nwp-top.htm (Accessed on 13 September 2023).]

JMA, 2015: Bugs in JRA-55 snow depth analysis. JMA, Japan, 19pp. [Available at https://jra.kishou.go.jp/JRA-55/index_en.html#quality (Accessed on 13 September 2023).]

JMA, 2019: Outline of the operational numerical weather prediction at the Japan Meteorological Agency. Appendix to WMO Technical Progress Report on the Global Data-processing and Forecasting System (GDPFS) and Numerical Weather Prediction (NWP) Research, JMA, Japan, 229pp. [Available at https://www.jma.go.jp/jma/jma-eng/jma-center/nwp/nwp-top.htm (Accessed on 13 September 2023).]

JMA, 2022a: JRA-3Q data format: 1.25 degree latitude/longitude grid data. JMA, Japan, 20 pp. [Available at https://jra.kishou.go.jp/JRA-3Q/index_en.html (Accessed on 13 September 2023).]

JMA, 2022b: JRA-3Q data format: Model grid data. JMA, Japan, 29 pp. [Available at https://jra.kishou.go.jp/JRA-3Q/index_en.html (Accessed on 13 September 2023).]

Kadowaki, T. and K. Yoshimoto, 2012: A new inner model with a higher horizontal resolution (TL319) in JMA's Global 4D-Var data assimilation system. CAS/JSC WGNE Res. Act. Atmos. Ocea. Model/WMO, 42, 1.09–1.10. [Available at https://wgne.net/publications/wgne-blue-book/ (Accessed on 13 September 2023).]

Kato, S., F. G. Rose, D. A. Rutan, T. E. Thorsen, N. G. Loeb, D. R. Doelling, X. Huang, W. L. Smith, W. Su, and S.-H. Ham, 2018: Surface irradiances of Edition 4.0 Clouds and the Earth's Radiant Energy System (CERES) Energy Balanced and Filled (EBAF) data product, J. Climate, 31, 4501–4527.

Kawai, H., and T. Inoue, 2006: A simple parameterization scheme for subtropical marine stratocumulus. SOLA, 2, 17–20.

Kawai, H., H. Yonehara, and M. Ujiie, 2013: Vertical layer placement in the eta coordinate for models with a high model top. CAS/JSC WGNE Res. Act. Atmos. Ocea. Model/WMO, 43, 3.03–3.04. [Available at https://wgne.net/publications/wgne-blue-book/

(Accessed on 13 September 2023).]

Kazumori, M., 2012: Assimilation experiments involving surface-sensitive microwave radiances in JMA's global data assimilation system. CAS/JSC WGNE Res. Act. Atmos. Ocea. Model/WMO, 42, 1.11–1.12. [Available at https://wgne.net/publications/wgne-blue-book/ (Accessed on 13 September 2023).]

Kazumori, M., 2016a: Assimilation of GPM microwave imager data in JMA's NWP systems. CAS/JSC WGNE Res. Act. Atmos. Ocea. Model/WMO, 46, 1.13–1.14. [Available at https://wgne.net/publications/wgne-blue-book/ (Accessed on 13 September 2023).]

Kazumori, M., 2016b: Assimilation of Megha-Tropiques/SAPHIR radiance data in JMA's global NWP system. CAS/JSC WGNE Res. Act. Atmos. Ocea. Model/WMO, 46, 1.17–1.18. [Available at https://wgne.net/publications/wgne-blue-book/ (Accessed on 13 September 2023).]

Knapp, K. R., M. C. Kruk, D. H. Levinson, H. J. Diamond, and C. J. Neumann, 2010: The International Best Track Archive for Climate Stewardship (IBTrACS): Unifying tropical cyclone best track data. Bull. Amer. Meteor. Soc., 91, 363–376.

Kobayashi, C., H. Endo, Y. Ota, S. Kobayashi, H. Onoda, Y. Harada, K. Onogi, and H. Kamahori, 2014: Preliminary results of the JRA-55C, an atmospheric reanalysis assimilating conventional observations only. SOLA, 10, 78–82.

Kobayashi, C., and K. Shibata, 2011: Evaluation of dynamical contribution to lower stratospheric ozone trends in northern mid-latitudes over the last three decades (1980-2006) using a chemical transport model. *J. Meteor. Soc. Japan*, **89**, 363–376.

Kobayashi, S., Y. Ota, Y. Harada, A. Ebita, M. Moriya, H. Onoda, K. Onogi, H. Kamahori, C. Kobayashi, H. Endo, K. Miyaoka, and K. Takahashi, 2015: The JRA-55 reanalysis: General specifications and basic characteristics. J. Meteor. Soc. Japan, 93, 5–48.

Kobayashi, S., P. Poli, and V. O. John, 2017: Characterisation of Special Sensor Microwave Water Vapor Profiler (SSM/T-2) radiances using radiative transfer simulations from global atmospheric reanalyses. Adv. Space Res., 59, 917–953.

Kosaka, Y. 2016: Assimilation of surface pressure in METAR. CAS/JSC WGNE Res. Activ. Atmos. Oceanic Modell., 46, 1.21-1.22. [Available at https://wgne.net/publications/wgne-blue-book/ (Accessed on 13 September 2023).]

Kurihara, Y., T. Sakurai, and T. Kuragano, 2006: Global daily sea surface temperature analysis using data from satellite microwave radiometer, satellite infrared radiometer and in-situ observations. Weather Service Bulletin, JMA, 73, Special issue, s1–s18 (in Japanese).

Kursinski, E. R., G. A. Hajj, J.T. Schofield, and R. P. Linfield, 1997: Observing Earth's atmosphere with radio occultation measurements using the Global Positioning System, *J. Geophys. Res.*, **102**, 23409–23465.

Laloyaux, P., E. de Boisseson, M. Balmaseda, J.-R. Bidlot, S. Broennimann, R. Buizza, P.

Dalhgren, D. Dee, L. Haimberger, H. Hersbach, Y. Kosaka, M. Martin, P. Poli, N. Rayner, E. Rustemeier, and D. Schepers, 2018: CERA-20C: A Coupled Reanalysis of the Twentieth Century. J. Adv. Model. Earth Syst., 10, 1172–1195.

Landsea, C.W., and J.L. Franklin, 2013: Atlantic hurricane database uncertainty and presentation of a new database format. Mon. Wea. Review, 141, 3576-3292. doi:10.1175/MWR-D-12-00254.1 (Accessed on 26 September 2023).

Lazzara, M. A., R. Dworak, D. A. Santek, B. T. Hoover, C. S. Velden and J. R. Key, 2014: High-latitude Atmospheric Motion Vectors from Composite Satellite Data. Journal of Applied Meteorology and Climatology, 53, 534 – 547.

Lenssen, N. J. L., G. A. Schmidt, J. E. Hansen, M. J. Menne, A. Persin, R. Ruedy, and D. Zyss, 2019: Improvements in the GISTEMP uncertainty model. J. Geophys. Res.: Atmos., 124, 6307–6326.

Lindner, T. H. and J. Li, 2000: Parameterization of the optical properties for water clouds in the infrared. J. Climate, 13, 1797–1805.

Loeb, N. G., D. R. Doelling, H. L. Wang, W. Y. Su, C. Nguyen, J. G. Corbett, L. S. Liang, C. Mitrescu, F. G. Rose, S. Kato, 2018: Clouds and the earth’s radiant energy system (CERES) energy balanced and filled (EBAF) top-of-atmosphere (TOA) edition-4.0 data product. J Climate, 31, 895–918.

Louis, J.-F., M. Tiedtke, and J.-F. Geleyn, 1982: A short history of the operational PBLparameterization at ECMWF. Workshop on Planetary Boundary Layer Parameterization, Reading, United Kingdom, 25–27 November 1981, ECMWF, 59–79.

Martin, G. M., D. W. Johnson, and A. Spice, 1994: The measurement and parameterization of effective radius of droplets in warm stratocumulus clouds. J. Atmos. Sci., 51, 1823–1842.

Masunaga, R., H. Nakamura, H. Kamahori, K. Onogi, and S. Okajima, 2018: JRA-55CHS: An atmospheric reanalysis produced with high-resolution SST. SOLA, 14, 6–13.

Matsumoto, T., M. Ishii, Y. Fukuda, and S. Hirahara, 2006: Sea ice data derived from microwave radiometer for climate monitoring. Proceedings of the 14th Conference on Satellite Meteorology and Oceanography, Atlanta, USA, 29 January – 3 February, 2006, P2.21.

Maycock, A. C., W. J. Randel, A. K. Steiner, A. Y. Karpechko, J. Christy, R. Saunders, D. W. J. Thompson, C.-Z. Zou, A. Chrysanthou, N. L. Abraham, H. Akiyoshi, A. T. Archibald, N. Butchart, M. Chipperfield, M. Dameris, M. Deushi, S. Dhomse, G. D. Genova, P. Jöckel, D. E. Kinnison, O. Kirner, F. Ladstädter, M. Michou, O. Morgenstern, F. O'Connor, L. Oman, G. Pitari, D. A. Plummer, L. E. Revell, E. Rozanov, A. Stenke, D. Visioni, Y. Yamashita, and G. Zeng, 2018: Revisiting the mystery of recent stratospheric temperature trends. Geophys. Res. Lett., 45, 9919–9933.

Mears, C. A., and F. J. Wentz, 2016: Sensitivity of satellite-derived tropospheric temperature trends to the diurnal cycle adjustment. J. Climate, 29, 3629–3646.

Mears, C. A., and F. J. Wentz, 2017: A satellite-derived lower-tropospheric atmospheric temperature dataset using an optimized adjustment for diurnal effects. J. Climate, 30, 7695–7718.

Meinshausen, M., Vogel, E., Nauels, A., Lorbacher, K., Meinshausen, N., Etheridge, D. M., Fraser, P. J., Montzka, S. A., Rayner, P. J., Trudinger, C. M., Krummel, P. B., Beyerle, U., Canadell, J. G., Daniel, J. S., Enting, I. G., Law, R. M., Lunder, C. R., O'Doherty, S., Prinn, R. G., Reimann, S., Rubino, M., Velders, G. J. M., Vollmer, M. K., Wang, R. H. J., and Weiss, R., 2017: Historical greenhouse gas concentrations for climate modelling (CMIP6), Geosci. Model Dev., 10, 2057–2116.

Mellor, G. L. and T. Yamada, 1974: A hierarchy of turbulence closure models for planetary boundary layers. J. Atmos. Sci., 31, 1791–1806.

Mellor, G. L. and T. Yamada, 1982: Development of a turbulence closure model for geophysical fluid problems. Rev. Geophys. Space Phys., 20, 851–875.

Moorthi, S. and M. J. Suarez, 1992: Relaxed Arakawa-Schubert: A parameterization of moist convection for general circulation models. Mon. Wea. Rev., 120, 978–1002.

Morice, C. P., J. J. Kennedy, N. A. Rayner, J. P. Winn, E. Hogan, R. E. Killick, R. J. H. Dunn, T. J. Osborn, P. D. Jones, and I. R. Simpson, 2021: An updated assessment of near-surface temperature change from 1850: the HadCRUT5 data set. J. Geophys.

Res.: Atmos., 126, e2019JD032361, doi:10.1029/2019JD032361 (Accessed on 26 September 2023).

Murakami, Y., and M. Kazumori, 2017: Assimilation of SSMIS humidity sounding channels into JMA's global NWP system. CAS/JSC WGNE Res. Act. Atmos. Ocea. Model/WMO, 47, 1.19–1.20. [Available at https://wgne.net/publications/wgne-blue-book/ (Accessed on 13 September 2023).]

Nagasawa, R., 2012: The problem of cloud overlap in the radiation process of JMA global NWP model. CAS/JSC WGNE Res. Act. Atmos. Ocea. Model/WMO, 42, 4.15–4.16. [Available at https://wgne.net/publications/wgne-blue-book/ (Accessed on 13 September 2023).]

Nakagawa, M., 2009: Outline of the high resolution global model at the Japan Meteorological Agency. RSMC Tokyo-Typhoon Center Technical Review, 11, JMA, Japan, 1-13. [Available at https://www.jma.go.jp/jma/jma-eng/jma-center/rsmc-hp-pub-eg/techrev.htm (Accessed on 26 September 2023).]

Nakajima, T. Y., K. Suzuki, and G. L. Stephens, 2010: Droplet growth in warm water clouds observed by the A-Train. Part I: Sensitivity analysis of the MODIS-derived cloud droplet sizes. J. Atmos. Sci., 67, 1884–1896.

Naoe, H., T. Matsumoto, K. Ueno, T. Maki, M. Deushi, and A. Takeuchi, 2020: Bias correction of multi-sensor total column ozone satellite data for 1978–2017. J. *Meteor.*

Soc. Japan, **98**, 353–377.

Okabe, I. 2019: Operational use of surface-sensitive clear-sky radiance data in JMA's global NWP system. CAS/JSC WGNE Res. Activ. Atmos. Oceanic Modell., 49, 1.15-1.16. [Available at https://wgne.net/publications/wgne-blue-book/ (Accessed on 13 September 2023).]

Okagaki, A. 2015: Assimilation of IASI and AIRS radiances at JMA. CAS/JSC WGNE Res. Activ. Atmos. Oceanic Modell., 45, 1.17-1.18. [Available at https://wgne.net/publications/wgne-blue-book/ (Accessed on 13 September 2023).]

Okamoto, N., M. D. Yamanaka, S.-Y. Ogino, H. Hashiguchi, N. Nishi, T. Sribimawati, and A. Numaguchi, 2003: Seasonal variations of tropospheric wind over Indonesia: comparison between collected operational radiosonde data and NCEP reanalysis for 1992-99. J. Meteor. Soc. Japan, 81. 829–850.

O'Neill, B. C., Tebaldi, C., van Vuuren, D. P., Eyring, V., Friedlingstein, P., Hurtt, G., Knutti, R., Kriegler, E., Lamarque, J.-F., Lowe, J., Meehl, G. A., Moss, R., Riahi, K., and Sanderson, B. M., 2016: The Scenario Model Intercomparison Project (ScenarioMIP) for CMIP6, Geosci. Model Dev., 9, 3461–3482.

Onogi, K., J. Tsutsui, H. Koide, M. Sakamoto, S. Kobayashi, H. Hatsushika, T. Matsumoto, N. Yamazaki, H. Kamahori, K. Takahashi, S. Kadokura, K. Wada, K. Kato, R. Oyama, T. Ose, N. Mannoji and R. Taira, 2007: The JRA-25 reanalysis. J. Meteor. Soc. Japan, 85, 369–432.

Owada, H. and M. Moriya, 2015: Recent updates on the use of GNSS RO data in JMA’s Operational Global Data Assimilation System. CAS/JSC WGNE Res. Activ. Atmos. Oceanic Modell., 45, 1.21-1.22. [Available at https://wgne.net/publications/wgne-blue-book/ (Accessed on 13 September 2023).]

Owada, H., Y. Hirahara, and M. Moriya, 2018: Recent updates on the usage of GNSS RO data in JMA’s Operational Global Data Assimilation System. CAS/JSC WGNE Res. Activ. Atmos. Oceanic Modell., 48, 1.19-1.20. [Available at https://wgne.net/publications/wgne-blue-book/ (Accessed on 13 September 2023).]

Painemal, D., and P. Zuidema, 2011: Assessment of MODIS cloud effective radius and optical thickness retrievals over the Southeast Pacific with VOCALS-Rex in situ measurements. J. Geophys. Res., 116, D24206, doi:10.1029/2011JD016155 (Accessed on 26 September 2023).

Parrish, D., and J. Derber, 1992: The National Meteorological Center’s spectral statistical interpolation analysis system. Mon. Wea. Rev., 120, 1747−1763.

Randall, D. and D.-M. Pan, 1993: Implementation of the Arakawa-Schubert cumulus parameterization with a prognostic closure. The representation of cumulus convection in numerical models, AMS Meteorological Monograph Series, 46, 137–144.

Randel, W. J., A. K. Smith, F. Wu, C.-Z. Zou, and H. Qian, 2016: Stratospheric temperature trends over 1979–2015 derived from combined SSU, MLS, and SABER satellite observations. J. Climate, 29, 4843–4859.

Randel, W. J., F. Wu, J. M. Russell III, A. Roche, and J. W. Waters, 1998: Seasonal cycles and QBO variations in stratospheric CH4 and H2O observed in UARS HALOE data. J. Atmos. Sci., 55, 163–185.

Rennie, M. P., 2010: The impact of GPS radio occultation assimilation at the Met Office. Quart. J. Roy. Meteor. Soc., 136, 116–131.

Rohde, R. A., and Z. Hausfather, 2020: The Berkeley Earth land/ocean temperature record. Earth Syst. Sci. Data, 12, 3469–3479.

Saha, S., Moorthi, S., Wu, X., Wang, J., Nadiga, S., Tripp, P., Behringer, D., Hou, Y., Chuang, H., Iredell, M., Ek, M., Meng, J., Yang, R., Mendez, M. P., van den Dool, H., Zhang, Q., Wang, W., Chen, M., & Becker, E. (2014). The NCEP Climate Forecast System Version 2, J. Climate, 27, 2185-2208.

Sato, N., P. J. Sellers, D. A. Randall, E. K. Schneider, J. Shukla, J. L. Kinter III, Y−T Hou, and E. Albertazzi, 1989a: Implementing the simple biosphere model (SiB) in a general circulation model: Methodologies and results. NASA contractor Rep., 185509, 76pp.

Sato, N., P. J. Sellers, D. A. Randall, E. K. Schneider, J. Shukla, J. L. Kinter III, Y−T Hou, and E. Albertazzi, 1989b: Effects of implementing the simple biosphere model (SiB) in a general circulation model. J. Atmos. Sci., 46, 2757–2782.

Saunders, R., 2008: RTTOV-9 science and validation report. EUMETSAT NWP SAF, 74pp. [Available at https://nwp-saf.eumetsat.int/site/software/rttov/ (Accessed on 13 September 2023).]

Saunders, R., J. Hocking, P. Rayer, M. Matricardi, A. Geer, N. Bormann, P. Brunel, F. Karbou, and F. Aires, 2012: RTTOV-10 science and validation report. EUMETSAT NWP SAF, 31pp. [Available at https://nwp-saf.eumetsat.int/site/software/rttov/ (Accessed on 13 September 2023).]

Scinocca, J. F., 2003: An accurate spectral nonorographic gravity wave drag parameterization for general circulation models. J. Atmos. Sci., 60, 667–682.

Sellers, P.J., Y. Mintz, Y.C. Sud, and A. Dalcher, 1986: A simple biosphere model (SiB) for use within general circulation models. J. Atmos. Sci., 43, 505–531.

Shibata, K., M. Deushi, T. T. Sekiyama, and H. Yoshimura, 2005: Development of an MRI chemical transport model for the study of stratospheric chemistry. *Pap. Geophys. Meteorol*., **55**, 75–119.

Shimokobe, A., 2012: Improvement of the Stratocumulus Parameterization Scheme in JMA’s Operational Global Spectral Model. CAS/JSC WGNE Res. Act. Atmos. Ocea. Model/WMO, 42, 4.17–4.18. [Available at https://wgne.net/publications/wgne-blue-book/ (Accessed on 13 September 2023).]

Simmons, A. J., P. D. Jones, V. da Costa Bechtold, A. C. M. Beljaars, P. W. Kållberg, S.

Saarinen, S. M. Uppala, P. Viterbo, and N. Wedi, 2004: Comparison of trends and low-frequency variability in CRU, ERA-40, and NCEP/NCAR analyses of surface air temperature. J. Geophys. Res., 109, D24115, doi:10.1029/2004JD005306.

Simmons, A. J., P. Poli, D. P. Dee, P. Berrisford, H. Hersbach, S. Kobayashi, and C. Peubey, 2014: Estimating low - frequency variability and trends in atmospheric temperature using ERA-Interim. Quart. J. Roy. Meteor. Soc., 140, 329–353.

Simmons, A. J., P. Berrisford, D. P. Dee, H. Hersbach, S. Hirahara, and J.-N. Thépaut, 2017: A reassessment of temperature variations and trends from global reanalyses and monthly surface climatological datasets. Quart. J. Roy. Meteor. Soc., 143, 101–119.

Simmons, A, C. Soci, J. Nicolas, B. Bell, P. Berrisford, R. Dragani, J. Flemming, L. Haimberger, S. Healy, H. Hersbach, A. Horányi, A. Inness, J. Munoz-Sabater, R. Radu, D. Schepers, 2020: Global stratospheric temperature bias and other stratospheric aspects of ERA5 and ERA5.1. ECMWF Technical Memorandum, 859, ECMWF, UK, 38 pp, doi:10.21957/rcxqfmg0 (Accessed on 26 September 2023).

Slingo, A., 1989: A GCM parameterization for the shortwave radiative properties of water clouds. J. Atmos. Sci., 46, 1419–1427.

Slivinski, L. C., G. P. Compo, J. S. Whitaker, P. D. Sardeshmukh, B. S. Giese, C. McColl, R. Allan, X. Yin, R. Vose, H. Titchner, J. Kennedy, L. J. Spencer, L. Ashcroft, S. Brönnimann, M. Brunet, D. Camuffo, R. Cornes, T. A. Cram, R. Crouthamel, F.

Domínguez-Castro, J. E. Freeman, J. Gergis, E. Hawkins, P. D. Jones, S. Jourdain, A. Kaplan, H. Kubota, F. Le Blancq, T.-C. Lee, A. Lorrey, J. Luterbacher, M. Maugeri, C. J. Mock, G. W. K. Moore, R. Przybylak, C. Pudmenzky, C. Reason, V. C. Slonosky, C. A. Smith, B. Tinz, B. Trewin, M. A. Valente, X. L. Wang, C. Wilkinson, K. Wood, P. Wyszyński, 2019: Towards a more reliable historical reanalysis: Improvements for version 3 of the Twentieth Century Reanalysis system, Quart. J. Roy. Meteor. Soc., 145, 2876–2908.

Smith, R. N. B., 1990: A scheme for predicting layer clouds and their water content in a general circulation model. Quart. J. Roy. Meteor. Soc., 116, 435–460.

Smith, A., N. Lott, and R. Vose, 2011: The Integrated Surface Database: Recent developments and partnerships. Bull. Amer. Meteor. Soc. 92, 704–708.

Spencer, R. W., J. R. Christy, and W. D. Braswell, 2017: UAH Version 6 global satellite temperature products: Methodology and results. Asia-Pac. J. Atmos. Sci., 53, 121–130.

Stuber et al., 2021: Data Rescue Activities, European Environment Agency, EEA/DIS/R0/20/001 Lot 1

Tanaka, T. Y., K. Orito, T. T. Sekiyama, K. Shibata, and M. Chiba, 2003: MASINGAR, a global tropospheric aerosol chemical transport model coupled with MRI/JMA98 GCM: Model description. Pap. Meteorol. Geophys., 53 (4), 119–138.

Taylor, K. E., R. J. Stouffer, and G. A. Meehl, 2012: An Overview of Cmip5 and the

Experiment Design. *Bull. Amer. Meteorol. Soc*., **93**, 485–498.

Thompson, D. W. J., D. J. Seidel, W. J. Randel, C.-Z. Zou, A. H. Butler, C. Mears, A. Osso, C. Long, and R. Lin, 2012: The mystery of recent stratospheric temperature trends. Nature, 491, 692–697.

Thorne, P. W., D. E. Parker, S. F. B. Tett, P. D. Jones, M. McCarthy, H. Coleman, and P. Brohan, 2005: Revisiting radiosonde upper-air temperatures from 1958 to 2002. J. Geophys. Res., 110, D18105, doi:10.1029/2004JD005753 (Accessed on 26 September 2023).

Trenberth, K. E., J. T. Fasullo, and J. Mackaro, 2011: Atmospheric moisture transports from ocean to land and global energy flows in reanalyses. *J. Climate*, **24**, 4907–4924

Uppala, S. M., P. W. Kållberg, A. J. Simmons, U. Andrae, V. Da Costa Bechtold, M. Fiorino, J. K. Gibson, J. Haseler, A. Hernandez, G. A. Kelly, X. Li, K. Onogi, S. Saarinen, N. Sokka, R. P. Allan, E. Andersson, K. Arpe, M. A. Balmaseda, A. C. M. Beljaars, L. Van De Berg, J. Bidlot, N. Bormann, S. Caires, F. Chevallier, A. Dethof, M. Dragosavac, M. Fisher, M. Fuentes, S. Hagemann, E. Hólm, B. J. Hoskins, L. Isaksen, P. A. E. M. Janssen, R. Jenne, A. P. McNally, J.-F. Mahfouf, J.-J. Morcrette, N. A. Rayner, R. W. Saunders, P. Simon, A. Sterl, K. E. Trenberth, A. Untch, D. Vasiljevic, P. Viterbo, and J. Woollen, 2005: The ERA-40 re-analysis. Quart. J. Roy. Meteor. Soc., 131, 2961–3012.

Valdivieso, M., K. Haines, M. Balmaseda, et al., 2017: An assessment of air–sea heat fluxes from ocean and coupled reanalyses. Climate Dyn., 49, 983–1008.

van de Berg, L., J. Gustafsson, and A. Yildirim, 2001: Reprocessing of atmospheric motion vectors from Meteosat image data. ECMWF ERA-40 Project Report Series, 3, ECMWF, UK, 159–168. [Available at https://www.ecmwf.int/en/publications/ (Accessed on 13 September 2023).]

Walsh, J. E., and W. L. Chapman, 2001: 20th-century sea-ice variations from observational data. Annals of Glaciology, 33, 444–448.

Wanzong, S., D. Santek, C. S. Velden, J. Daniels, D. Stettner, W. C. Bresky, and A. Bailey, 2014: Historical GOES AMV reprocessing. Twelfth International Winds Workshop, Copenhagen, Denmark. [Available at https://cimss.ssec.wisc.edu/iwwg/iwwg_meetings.html (Accessed on 13 September 2023).]

Wild, M., D. Folini, C. Schr, N. Loeb, E. G. Dutton, and G. König-Langlo, 2013: The global energy balance from a surface perspective. Climate Dyn., 40, 3107-3134

Wild, M., D. Folini, M. Z. Hakuba, C. Schär, S.I. Seneviratne, S. Kato, D. Rutan, C. Ammann, E.F. Wood, and G. König-Langlo, 2015: The energy balance over land and oceans: an assessment based on direct observations and CMIP5 climate models. Climate Dyn 44, 3393–3429

Wild, M., M. Z. Hakuba, D. Folini, P. Dörig-Ott, C. Schär, S. Kato, and C. N. Long, 2019:

The cloud-free global energy balance and inferred cloud radiative effects: an assessment based on 3 direct observations and climate models. Climate Dyn., 52, 4787–4812.

WMO, 1986: A preliminary cloudless standard atmosphere for radiation computation, World Climate Programme (WCP), 112, 53 pp.

WMO, World Data Centre for Greenhouse Gases (WDCGG) Data Summary, WDCGG No. 42, 97pp, 2018.

WMO (World Meteorological Organization), Scientific Assessment of Ozone Depletion: 2014, World Meteorological Organization, Global Ozone Research and Monitoring Project-Report No. 55, 416 pp., Geneva, Switzerland, 2014.

Xie, S., and M. Zhang, 2000: Impact of the convection triggering function on single-column model simulations. J. Geophys. Res., 105, D11, 14983–14996.

Yabu, S., 2013: Development of longwave radiation scheme with consideration of scattering by clouds in JMA global model. CAS/JSC WGNE Res. Activ. Atmos. Oceanic Modell., 43, 4.07–4.08. [Available at https://wgne.net/publications/wgne-blue-book/ (Accessed on 13 September 2023).]

Yabu, S., T. Y. Tanaka, and N. Oshima, 2017: Development of a multi-species aerosol-radiation scheme in JMA's global model. CAS/JSC WGNE Res. Activ. Atmos. Oceanic Modell., 47, 6.19–6.20. [Available at https://wgne.net/publications/wgne-blue-book/

(Accessed on 13 September 2023).]

Yamashita, K. 2014: Introduction of LEO-GEO and AVHRR Polar Atmospheric Motion Vectors into JMA’s Operational Global NWP System. CAS/JSC WGNE Res. Activ. Atmos. Oceanic Modell., 44, 1.25-1.26. [Available at https://wgne.net/publications/wgne-blue-book/ (Accessed on 13 September 2023).]

Yatagai, A., K. Kamiguchi, O. Arakawa, A. Hamada, N. Yasutomi, and A. Kitoh, 2012: APHRODITE: Constructing a long-term daily gridded precipitation dataset for Asia based on a dense network of rain gauges. Bull. Amer. Meteor. Soc., 93, 1401–1415.

Yonehara, H., M. Ujiie, T. Kanehama, R. Sekiguchi, and Y. Hayashi, 2014: Upgrade of JMA's Operational NWP Global Model. CAS/JSC WGNE Res. Activ. Atmos. Oceanic Modell., 44, 4.15–4.16. [Available at https://wgne.net/publications/wgne-blue-book/ (Accessed on 13 September 2023).]

Yonehara, H., T. Tokuhiro, R. Nagasawa, M. Ujiie, A. Shimokobe, M. Nakagawa, R. Sekiguchi, T. Kanehama, H. Sato, and K. Saito, 2017: Upgrade of parameterization schemes in JMA’s operational global NWP model. CAS/JSC WGNE Res. Activ. Atmos. Oceanic Modell., 47, 4.17–4.18. [Available at https://wgne.net/publications/wgne-blue-book/ (Accessed on 13 September 2023).]

Yonehara, H., R. Sekiguchi, T. Kanehama, K. Saitou, T. Kinami, A. Shimokobe, D. Hotta, R.Nagasawa, H. Sato, M. Ujiie, T. Kadowaki, S. Yabu, K. Yamada, M. Nakagawa, and T.

Tokuhiro, 2018: Upgrade of JMA’s operational global NWP system. CAS/JSC WGNE Res. Activ. Atmos. Oceanic Modell., 48, 6.15–6.16. [Available at https://wgne.net/publications/wgne-blue-book/ (Accessed on 13 September 2023).]

Yu, L., 2019: Global Air-Sea Fluxes of Heat, Fresh Water, and Momentum: Energy Budget Closure and Unanswered 5 Questions. Annu. Rev. Marine Sci., 11, 227–248.

Yukimoto, S., H. Kawai, T. Koshiro, N. Oshima, K. Yoshida, S. Urakawa, H. Tsujino, M. Deushi, T. Tanaka, M. Hosaka, S. Yabu, H. Yoshimura, E. Shindo, R. Mizuta, A. Obata, Y. Adachi, and M. Ishii, 2019: The Meteorological Research Institute Earth System Model Version 2.0, MRI-ESM2.0: Description and Basic Evaluation of the Physical Component. J. Meteor. Soc. Japan, 97, 931–965.

Zhong, W., and J. D. Haigh, 1995: Improved broadband emissivity parameterization for water vapor cooling rate calculations. J. Atmos. Sci., 52, 124–138.

Zou, C.-Z., and H. Qian, 2016: Stratospheric temperature climate data record from merged SSU and AMSU-A observations. J. Atmos. Oceanic Technol., 33, 1967–1984.

Zou, C.-Z., and W. Wang, 2011: Intersatellite calibration of AMSU-A observations for weather and climate applications. J. Geophys. Res., 116, D23113, doi:10.1029/2011JD016205 (Accessed on 26 September 2023).

List of Figures

recalculation was performed. Solid vertical lines represent the three disconnection points (see Section 6).

Fig. 8 RMS errors of two-day forecasts of the geopotential height at 500 hPa averaged over the extratropics in the (a) Northern and (b) Southern Hemisphere (from 90°N to 20°N and from 20°S to 90°S, respectively) from JRA-3Q, JRA-55, JRA-25, and the JMA operational system, verified against their own analyses. Each value represents the average over the previous 12 months.

Fig. 9 Same as Fig. 8, but for the wind vectors at (a) 250 hPa and (b) 850 hPa averaged over the tropics (from 20°N to 20°S).

Fig. 10 Global mean and RMS background departure (observation minus background) of radiosonde temperatures used in JRA-3Q, JRA-55, and JRA-25.

Fig. 11 Radial profiles of horizontal correlations of the background error covariances used in (a, b) JRA-3Q and (c, d) JRA-55 for (a, c) relative vorticity and (b, d) unbalanced temperature (the temperature component that is statistically independent of wind fields). The relative vorticity and unbalanced temperature, are included in the control variables of 4D-Var (JMA 2019).

Fig. 12 Spatial distributions of (a–c) reflected solar radiation, (d–f) outgoing thermal (longwave) radiation, and (g–i) net radiation at the TOA for JRA-3Q (a, d, g), their differences from CERES-EBAF (b, e, h), and the differences of JRA-55 from CRES-

EBAF (c, f, i) averaged over 2002–2008 in units of W m^{-2}.

Fig. 13 Time series of 12-month running mean of radiation anomalies in JRA-3Q (red), JRA-55 (purple), ERA-5 (blue) and CERES-EBAF (black), for (a) the TOA solar incoming radiation, (b) the TOA solar reflected radiation, (c) the TOA outgoing thermal radiation and for (d) the TOA net radiation flux. The anomalies are defined relative to their own monthly climatologies averaged over 2002–2008 in units of W m^{-2}.

Fig. 14 Spatial distributions of (a–c) radiative net heat fluxes, (d–f) sensible heat fluxes, and (g–i) latent heat fluxes at the surface for JRA-3Q (a, d, g), their differences from CERES-EBAF or OAFLUX (b, e, h), and differences of JRA-55 from CERES-EBAF or OAFLUX (c, f, i) averaged over 2002–2008 in units of W m^{-2}.

Fig. 15 Global TC detection rates in JRA-3Q and JRA-55.

Fig. 16 Global mean of the maximum 10-m wind speed around detected TC centers. The best track data used in the calculation are the same as the data used for the rate of detection.

Fig. 17 Twelve-month running mean surface temperature anomalies of JRA-3Q, JRA-55, ERA5, HadCRUT5 analysis, NOAAGlobalTemp, GISTEMP, and Berkeley Earth averaged over the globe. The global mean surface air temperatures for JRA-55 and JRA-3Q were calculated using analysis fields over land and background fields over the ocean. Anomalies for each dataset are defined relative to their own climatological means during 1991–2020.

Fig. 18 Twelve-month running mean temperature anomalies for the (a) lower stratosphere, (b) upper troposphere, (c) middle troposphere, and (d) lower troposphere averaged over the globe. Time series from RSS v4.0, UAH v6.0, and NOAA v4.1 represent measurements by the MSU channel 4, 3, and 2, and extrapolated values from the MSU measurements to the lower troposphere, whereas those from JRA-3Q, JRA-55, and HadAT2 are MSU equivalent brightness temperatures. Anomalies for each dataset are defined relative to their own climatological means during 1995–2005.

Fig. 19 Twelve-month running mean temperature anomalies for the (a) top, (b) upper, and (c) middle stratosphere averaged over the globe. Time series from NOAA v3.0 and NCAR represent measurements by the SSU channel 3, 2, and 1, whereas those from JRA-3Q and JRA-55 are SSU equivalent brightness temperatures. Anomalies for each dataset are defined relative to their own climatological means during 1995–2005.

Fig. 20 Zonal-mean differences of specific humidity between JRA-3Q and three other reanalysis products, averaged over 1981–2015.

Fig. 21 Vertical profiles of equatorial mean (5S–5N) specific humidity bias of JRA-3Q and JRA-55 against GNSS−RO averaged over 2007–2018.

Fig. 22 Twelve-month running means of specific humidity for 11 reanalysis products averaged over the equatorial region (5S–5N) at pressure levels of (a) 600 hPa and (b)

925 hPa.

Fig. 23 Time-height cross sections of tropospheric specific humidity increments averaged over the equatorial region (5S–5N) in (a) JRA-3Q and (b) JRA-55.

Fig. 24 Time-height cross sections of stratospheric specific humidity averaged over the equatorial region (5S–5N) in (a) JRA-3Q and (b) JRA-55.

Fig. 25 Time series of 12-month running means of (a) tropical (22S-22N) precipitation for 11 reanalysis products and 2 observational datasets, and (b) spatial anomaly correlations against GPCP. Anomalies for each dataset are defined relative to their own climatological monthly means during 1991–2010 (except for the 1991–2002 mean for ERA-40 and the 1997–2010 mean for TRMM).

Fig. 26 Decadal mean precipitation bias against GPCP. (a)–(d) and (e)–(h) denote the precipitation bias in JRA-3Q and JRA-55, respectively.

Fig. 27 Zonally averaged decadal mean precipitation bias of (a) JRA-3Q and (b) JRA-55 against GPCP, and (c) bias differences between the 2000s and 1990s.

Fig. 28 Coverages of surface pressure (a, b, c) and upper-level observations (d, e, f) used in JRA-3Q, for (a, d) 1947-09-14 06UTC, (b, e) 1959-09-14 12UTC, and (c, f) 2020-09-14 12UTC are shown. The number at the lower left corner in each panel indicates the number of stations used in JRA-3Q.

Fig. 29 Time series of monthly global mean and RMS of background departure for surface pressure from land stations.

Fig. 30 Names of geographical locations around Japan.

Fig. 31 Analysis field of mean sea level pressure (hPa) from (a) JRA-3Q, (b) 20CRv3, and (c) CERA-20C at 06 UTC on 14 September, 1947 and (d) the weather map analyzed at that time (the JMA weather chart).

Fig. 32 Time series of three-hour accumulated precipitation at Tokyo (35°42'N, 139°45'E), Hamamatsu (34°45'N, 137°43'E), Maebashi (36°24'N, 139°04 E), and Sendai (38°16'N, 140°54'E) from 00 UTC on 13 September 1947 to 00UTC on 17 September 1947.

Fig. 33 Same as Fig. 31, but at 00 UTC on 26 September, 1954.

Fig. 34 Time series of 10 m wind speed (m/s) at Kumamoto (32°49’N, 130°42’E), Hiroshima (34°24’N, 132°28’E), Tsuruga (35°39’N, 136°04’E), and Hakodate (41°49’N, 140°45’E) from 00 UTC on 24 September 1954 to 06UTC on 27 September 1954.

Fig. 35 Annual mean horizontal SST gradients (shaded, in units of °C (100km)$^{-1}$) and SSTs (contoured every 2°C) from (a, g) JRA-3Q, (b, h) JRA-3Q-COBE, and (c, i) JRA-3Q minus JRA-3Q-COBE, and annual mean total precipitation (shaded, in units of mm day^{-1}) and SSTs (contoured every 2°C) from (d, j) JRA-3Q, (e, k) JRA-3Q-COBE, and (f, l) JRA-3Q minus JRA-3Q-COBE over the (a–f) western North Pacific and (g–l) western North Atlantic domains, averaged over 1986–1990.

Fig. 36 Annual mean latent heat fluxes (shaded, in units of W m^{-2}) and SSTs (contoured every 2°C) from (a) JRA-3Q, (b) JRA-3Q-COBE, and (c) JRA-3Q minus JRA-3Q-COBE over northern North America, averaged over 1986–1990.

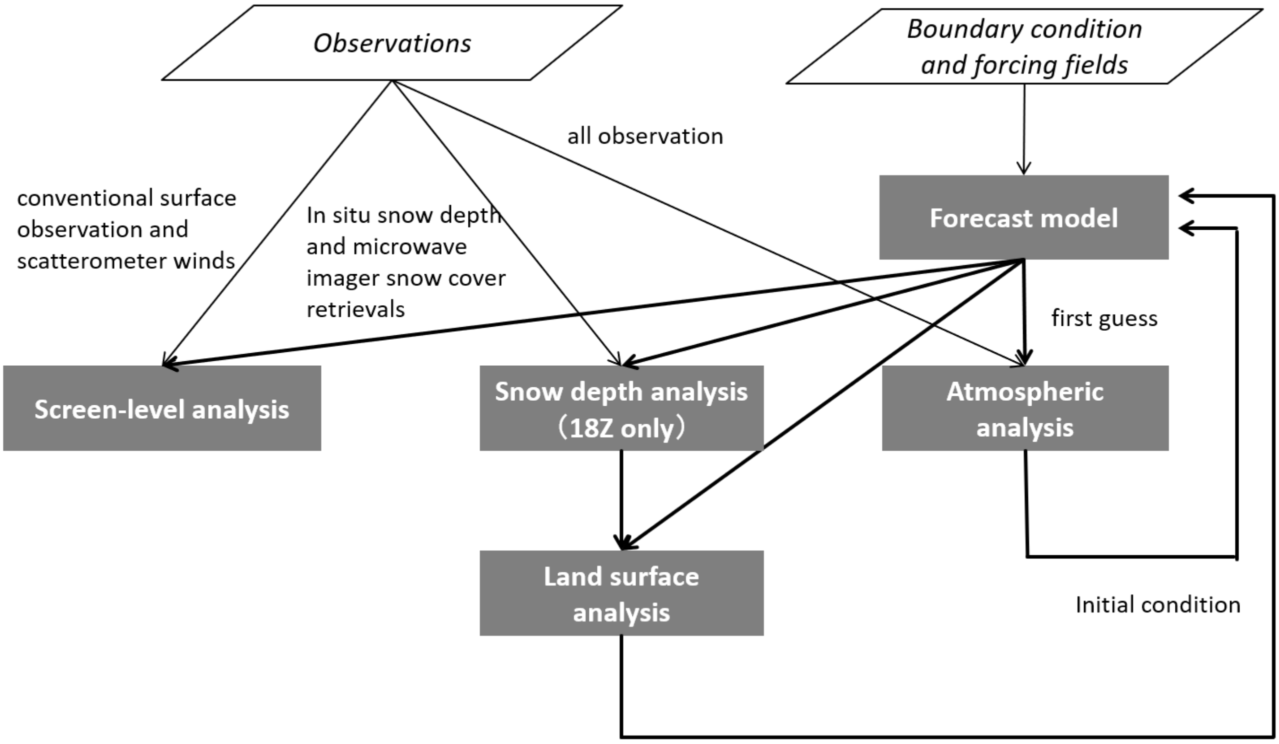

Fig. 1 Schematic diagram of the main components of the JRA-3Q data assimilation system and the data flow among them. The atmospheric, screen-level, and land surface analyses are performed every 6 hours, and the snow depth analysis is performed daily. The forecast model is used to produce the first guess needed for the analysis.

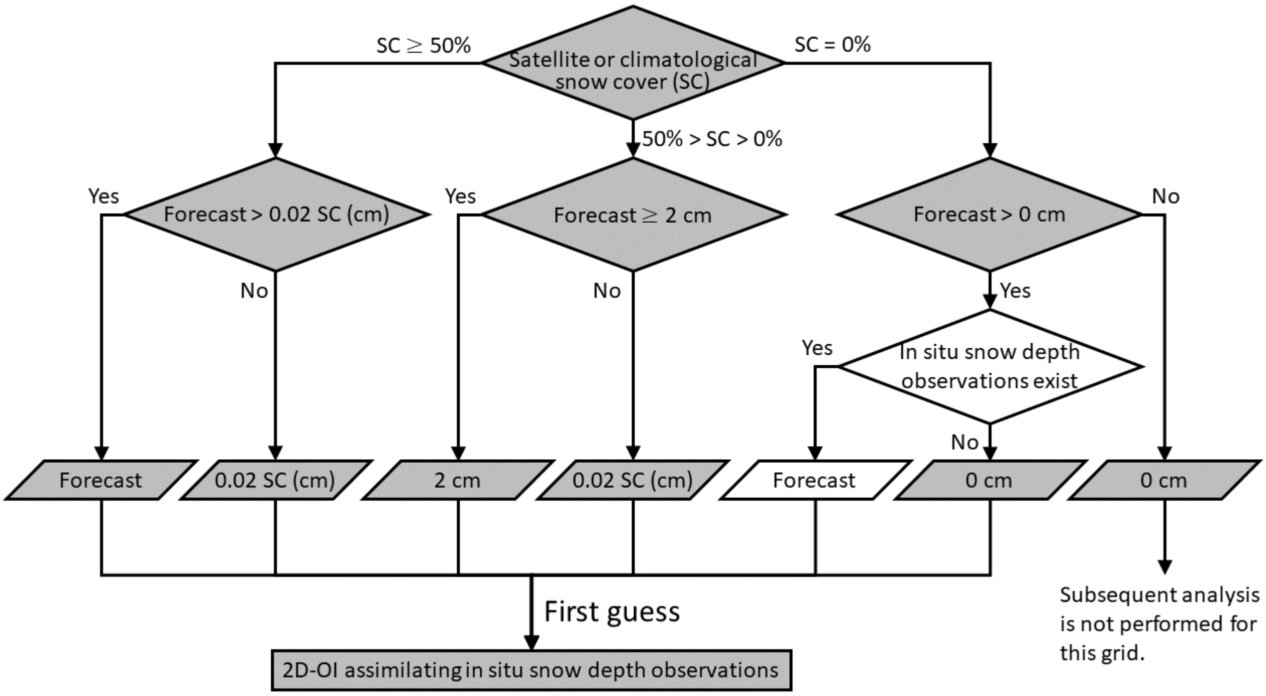

Fig. 2 Flow chart of producing first guesses of snow depth. Processes shown in plain boxes were added after JRA-55, whereas those in shaded boxes are the same as the ones used in JRA-55.

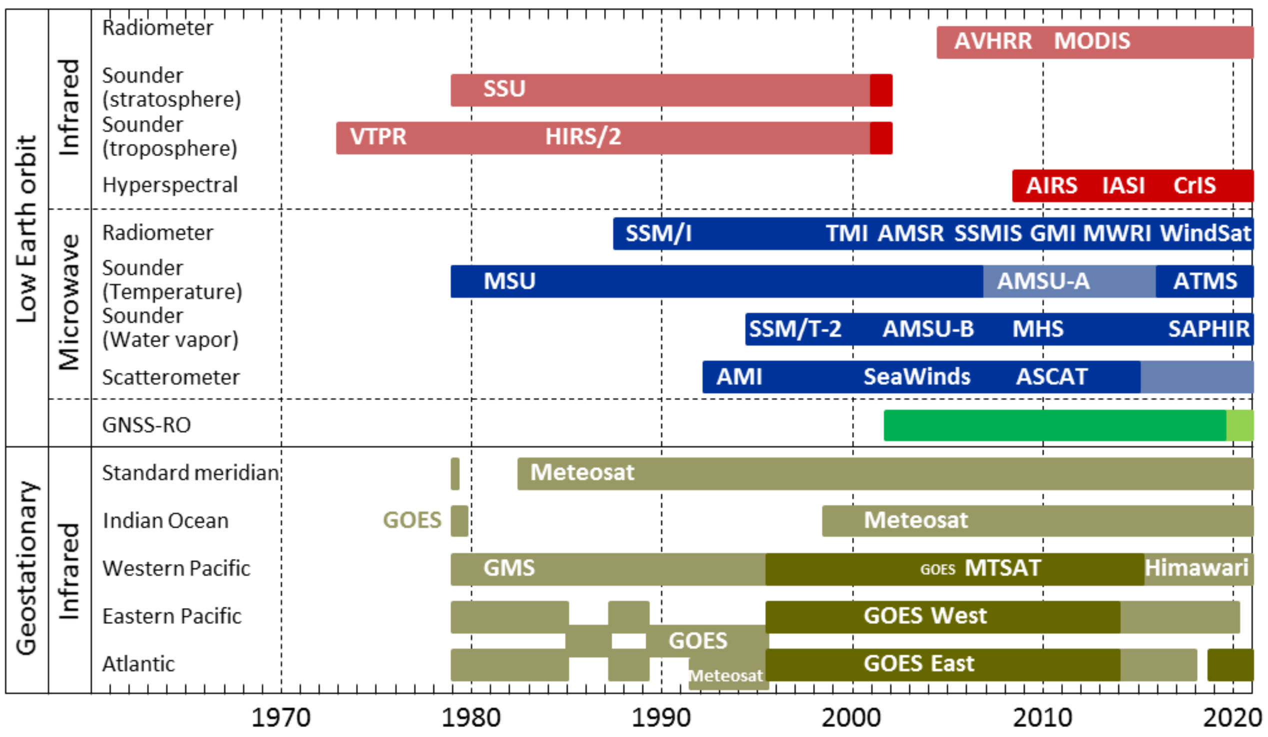

Fig. 3 Satellite observations used in JRA-3Q. Darker shading indicates observations added, recalibrated, or reprocessed after JRA-55.

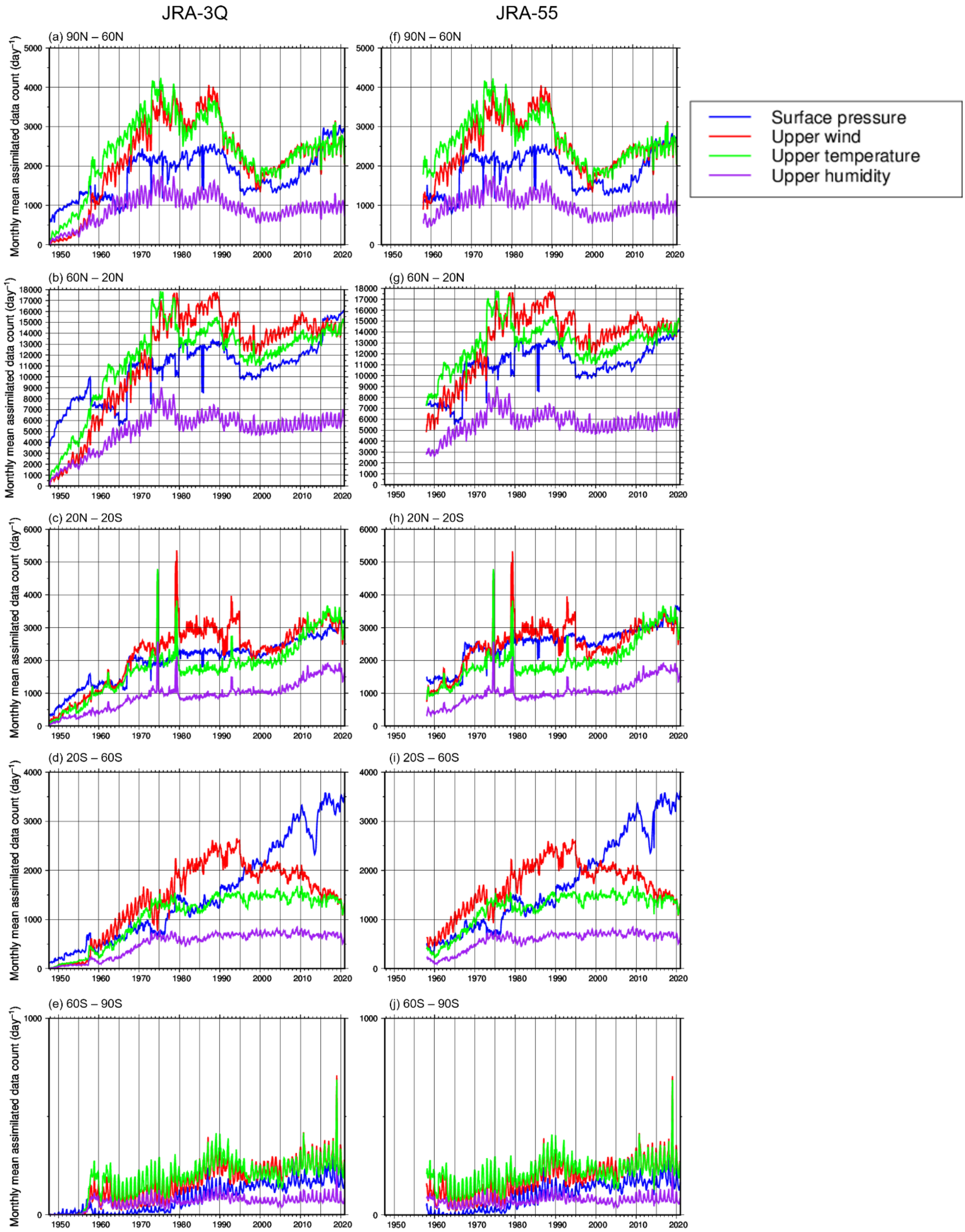

Fig. 4 Monthly mean counts of conventional surface pressures and upper-air observations assimilated in the atmospheric analysis component of (a–e) JRA-3Q and (f–j) JRA-55 in five latitude bands.

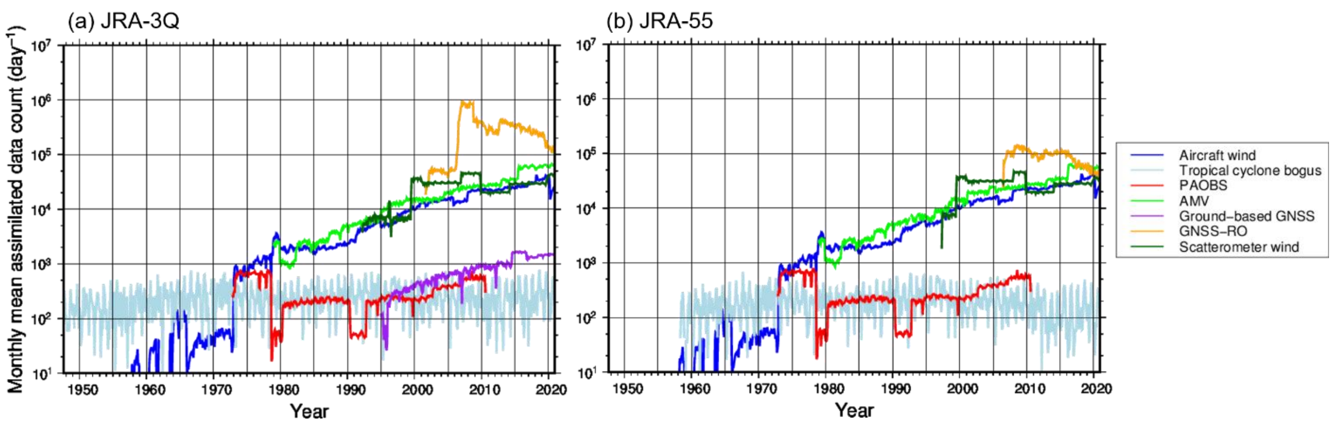

Fig. 5 Global monthly mean counts of aircraft winds, tropical cyclone boguses, PAOBS, AMV, ground-based GNSS zenith total delays, GNSS-RO bending angles, and scatterometer winds assimilated in the atmospheric analysis component of (a) JRA-3Q and (b) JRA-55.

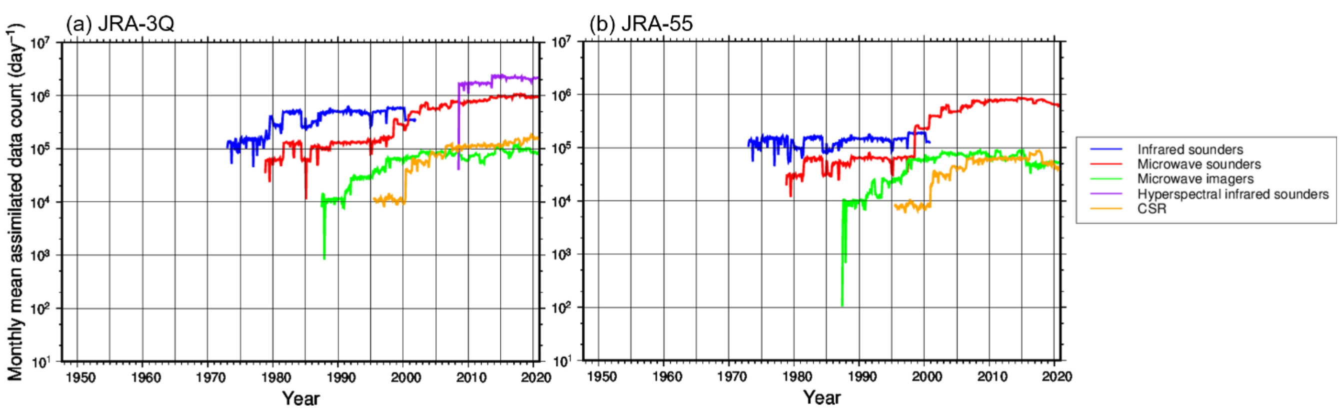

Fig. 6 Global monthly mean counts of various types of satellite radiances assimilated in the atmospheric analysis component of (a) JRA-3Q and (b) JRA-55.

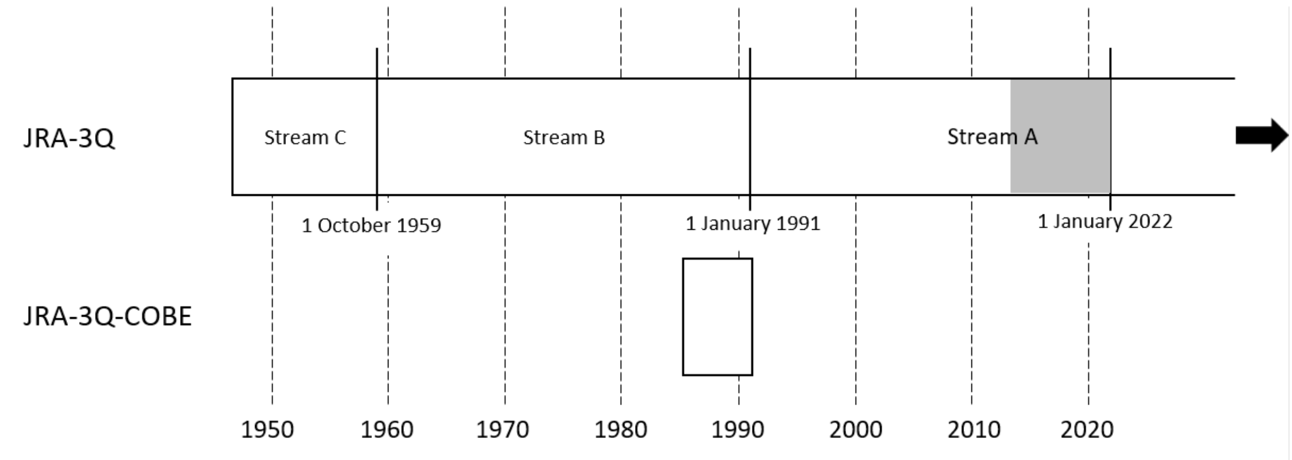

Fig. 7 Streams of JRA-3Q production. The shading indicates the period during which the recalculation was performed. Solid vertical lines represent the three disconnection points (see Section 6).

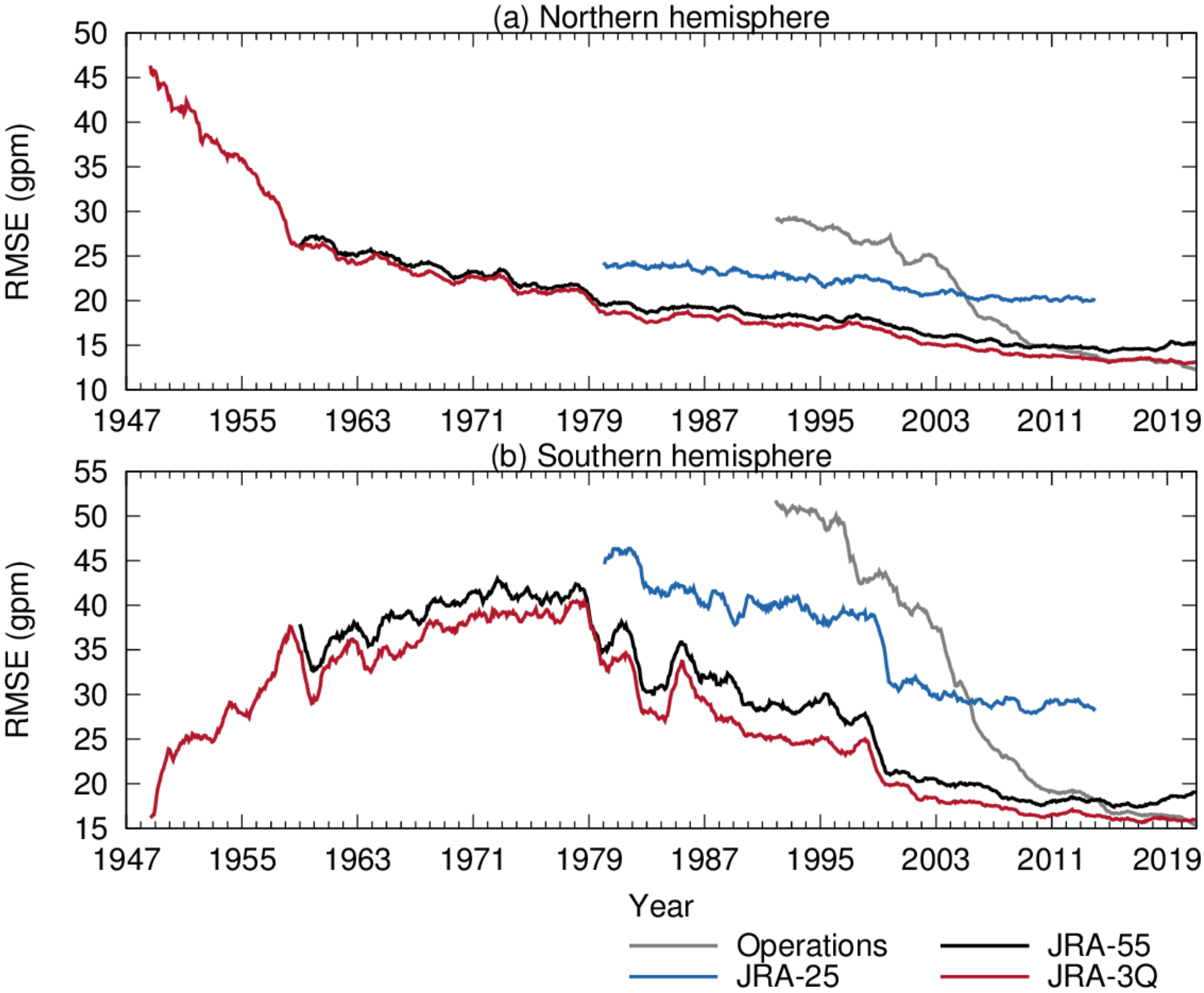

Fig. 8 RMS errors of two-day forecasts of the geopotential height at 500 hPa averaged over the extratropics in the (a) northern and (b) southern hemisphere (from 90°N to 20°N and from 20°S to 90°S, respectively) from JRA-3Q, JRA-55, JRA-25, and the JMA operational system, verified against their own analyses. Each value represents the average over the previous 12 months.

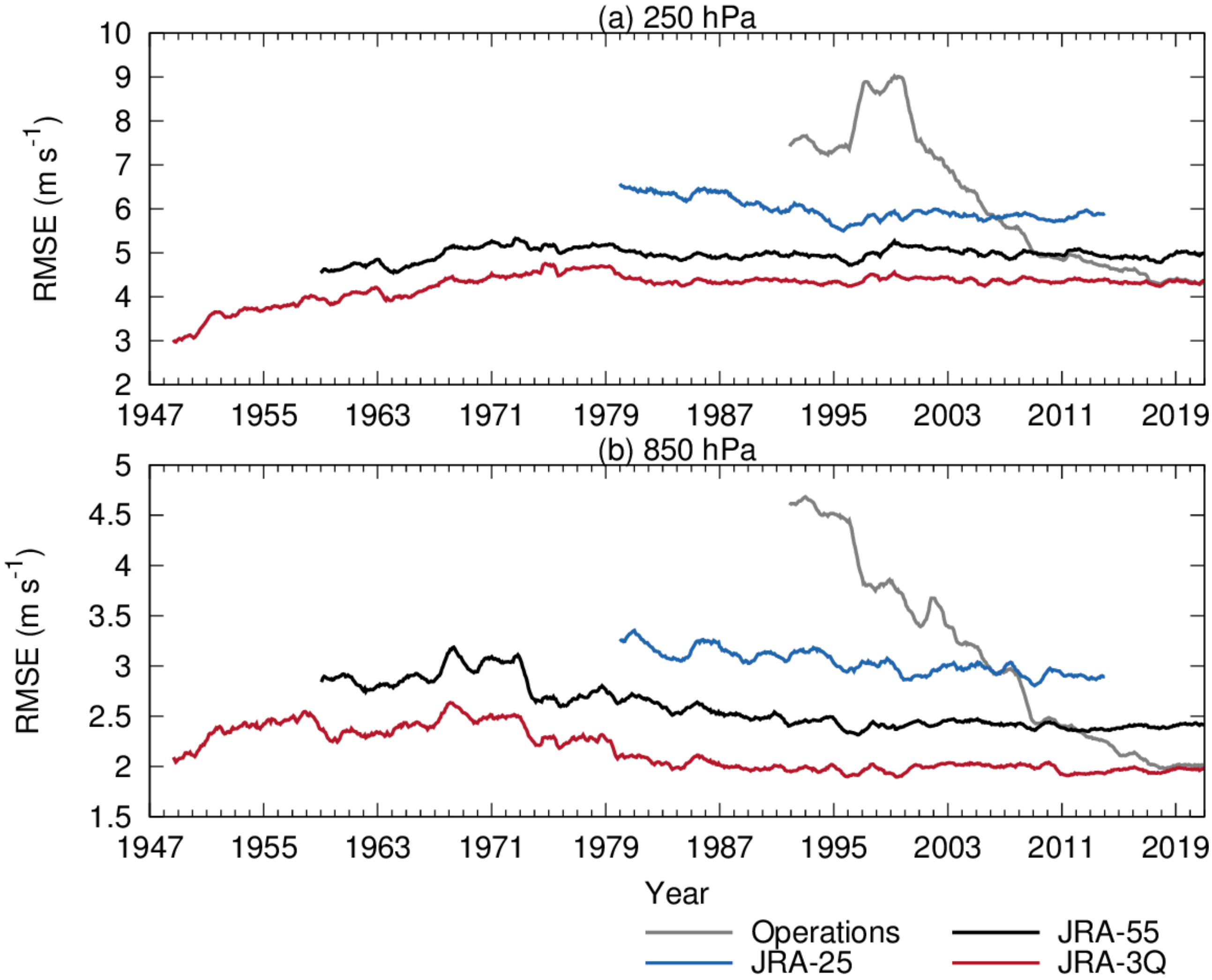

Fig. 9 Same as Fig. 8, but for the wind vectors at (a) 250 hPa and (b) 850 hPa averaged over the tropics (from 20°N to 20°S).

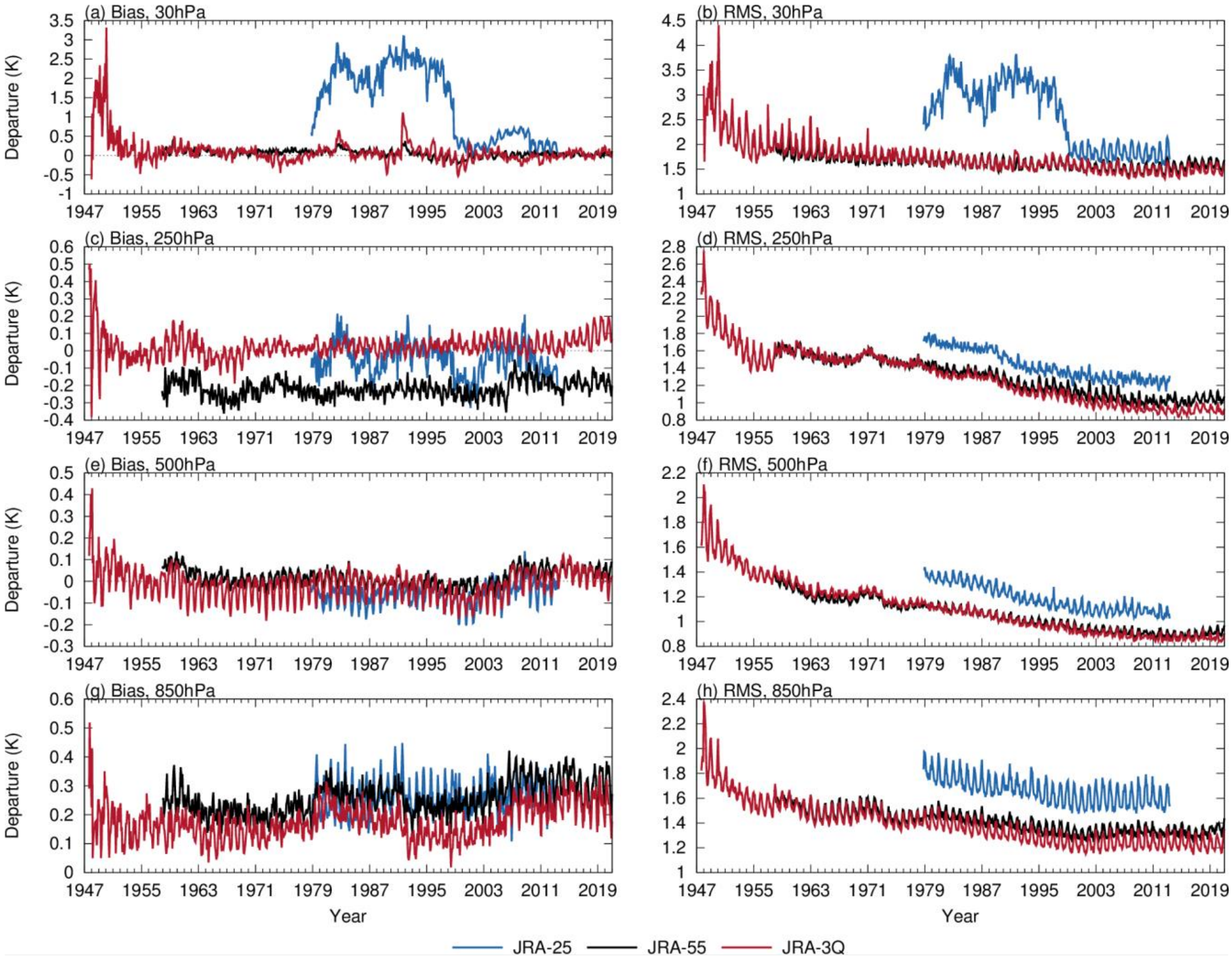

Fig. 10 Global mean and RMS background departure (observation minus background) of radiosonde temperatures used in JRA-3Q, JRA-55, and JRA-25.

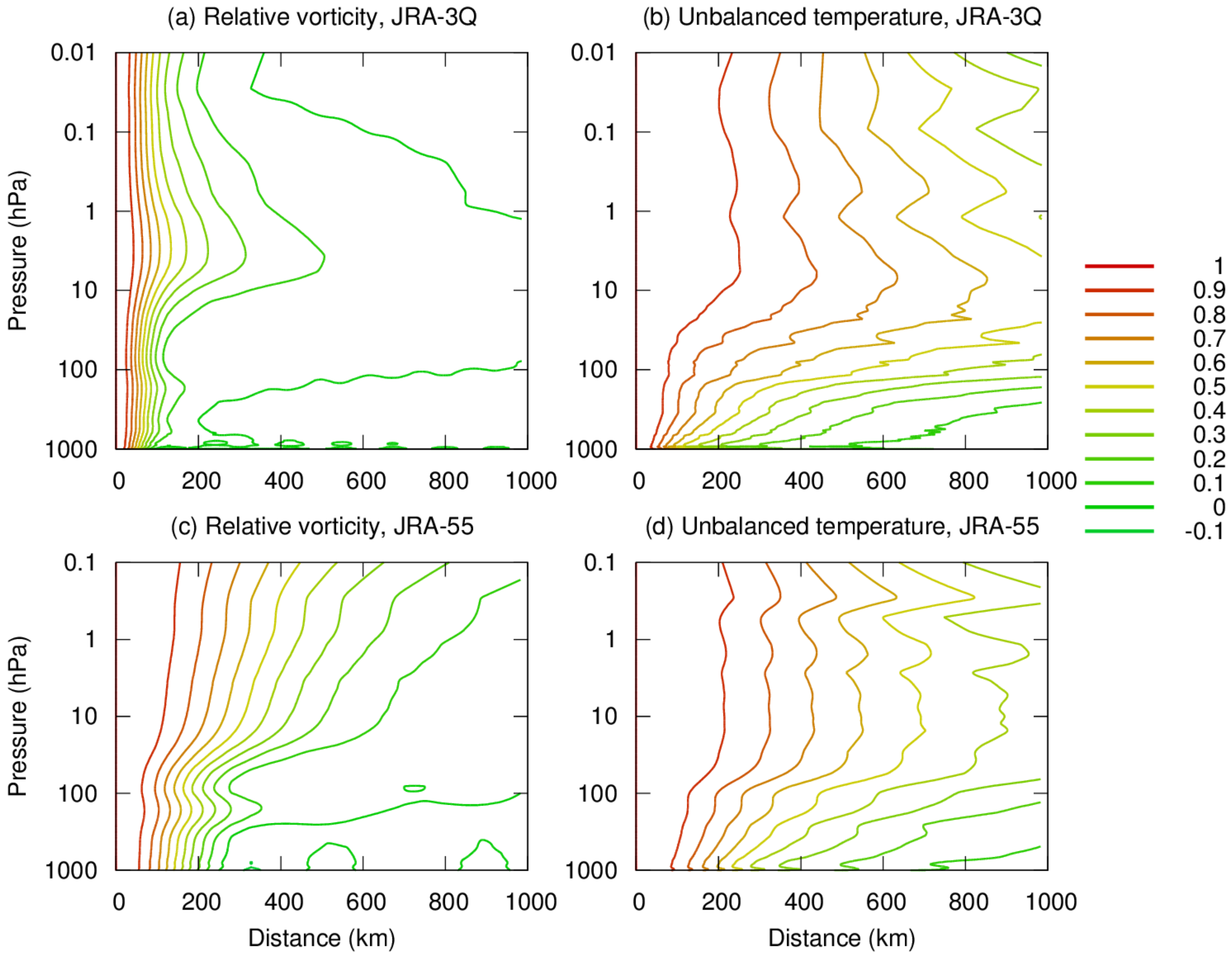

Fig. 11 Radial profiles of horizontal correlations of the background error covariances used in (a, b) JRA-3Q and (c, d) JRA-55 for (a, c) relative vorticity and (b, d) unbalanced temperature (the temperature component that is statistically independent of wind fields). The relative vorticity and unbalanced temperature are included in the control variables of 4D-Var (JMA 2019).

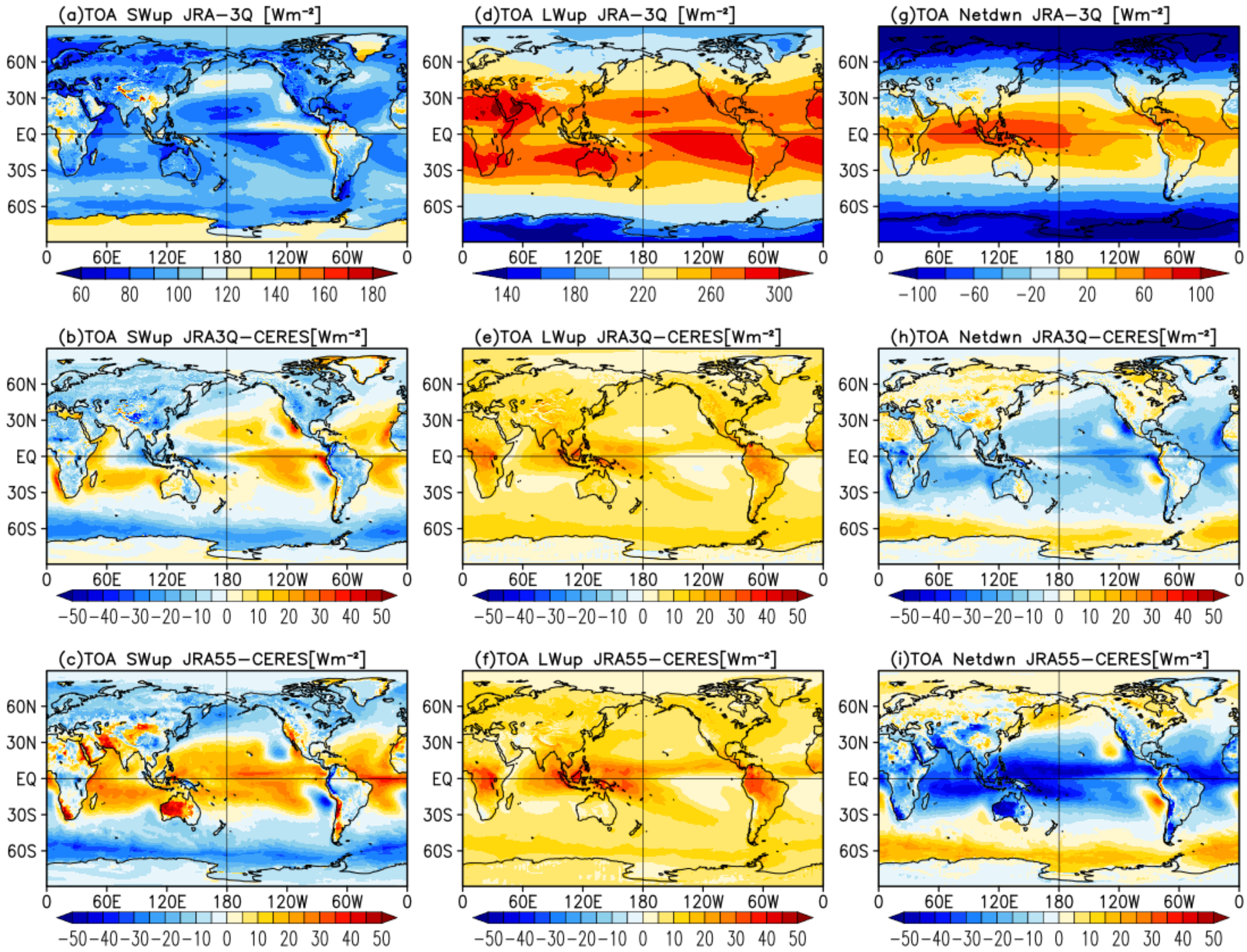

Fig. 12 Spatial distributions of (a–c) reflected solar radiation, (d–f) outgoing thermal (longwave) radiation, and (g–i) net radiation at the TOA for JRA-3Q (a, d, g), their differences from CERES-EBAF (b, e, h), and the differences of JRA-55 from CRES-EBAF (c, f, i) averaged over 2002–2008 in units of W m^{-2}.

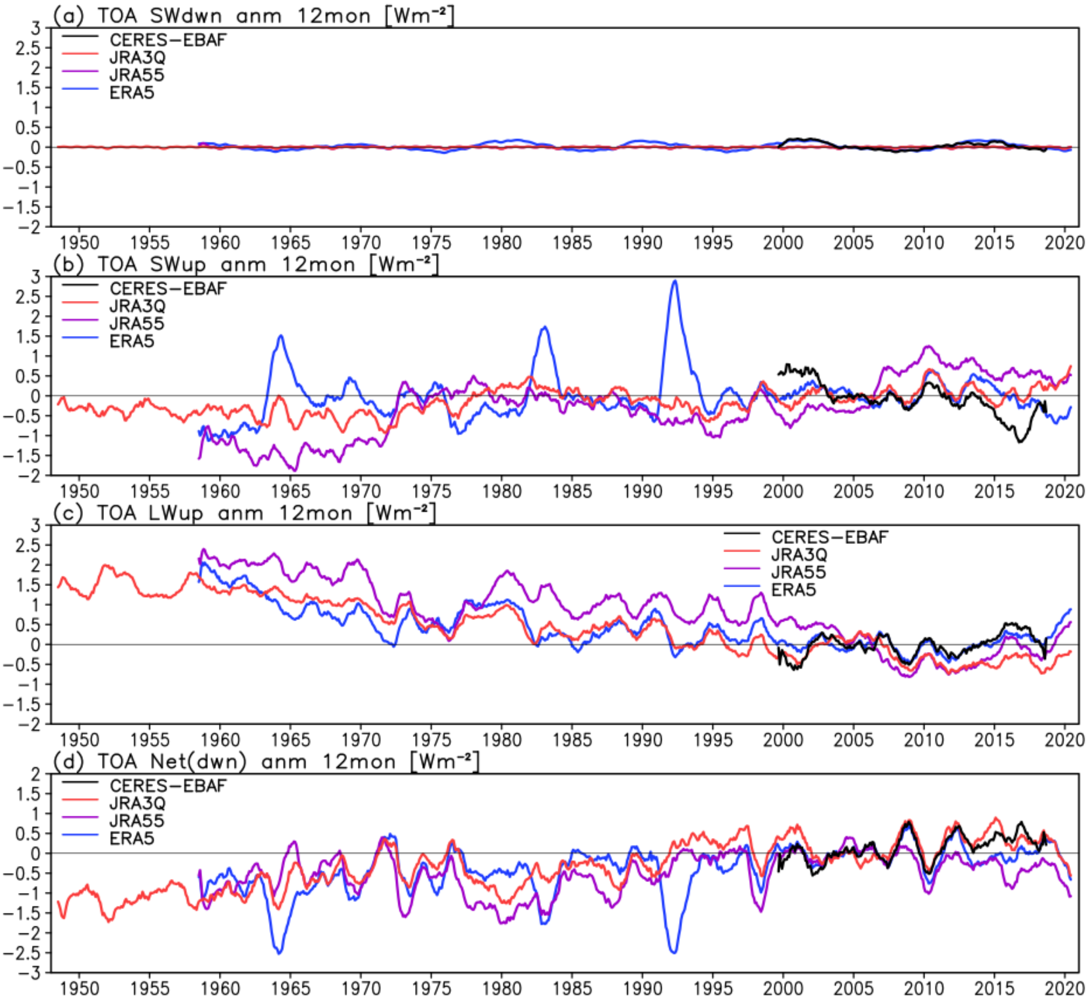

Fig. 13 Time series of 12-month running mean of radiation anomalies in JRA-3Q (red), JRA-55 (purple), ERA-5 (blue) and CERES-EBAF (black), for (a) the TOA solar incoming radiation, (b) the TOA solar reflected radiation, (c) the TOA outgoing thermal radiation and for (d) the TOA net radiation flux. The anomalies are defined relative to their own monthly climatologies averaged over 2002–2008 in units of W m^{-2}.

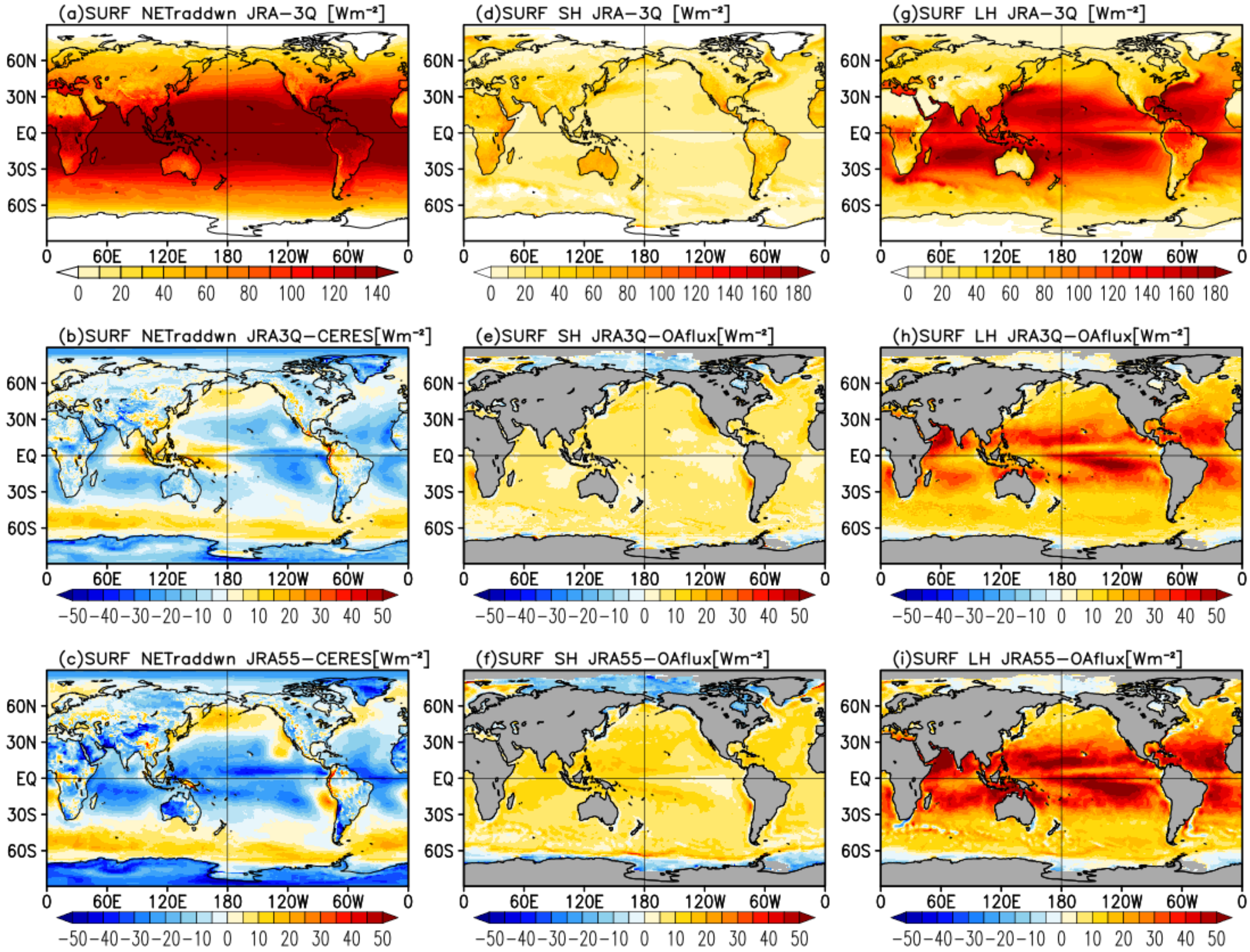

Fig. 14 Spatial distributions of (a–c) radiative net heat fluxes, (d–f) sensible heat fluxes, and (g–i) latent heat fluxes at the surface for JRA-3Q (a, d, g), their differences from CERES-EBAF or OAFLUX (b, e, h), and differences of JRA-55 from CERES-EBAF or OAFLUX (c, f, i) averaged over 2002–2008 in units of W m^{-2}.

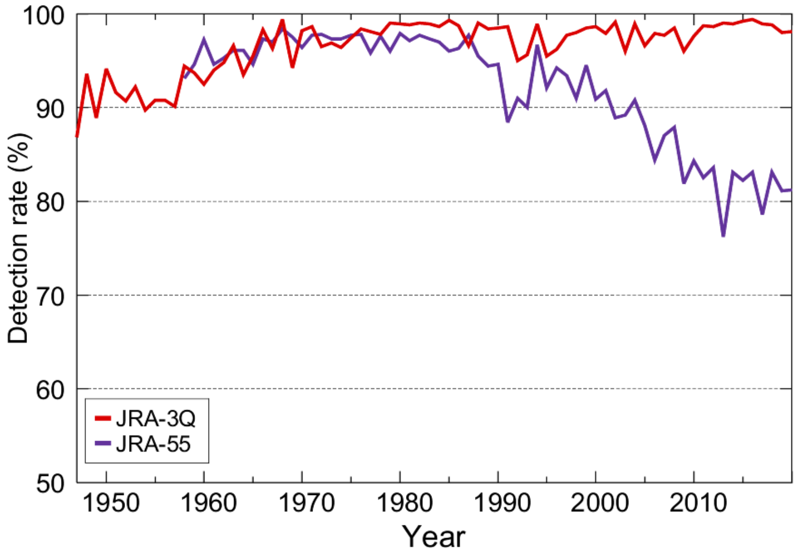

Fig. 15 Global TC detection rates in JRA-3Q and JRA-55.

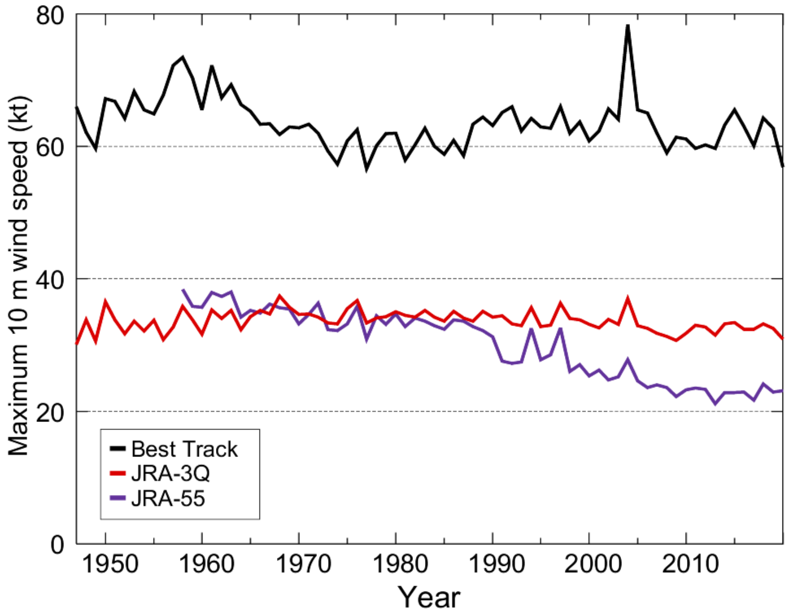

Fig. 16 Global mean of the maximum 10-m wind speed around detected TC centers. The best track data used in the calculation are the same as the data used for the rate of detection.

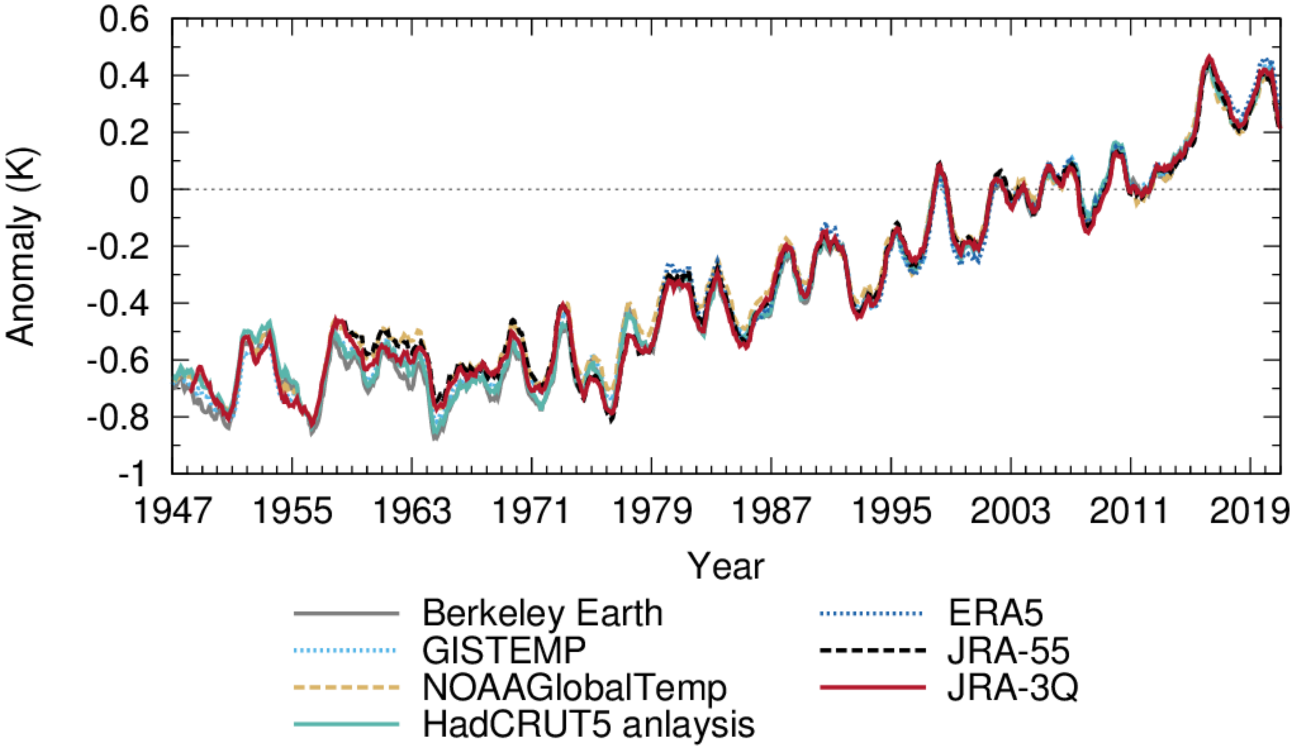

Fig. 17 Twelve-month running mean surface temperature anomalies of JRA-3Q, JRA-55, ERA5, HadCRUT5 analysis, NOAAGlobalTemp, GISTEMP, and Berkeley Earth averaged over the globe. The global mean surface air temperatures for JRA-55 and JRA-3Q were calculated using analysis fields over land and background fields over the ocean. Anomalies for each dataset are defined relative to their own climatological means during 1991–2020.

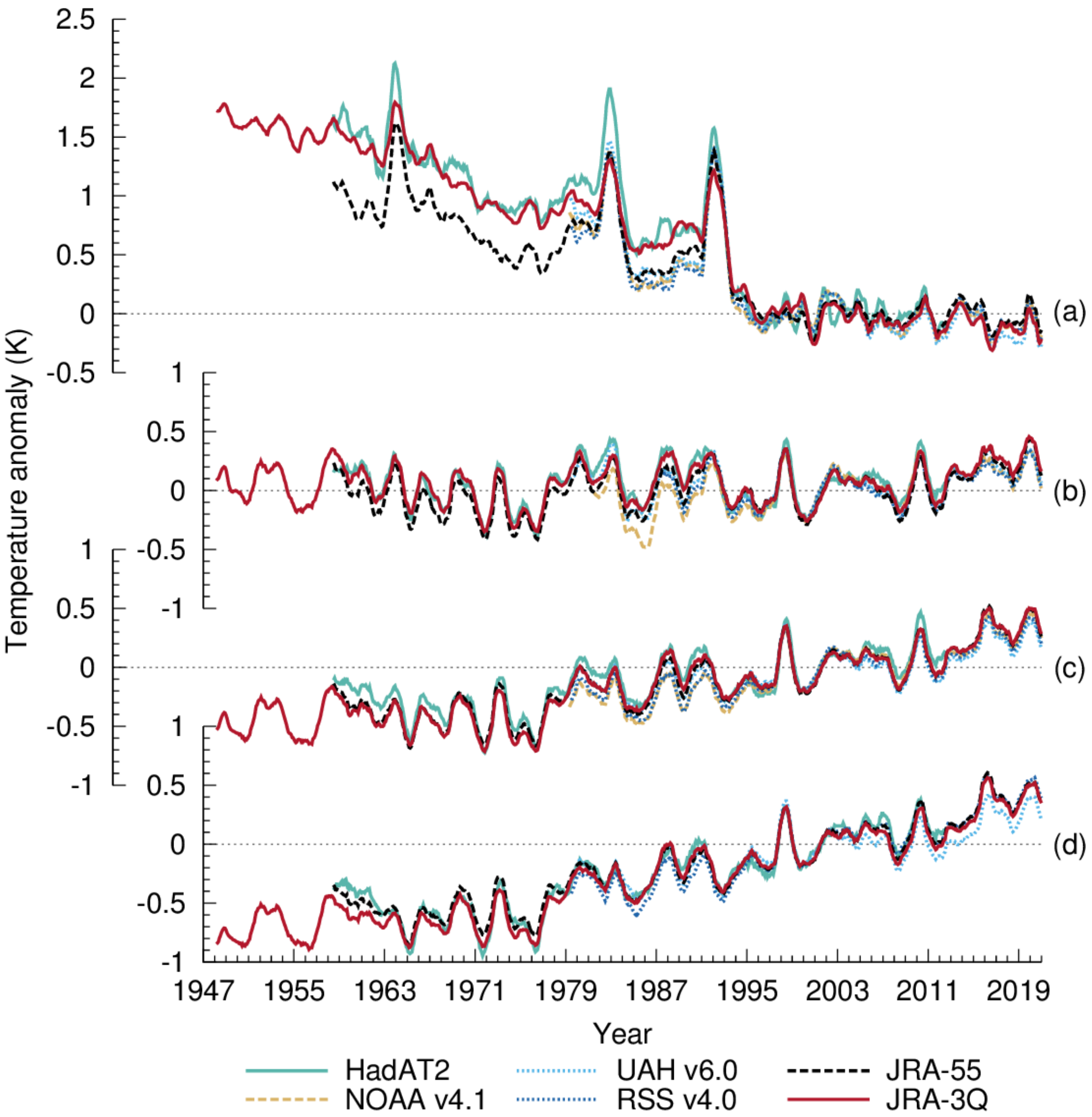

Fig. 18 Twelve-month running mean temperature anomalies for the (a) lower stratosphere, (b) upper troposphere, (c) middle troposphere, and (d) lower troposphere averaged over the globe. Time series from RSS v4.0, UAH v6.0, and NOAA v4.1 represent measurements by the MSU channel 4, 3, and 2, and extrapolated values from the MSU measurements to the lower troposphere, whereas those from JRA-3Q, JRA-55, and HadAT2 are MSU equivalent brightness temperatures. Anomalies for each dataset are defined relative to their own climatological means during 1995–2005.

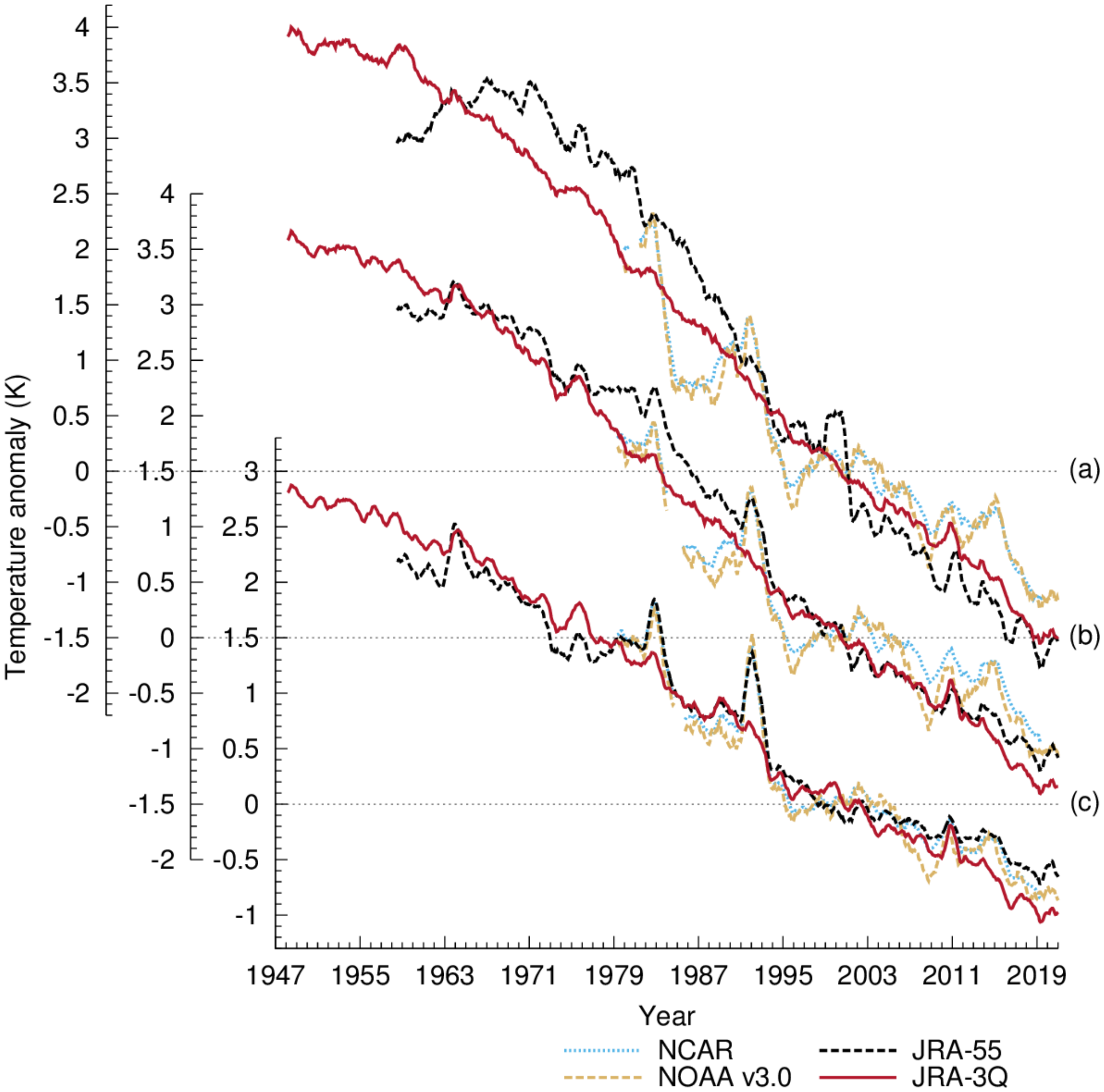

Fig. 19 Twelve-month running mean temperature anomalies for the (a) top, (b) upper, and (c) middle stratosphere averaged over the globe. Time series from NOAA v3.0 and NCAR represent measurements by the SSU channel 3, 2, and 1, whereas those from JRA-3Q and JRA-55 are SSU equivalent brightness temperatures. Anomalies for each dataset are defined relative to their own climatological means during 1995–2005.

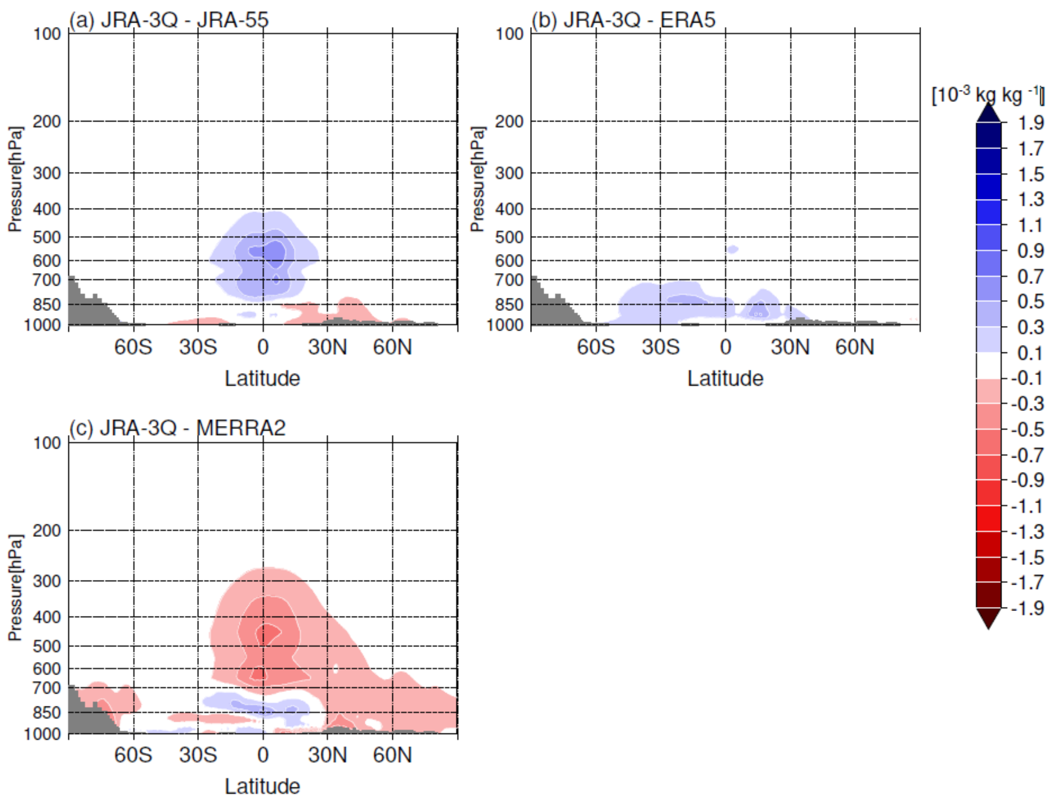

Fig. 20 Zonal-mean differences of specific humidity between JRA-3Q and three other reanalysis products, averaged over 1981–2015.

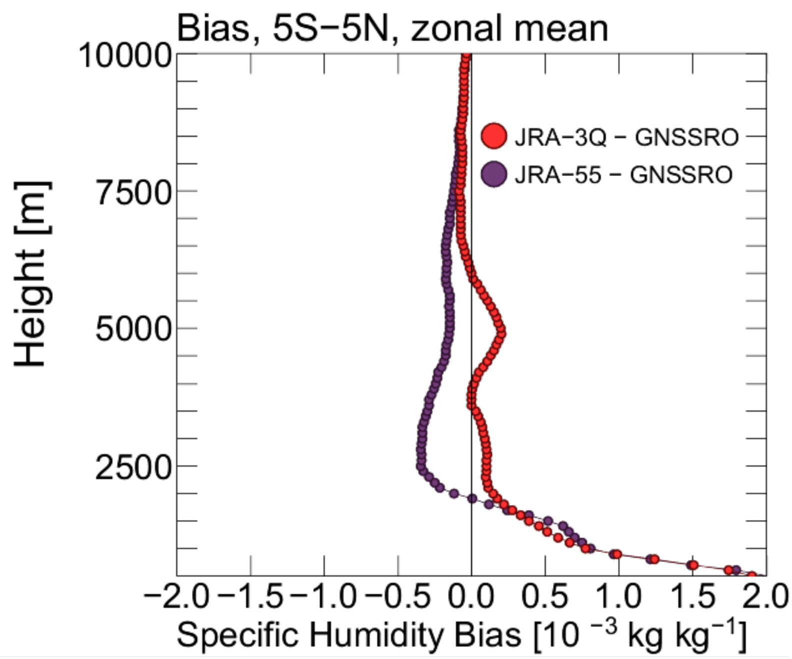

Fig. 21 Vertical profiles of equatorial mean (5S–5N) specific humidity bias of JRA-3Q and JRA-55 against GNSS−RO averaged over 2007–2018.

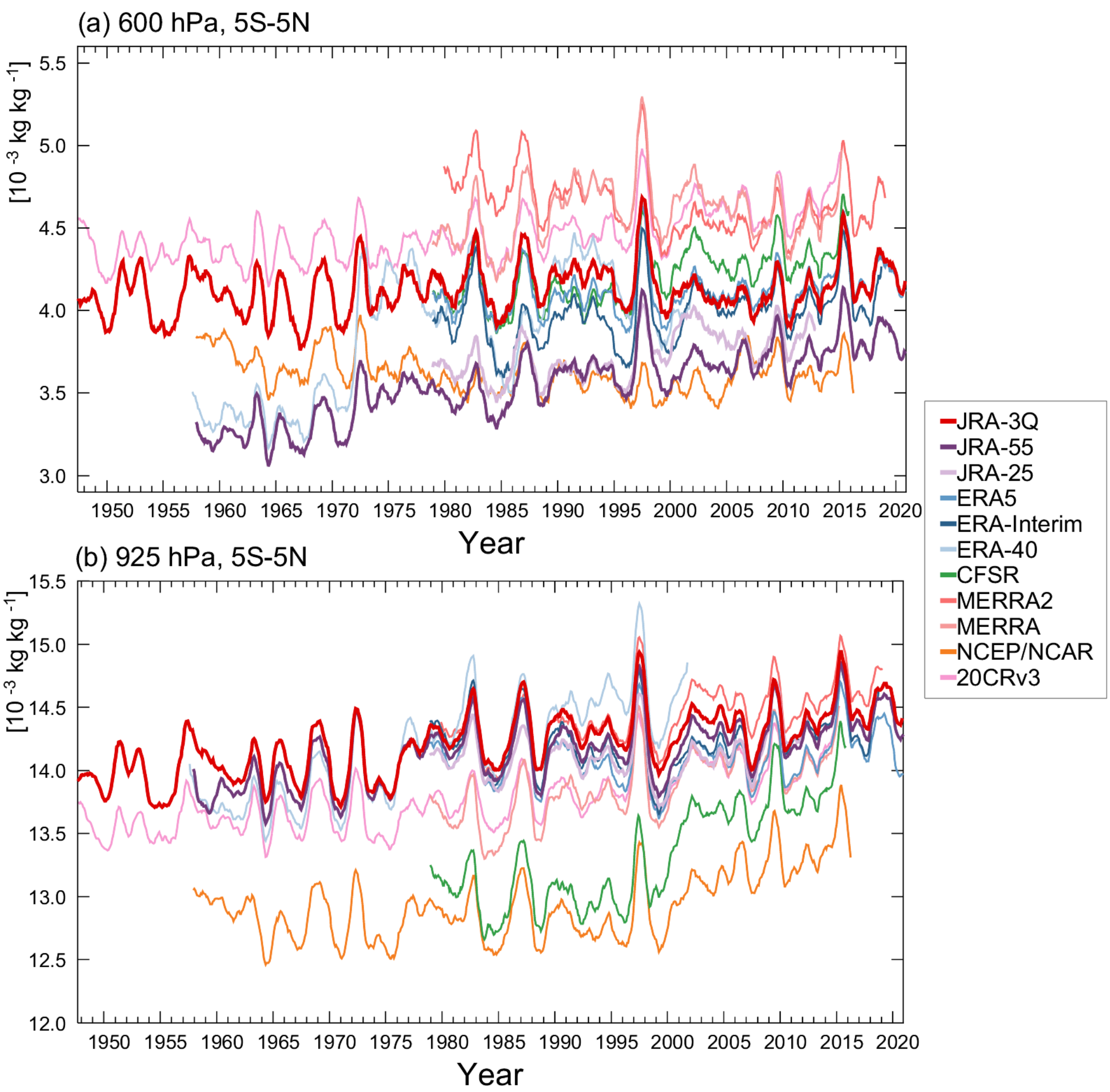

Fig. 22 Twelve-month running means of specific humidity for 11 reanalysis products averaged over the equatorial region (5S–5N) at pressure levels of (a) 600 hPa and (b) 925 hPa.

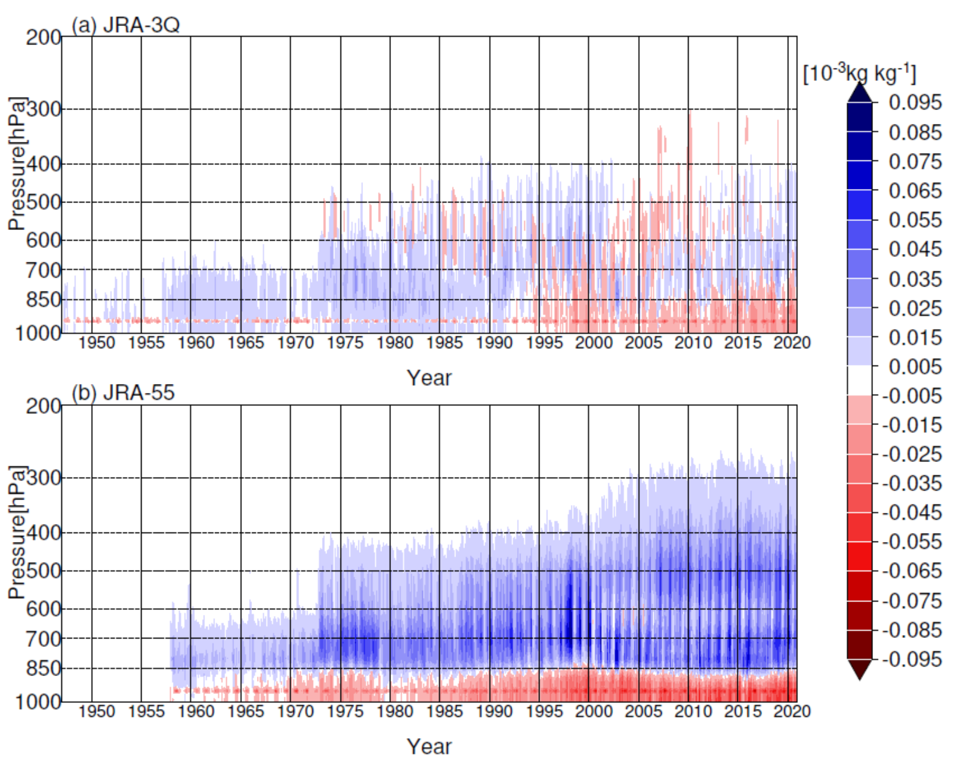

Fig. 23 Time-height cross sections of tropospheric specific humidity increments averaged over the equatorial region (5S–5N) in (a) JRA-3Q and (b) JRA-55.

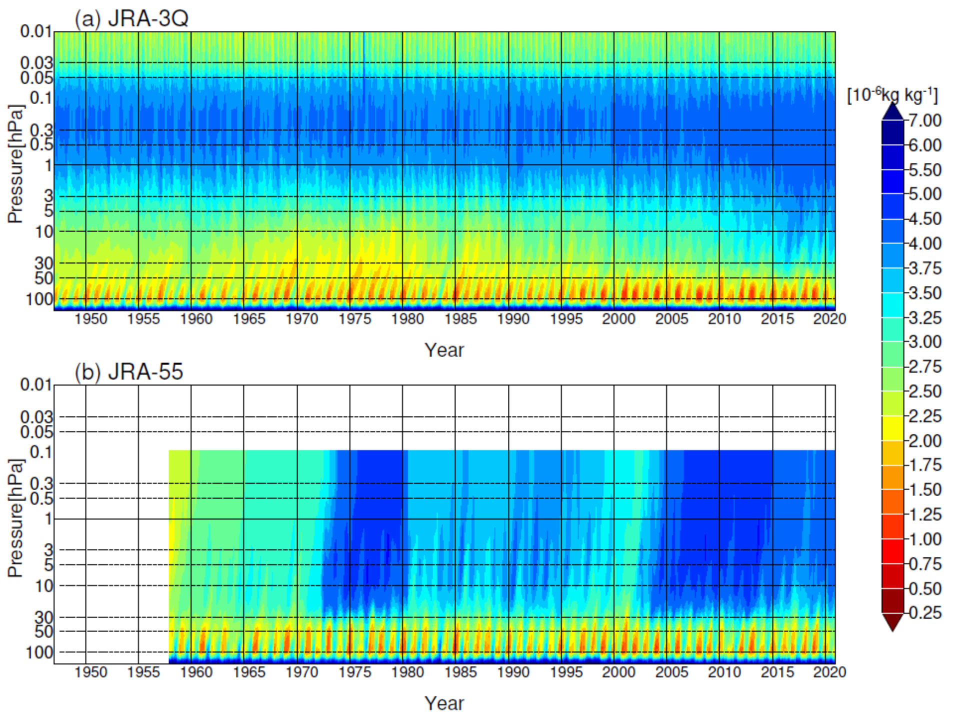

Fig. 24 Time-height cross sections of stratospheric specific humidity averaged over the equatorial region (5S–5N) in (a) JRA-3Q and (b) JRA-55.

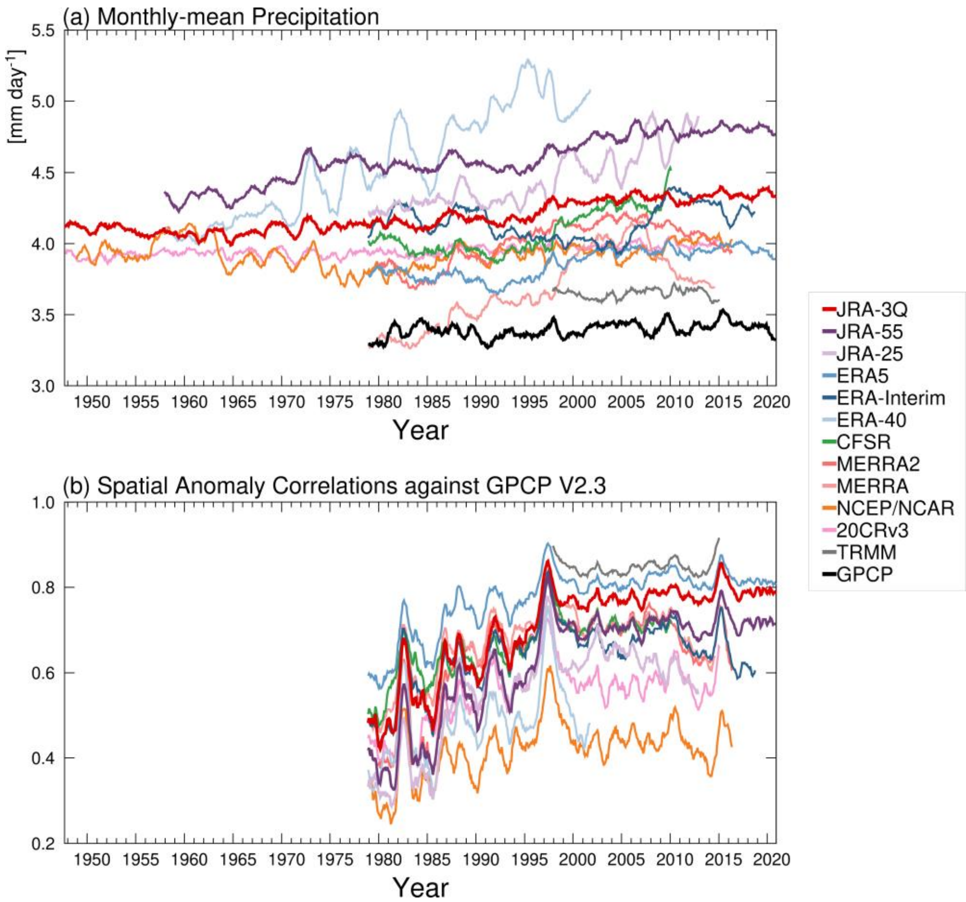

Fig. 25 Time series of 12-month running means of (a) tropical (22S-22N) precipitation for 11 reanalysis products and 2 observational datasets, and (b) spatial anomaly correlations against GPCP. Anomalies for each dataset are defined relative to their own climatological monthly means during 1991–2010 (except for the 1991–2002 mean for ERA-40 and the 1997–2010 mean for TRMM).

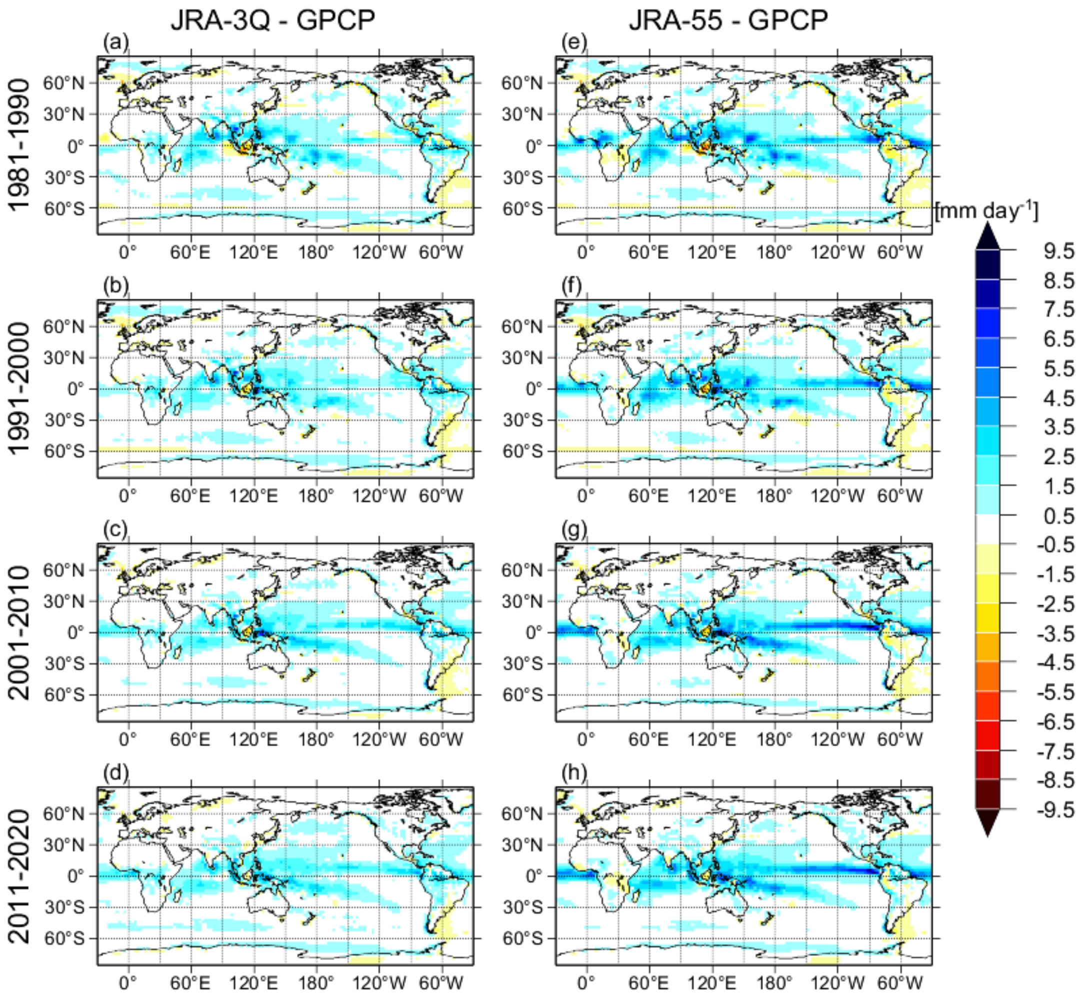

Fig. 26 Decadal mean precipitation bias against GPCP. (a)–(d) and (e)–(h) denote the precipitation bias in JRA-3Q and JRA-55, respectively.

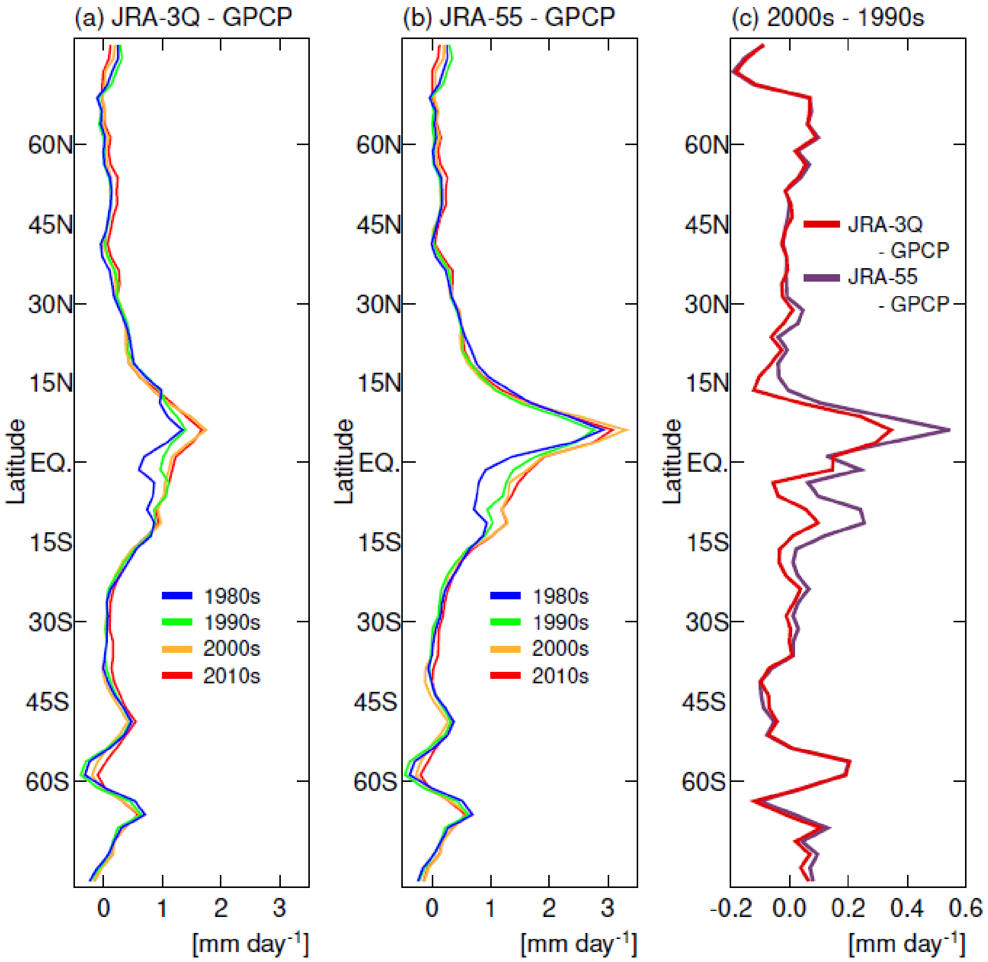

Fig. 27 Zonally averaged decadal mean precipitation bias of (a) JRA-3Q and (b) JRA-55 against GPCP, and (c) bias differences between the 2000s and 1990s.

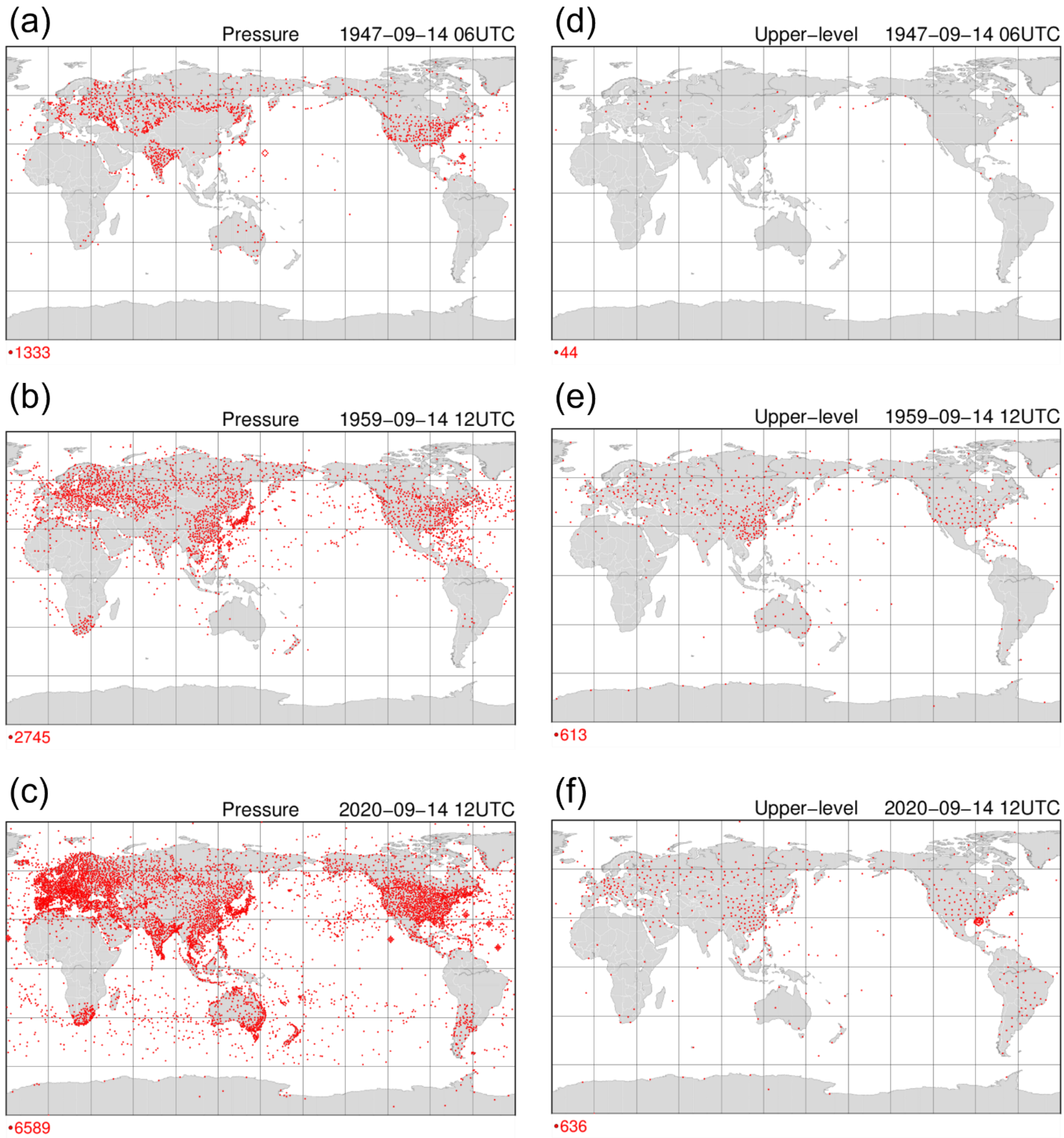

Fig. 28 Coverages of surface pressure (a, b, c) and upper-level observations (d, e, f) used in JRA-3Q, for (a, d) 1947-09-14 06UTC, (b, e) 1959-09-14 12UTC, and (c, f) 2020-09-14 12UTC are shown. The number at the lower left corner in each panel indicates the number of stations used in JRA-3Q.

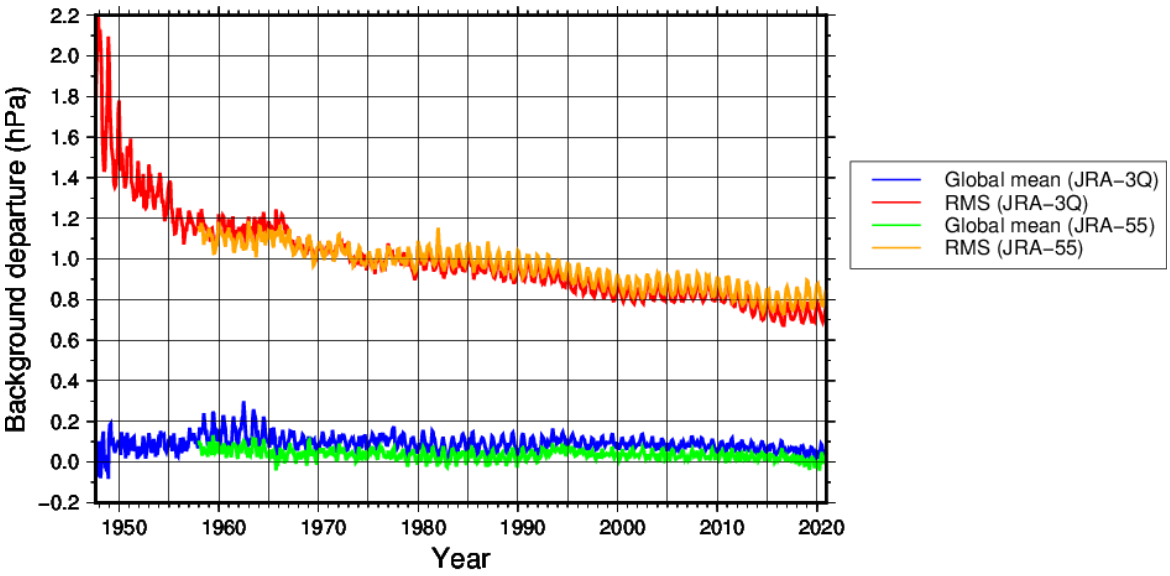

Fig. 29 Time series of monthly global mean and RMS of background departure for surface pressure from land stations.

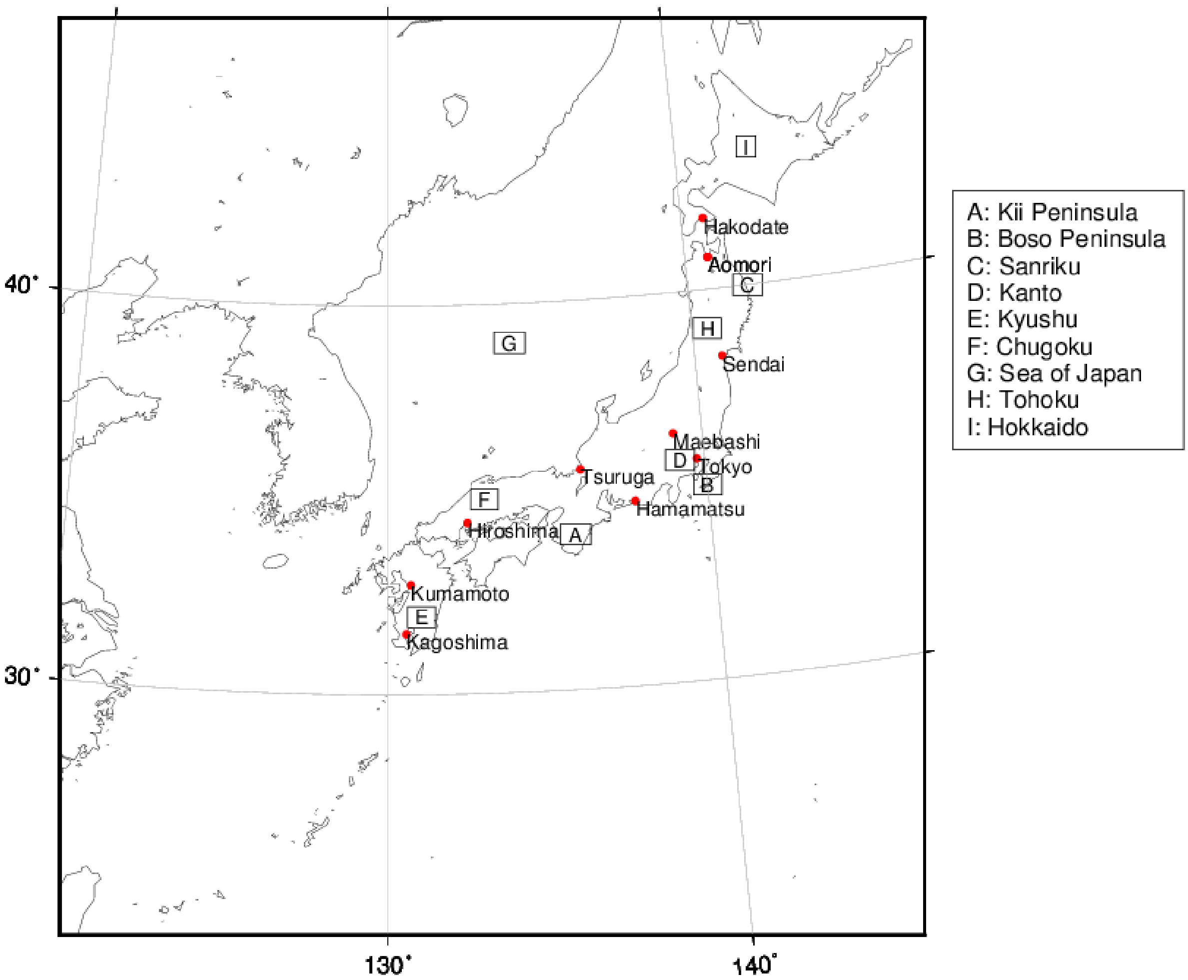

Fig. 30 Names of geographical locations around Japan.

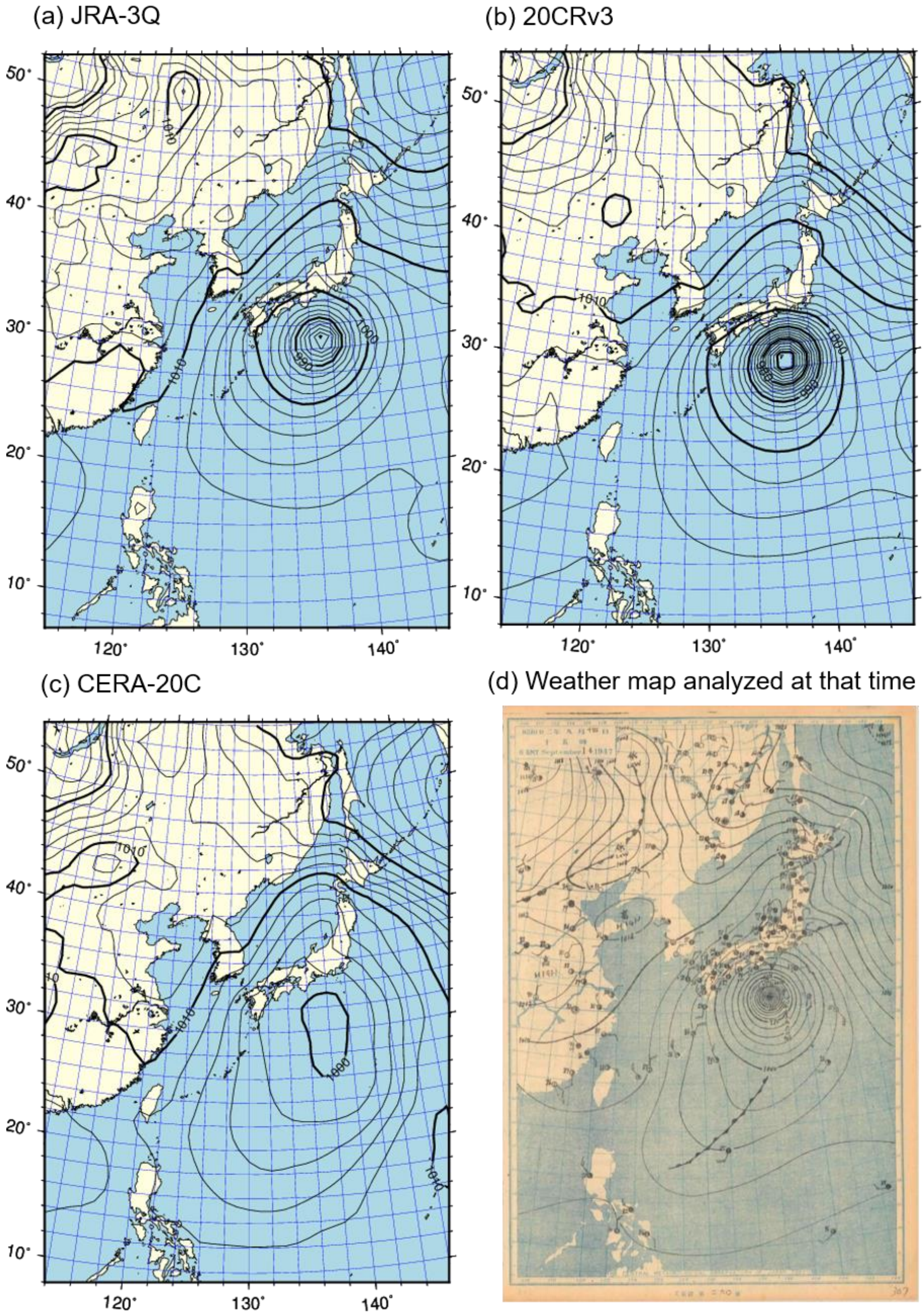

Fig. 31 Analysis field of mean sea level pressure (hPa) from (a) JRA-3Q, (b) 20CRv3, and (c) CERA-20C at 06 UTC on 14 September, 1947 and (d) the weather map analyzed at that time (the JMA weather chart).

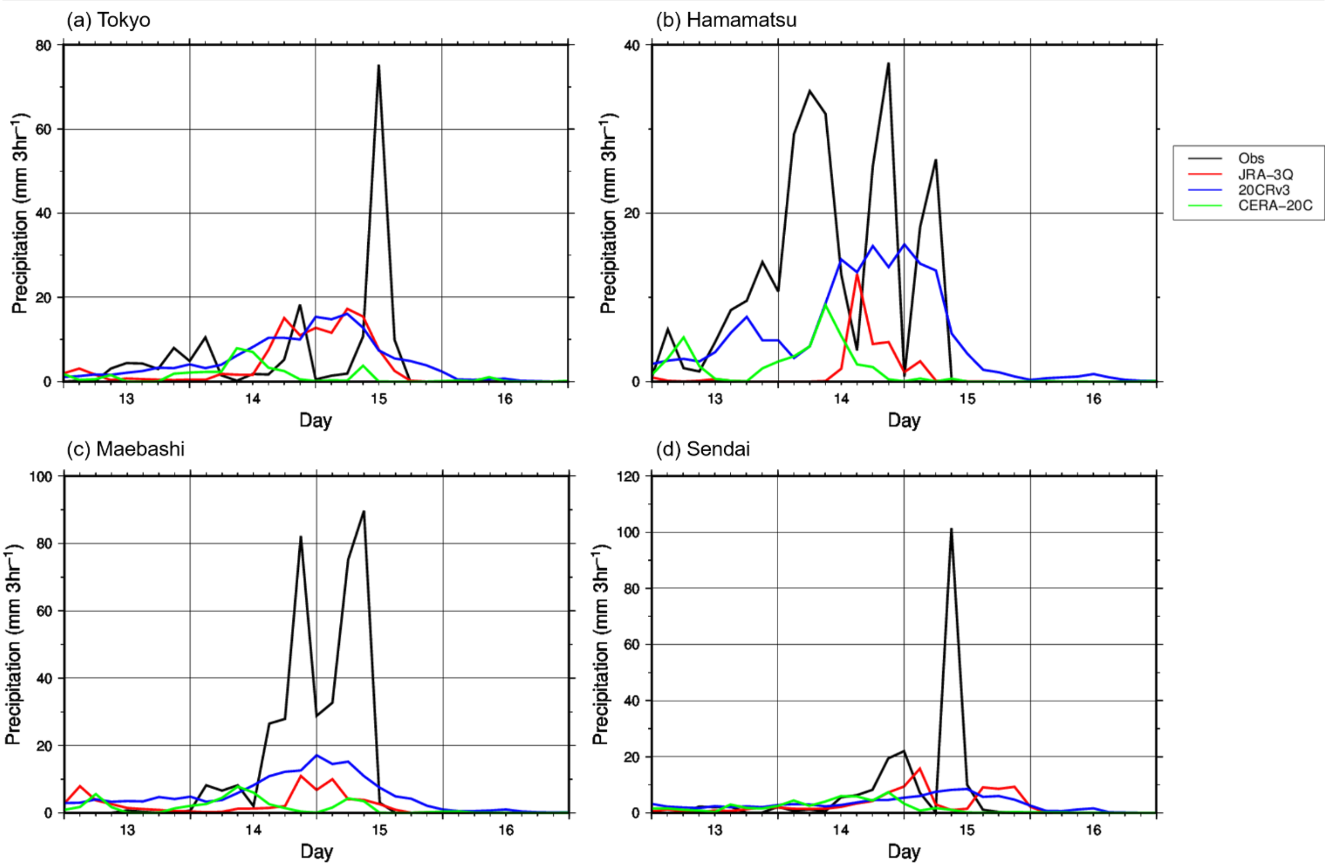

Fig. 32 Time series of three-hour accumulated precipitation at Tokyo (35°42'N, 139°45'E), Hamamatsu (34°45'N, 137°43'E), Maebashi (36°24'N, 139°04 E), and Sendai (38°16'N, 140°54'E) from 00 UTC on 13 September 1947 to 00UTC on 17 September 1947.

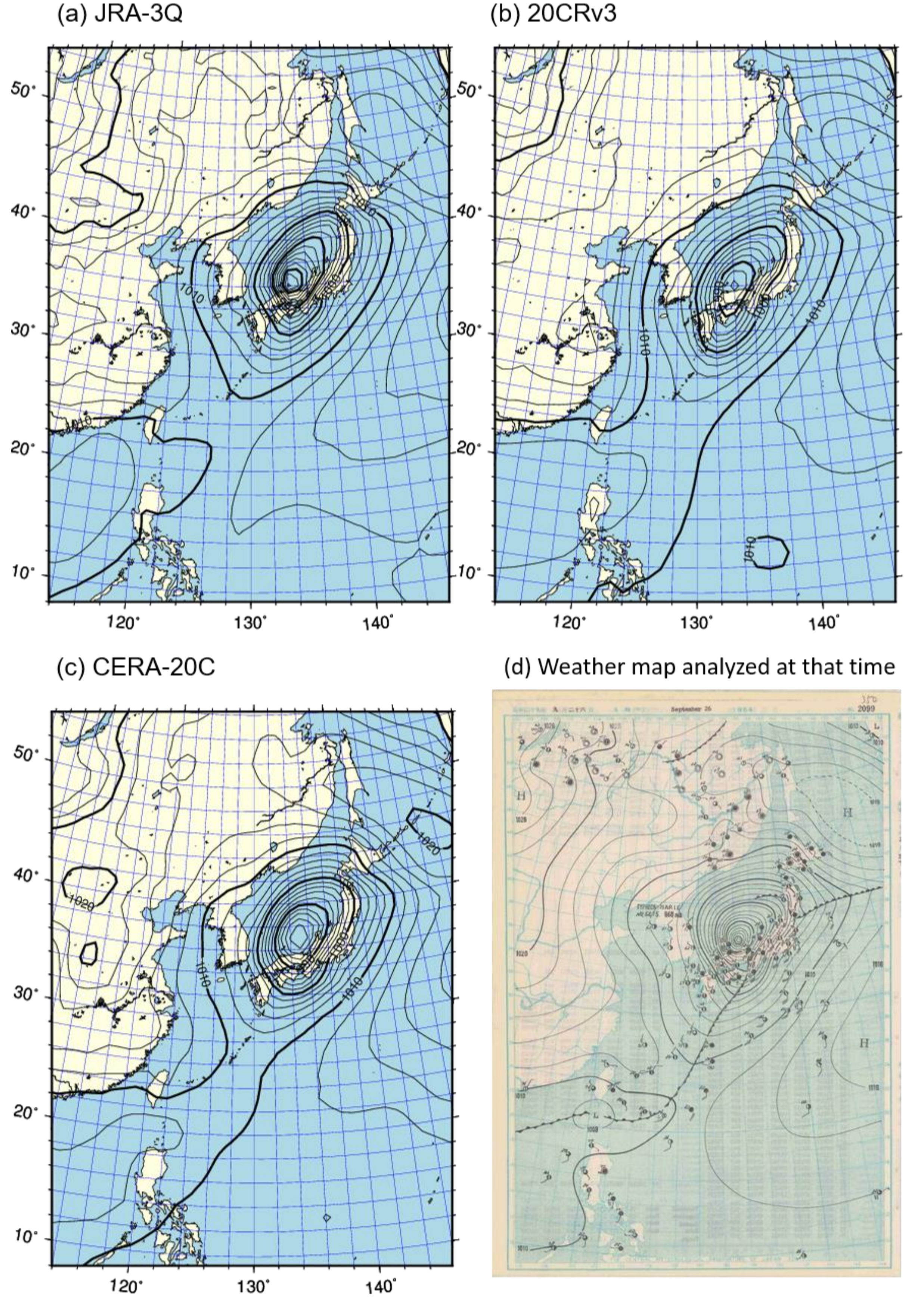

Fig. 33 Same as Fig. 31, but at 00 UTC on 26 September, 1954.

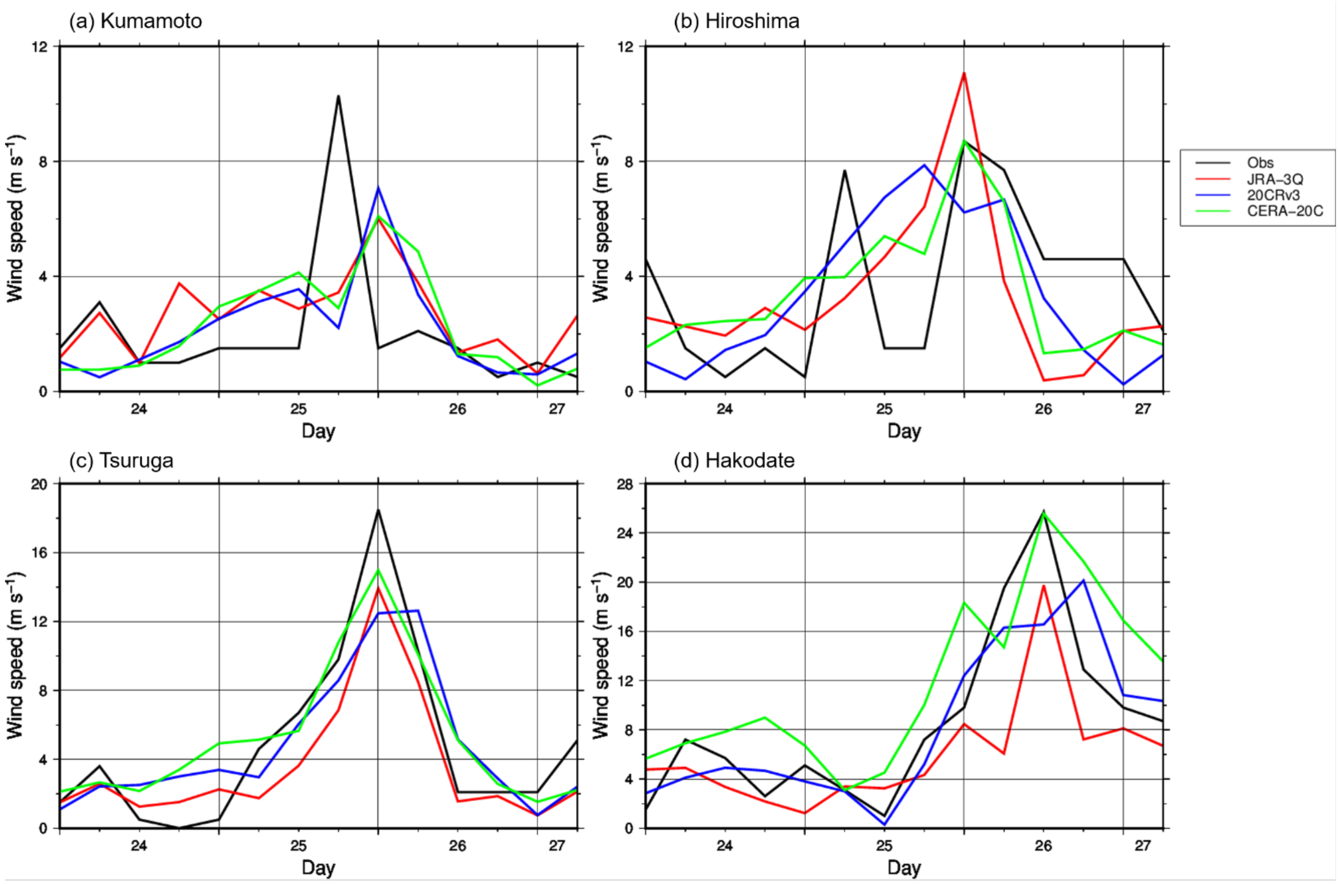

Fig. 34 Time series of 10 m wind speed (m s^{-1}) at Kumamoto (32°49'N, 130°42'E), Hiroshima (34°24'N, 132°28'E), Tsuruga (35°39'N, 136°04'E), and Hakodate (41°49'N, 140°45'E) from 00 UTC on 24 September 1954 to 06UTC on 27 September 1954.

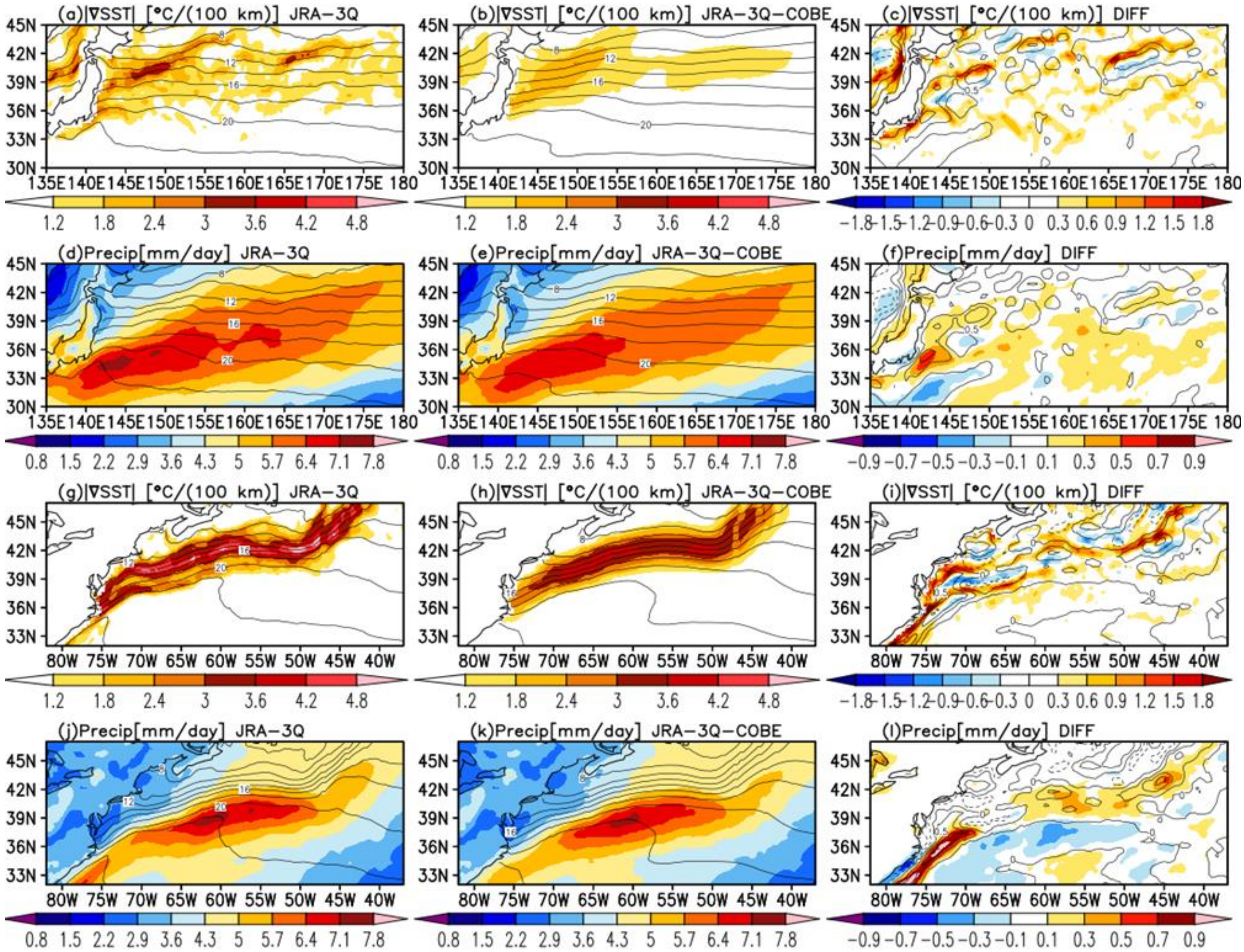

Fig. 35 Annual mean horizontal SST gradients (shaded, in units of °C (100km) $^{-1}$) and SSTs (contoured every 2°C) from (a, g) JRA-3Q, (b, h) JRA-3Q-COBE, and (c, i) JRA-3Q minus JRA-3Q-COBE, and annual mean total precipitation (shaded, in units of mm day^{-1}) and SSTs (contoured every 2°C) from (d, j) JRA-3Q, (e, k) JRA-3Q-COBE, and (f, l) JRA-3Q minus JRA-3Q-COBE over the (a–f) western North Pacific and (g–l) western North Atlantic domains, averaged over 1986–1990.

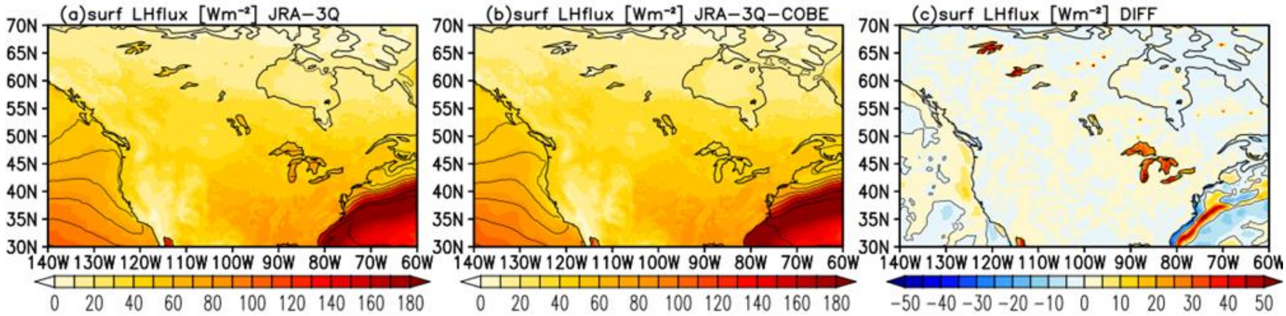

Fig. 36 Annual mean latent heat fluxes (shaded, in units of W m^{-2}) and SSTs (contoured every 2°C) from (a) JRA-3Q, (b) JRA-3Q-COBE, and (c) JRA-3Q minus JRA-3Q-COBE over northern North America, averaged over 1986–1990.

List of Tables

Table 9 Same as Table 8, but at the Earth’s surface.Values in the last line are total (net) energy fluxes averaged over the global ocean.

Table B1 Observational data sources for JRA-3Q. Observations shown in plain cells were added, recalibrated, or reprocessed after JRA-55, whereas those in shaded cells are the same as the ones used in JRA-55.

Table 1 Data assimilation systems used for JRA-55 and JRA-3Q.

	JRA-55	JRA-3Q
Analysis period	From 1958 onward	From September 1947 onward
Base system	The JMA operational system as of December 2009 (JMA 2007, 2013)	The JMA operational system as of December 2018 (JMA 2019)
Horizontal resolution	TL319 (~55km)	TL479 (~40km)
Vertical levels	Surface and 60 levels up to 0.1hPa (Iwamura and Kitagawa 2008, Nakagawa 2009)	Surface and 100 levels up to 0.01hPa (Kawai et al. 2013)
Analysis scheme	4D-Var with the T106 inner resolution	4D-Var with the TL319 resolution (Kadowaki and Yoshimoto 2012)
Radiosonde temperature bias correction	Until 2006: RAOBCORE V1.4 (Haimberger et al. 2008) From 2007 onward: RAOBCORE V1.5 (Haimberger et al. 2012) ・ based on comparison with	RISE (RICH with solar elevation dependence) v1.7.2 (Haimberger et al. 2012) ・ based on comparison with surrounding stations ・ seasonal dependent (from

	ERA	1979 onward)
Radiative transfer model for satellite radiances	RTTOV-9.3 (Saunders 2008)	RTTOV-10.2 (Saunders et al. 2012) ・ Improved accuracy ・ Inclusion of GHGs variations
Land surface analysis	Offline SiB	Cycle of land surface forecast from the model
SST and sea ice	COBE-SST (1-degree) (Ishii et al. 2005)	Until May 1985: COBE-SST2 (1-degree) (Hirahara et al. 2014) From June 1985 onward: MGDSST (0.25-degree) (Kurihara et al. 2006)
Ozone	Until 1978: Climatology From 1979 onward: MRI-CCM1 (T42L68) (Shibata et al. 2005)	MRI-CCM2.1 (TL159L64) (Deushi and Shibata 2011) ・ Produced with the new model for the whole period

Table 2 Forecast models used for JRA-55 and JRA-3Q.

	JRA-55 JMA's GSM as of December 2009 (JMA 2007,2013)	JRA-3Q JMA's GSM as of December 2018 (JMA 2019)	Impact
Longwave radiation	Broad-band emissivity method with the diffusivity approximation Pre-computed transmittance tables (for important absorption bands in the stratosphere)	Two-stream absorption approximation Correlated k-distribution method (for important absorption bands in the stratosphere)	•Improved stratospheric temperature profile
Cloud radiation	Random overlap (shortwave)	Maximum-random overlap (shortwave) Revision of optical properties of cloud water droplets Introduction of cloud diagnostics for cumulus updraft regions	•Improved radiation budget
Aerosols	Land and sea types	Sulfate, black carbon, organic carbon, sea salt and mineral dust	•Improved radiation budget
Cumulus convection	Prognostic Arakawa-Schubert scheme	Prognostic Arakawa-Schubert scheme •Introduction of precipitation conversion rate in the updraft •Improved convective updraft model below cloud base •Improvement of melting and evaporating processes	•Improved heating profile •Improved precipitation distribution
Cloud	Smith scheme Stratocumulus: Kawai and Inoue (2006)	Smith scheme: improvement of cloud water amount computation Stratocumulus: addition of a new relative humidity threshold for occurrence Improved cloud ice sedimentation scheme	•Reduced dry bias in the mid troposphere •Suppressed excessive stratocumuli •Improved radiation budget
Surface boundary layer	Monin-Obukhov similarity theory •Noniterative	Monin-Obukhov similarity theory •Dimensionless gradient functions (Beljaars and Holtslag 1991)	•Reduced excessive sensible and latent heat fluxes

	parameterization (Louis 1979)		
Non-orographic gravity wave drag	Rayleigh friction (above 50 hPa)	Scinocca (2003)	•Improved representation of QBO
Land surface	SiB (Sellers et al. 1986; Sato et al. 1989a, 1989b) •T: 1 (layer), moisture: 3 •Snow: 1	Improved SiB •T and moisture: 7 •Snow: 4 (maximum)	•Improved representation of surface temperature diurnal cycle
Sea ice	Single-layer model representing complete open water or sea ice only	Four-layer model allowing partial sea ice	•Reduce cold bias in the polar regions

Table 3 Data sources for long-lived greenhouse gases.

Molecule	Period	Source
CO_2	-1983 1984-2016 2017-	CMIP6 Historical (Meinshausen et al. 2017) WDCGG (WMO 2018) CMIP6 SSP2-4.5 (O'Neill et al. 2016)
CH_4	-1983 1984-2016 2017-	CMIP6 Historical (Meinshausen et al. 2017) WDCGG (WMO 2018) CMIP6 SSP2-4.5 (O'Neill et al. 2016)
N_2O	-1979 1980-2016 2017-	CMIP6 Historical (Meinshausen et al. 2017) WDCGG (WMO 2018) CMIP6 SSP2-4.5 (O'Neill et al. 2016)
CFC-11, CFC-12, HCFC-22	-1954 1955-	CMIP6 Historical (Meinshausen et al. 2017) A1 scenario: 2014 (WMO 2014)

Table 4 Data counts and QC statistics for conventional data in JRA-55 and JRA-3Q for the year 2017.

Obs type	Parameter	Level	Ingested obs		Rejected obs(%)		Used obs(%)	
			JRA-55	JRA-3Q	JRA-55	JRA-3Q	JRA-55	JRA-3Q

Land stations	P	surface	27633329	27646844	1.30087	1.10344	24.2299	21.054
Airport observations	P (QNH)	surface	0	60853072	n/a	0.796814	n/a	2.6379
Commercial or research vessels	P	surface	1952550	1952544	4.06356	4.01891	19.5542	18.764
Buoys	P	surface	11215450	11198358	1.00004	0.873985	11.6376	11.4156
Upper-level	T	to 100hPa	7614262	7643602	4.11563	3.53773	37.2148	37.2515
Upper-level	T	100 to 1000hPa	15117018	15180530	2.91194	2.67066	33.4499	33.4879
Upper-level	u	to 100hPa	9976481	10006671	1.09327	1.03071	27.1379	27.112
Upper-level	u	100 to 1000hPa	13532896	13585534	1.70262	1.43679	35.3985	35.5194
Upper-level	Rh	100 to 1000hPa	14567834	14630915	0.811624	0.867465	23.3093	23.3497
Aircraft	u	100 to 1000hPa	107904282	107904513	1.03543	0.853955	10.176	10.1617
Profiler (Japan)	u	100 to 1000hPa	21558003	21608191	7.50359	7.0326	0.766736	0.770985
Profiler (Europe)	u	100 to 1000hPa	9280095	9280326	1.20878	1.08609	0.92068	0.921433

Table 5 Microwave temperature sounding channels used in JRA-3Q. Channels shown in plain cells were added in JRA-3Q, whereas those in shaded cells are the same as the ones used in JRA-55.

	MSU	AMSU-A	ATMS
Clear sky ocean	2–4	4–14	6–9
Cloudy ocean	3–4	7–14	8–9
Rainy ocean	3–4	9–14	

Clear sky land/coast/sea-ice	4	6–14	7–9
Rainy or cloudy land/coast/sea-ice	4	9–14	

Table 6 Microwave humidity sounding channels used in JRA-3Q. Channels shown in plain cells were added in JRA-3Q, whereas those in shaded cells are the same as the ones used in JRA-55.

	SSM/T-2	AMSU-B/MHS	SSMIS	ATMS	SAPHIR	GMI
Clear sky ocean	3–5	3–5	9–11	18–22	1–6	12–13
Cloudy ocean	3–4	3–5				
Clear sky land/coast/sea-ice		3-5		18–22		

Table 7 Tropical cyclone information used in JRA-3Q.

Area	Period covered	Data providing agencies
Western North Pacific	1947 – 1950	NCDC
(100° E – 180° E, 0° N – 90° N)	1951 – 2012	JMA
	Dec 2012 – Apr 2013	TCAC Tokyo

	May 2013 – 2021	JMA
	2022 –	TCAC Tokyo
Arabian Sea and Bay of Bengal	1947 – 1976	UCAR
(10° E – 100° E, 0° N – 90° N)	1977 – 2012	JTWC
	Dec 2012 – Apr 2013	TCAC New Delhi
	May 2013 – 2021	JTWC
	2022 –	TCAC New Delhi
Central North Pacific	1947 – 1949	(Not available)
(180° W – 140° W, 0° N – 90° N)	1950 – 2012	NHC/NOAA
	Dec 2012 – Apr 2013	TCAC Honolulu
	May 2013 – 2021	NHC/NOAA
	2022 –	TCAC Honolulu
North Atlantic, Caribbean Sea and	1947 – 2012	NHC/NOAA
Gulf of Mexico plus eastern North	Dec 2012 – Apr 2013	TCAC Miami
Pacific	May 2013 – 2021	NHC/NOAA
(140° W – 10° E, 0° N – 90° N)	2022 –	TCAC Miami
South-west Indian Ocean	1947 – 1980	UCAR
(0° E – 90° E, 90° S – 0° S)	1981 – 2012	JTWC
	Dec 2012 – Apr 2013	TCAC La Réunion

	2013 – 2021	Météo-France
	2022 –	TCAC La Réunion
Seas surrounding Australia,	1947 – 1980	UCAR
Indonesia and Papua New Guinea	1981 – 2012	JTWC
and the eastern Indian Ocean	Dec 2012 – Apr 2013	Australian Bureau of Meteorology
(90° E – 160° E, 90° S – 0° S)	May 2013 – 2021	JTWC
	2022 –	TCWC-Melbourne
Central and western tropical Pacific	1947 – 1980	UCAR
(160° E – 120° W, 25° S – 0° S)	1981 – 2012	JTWC
	Dec 2012 – Apr 2013	TCAC Nadi
	May 2013 – 2021	JTWC
	2022 –	TCAC Nadi
Central and western South Pacific	1947 – 1980	UCAR
(160° E – 120° W, 90° S – 25° S)	1981 – 2012	JTWC
	Dec 2012 – Apr 2013	TCAC Nadi
	May 2013 – 2021	Meteorological Service of New Zealand
	2022 –	TCAC Nadi

Table 8 Global means of the annual means of energy budgets at the TOA (W m^{-2}). Values from reanalyses (JRA-25, JRA-55, JRA-3Q, and ERA5) and CERES-EBAF are

calculated from monthly averaged products for the period 2002–2008. Values for W19 are from Forster et al. (2021) and Wild et al. (2015, 2019) and represent present-day climate conditions at the beginning of the 21st century with their uncertainty ranges in parentheses.

TOA	W19	JRA-25	JRA-55	JRA-3Q	ERA5	CERES-EBAF
Incoming solar radiation	340(340,341)	341	341	341	340	340
Reflected solar radiation	100(96,100)	95	100	97	98	99
Net absorbed solar radiation		246	241	244	243	241
Outgoing thermal radiation	239(236,242)	255	251	250	242	240
Net radiation (down)(R_T)	0.7(0.5,0.9)	-7.9	-10.0	-5.5	0.7	0.8

Table 9 Same as Table 8, but at the Earth's surface. Values in the last line are total (net) energy fluxes averaged over the global ocean.

The Earth's surface	W19	JRA-25	JRA-55	JRA-3Q	ERA5	CERES-EBAF
downward Solar radiation	185(179,189)	197	189	190	188	187
Upward Solar radiation	25(22,26)	25	26	23	24	23
Net Solar radiation (down)	160(154,166)	172	164	166	164	164
Solar absorbed atmosphere	80(74,91)	75	77	78	79	77
Downward Thermal radiation	342(338,348)	327	338	340	340	345
Upward Thermal radiation	398(394,400)	399	400	400	398	399
Net Thermal radiation (up)		72	62	60	58	53
Sensible heat flux	21(15,25)	20	20	21	17	
Latent heat flux	82(70,85)	91	93	89	85	
Net energy flux (down)(Fs)	0.6(0.2,1.0)	-11.6	-11.2	-4.4	4.1	
Atmosphere net (Total energy Input=R_T-Fs)		3.7	1.2	-1.1	-3.3	
Net energy flux over ocean (down)	0.8(0.4,1.2)	-17.0	-15.9	-6.5	5.5	

Table B1 Observational data sources for JRA-3Q. Observations shown in plain cells were added, recalibrated, or reprocessed after JRA-55, whereas those in shaded cells are the same as the ones used in JRA-55.

Data supplier	Data type and suppliers' identifiers	Period	Reference
Conventional data			
NOAA/NCEI	ICOADS R3.0	Sep 1947 - Dec 1957	Freeman et al. (2017)
	IGRA V2	Sep 1947 - Dec 1957	doi:10.7289/V5X63K0Q
NOAA/CIRES	ISPD V4	Sep 1947 - Dec 1957	doi:10.5065/9EYR-TY90
The Met Office Hadley Centre	HadISD v3.1.0.201911p	Sep 1947 - Dec 1957	Dunn (2019)
NCAR	CHUAN V1.7 (stations in Japan only)	Sep 1947 - Dec 1957	doi:10.5065/AHPM-FC10
	Snow depths from USA	Nov 1957 - Aug 2011	doi:10.5065/B6MM-RS76
ECMWF		Jan 1958 - Aug 2002	Uppala et al. (2005)
JMA		Jan 1961 -	
	Radiosondes from Japan	Sep 1947 - Oct 1947	Digitized from monthly reports (Central Meteorological Observatory 1948)
	Dropsondes around Typhoon Vera (1959)	21 - 26 Sep 1959	Digitized from JMA (1961)
	GAME and SCSMEX	Apr 1998 - Oct 1998	Lau et al. (2000), Yasunari (2001)
M. Ishii at MRI	Near-surface observations (Wakkanai, Sapporo, Hakodate, Niigata, Tokyo, Kobe, Shionomisaki, Fukuoka, and Kaboshima in Japan)	Sep 1947 - Dec 1957	Digitized from original observation registers
H. Kamahori at MRI	Radiosondes from Tateno in Japan	Sep 1947 - Dec 1949	JSPS KAKENHI(S) 26220202 Digitized from original observation registers
M. Yamanaka	Radiosondes from Indonesia	Nov 1991 - May 1999	Okamoto et al. (2003)
RIHMI	Snow depths from Russia	Jan 1950 - Dec 2008	http://meteo.ru/english/climate/snow.php
Monthly Surface Meteorological Data in China	Snow depths from China	Jan 1971 - Dec 2006	Digitized from printed matters
IMH	Snow depths from Mongolia	Jan 1975 - Dec 2007	
Tropical cyclone information			
NOAA/NCEI	IBTrACS v03r05	Sep 1947 - Dec 2012	Knapp et al. (2010)
	IBTrACS v04	May 2013 - Dec 2021	
JMA	Best tracks in the western North Pacific	Feb 1951 - Dec 2012 May 2013 - Dec 2021	https://www.jma.go.jp/jma/jma-eng/jma-center/rsmc-hp-pub-eg/trackarchives.html
	Tropical cyclone information in the western North Pacific	Dec 2012 - Apr 2013 Jan 2022 -	
	Tropical cyclone advisories from TCACs (Honolulu, La Réunion,	Dec 2012 - Apr 2013 Jan 2022 -	https://community.wmo.int/en/activity-

	Miami, Nadi, New Delhi) and TCWC (Melbourne)		areas/aviation/hazards/tropical-cyclones https://community.wmo.int/en/tropical-cyclone-regional-bodies
Zenith total delays from the ground-based GNSS			
Y. Shoji at MRI	Reprocessed zenith total delays from the ground-based GNSS	Jan 1995 - Aug 2014	
JMA		Sep 2014 -	
Satellite radiances			
ECMWF	VTPR	Jan 1973 - Feb 1979	Uppala et al. (2005)
	HIRS and SSU	Nov 1978 - Dec 2001	
	AMSU-A	Aug 1998 - May 2003	
NOAA/NCDC	SSM/I	Jun 1987 - Dec 2004	
NOAA/NCEI	MSU CDR V1.0	Nov 1978 - Dec 2006	doi:10.7289/V51Z429F
NOAA/CLASS	AMSU-A	Aug 1998 - Dec 2012	https://www.avl.class.noaa.gov/saa/products/search?datatype_family=TOVS
	SSM/I	Jul 1987 - Dec 2012	https://www.avl.class.noaa.gov/saa/products/search?datatype_family=DMSP
JMA	AIRS	Jul 2008 - Dec 2020	
	IASI	Jul 2008 -	
	CrIS	May 2015 -	
	SSM/I	Mar 2006 - Apr 2021	
	SSMIS	Jun 2012 -	
	AMSR2	Sep 2016 -	
	GMI	May 2017 -	
	MWRI	Nov 2016 - Aug 2019	
	WindSat	Sep 2020 - Oct 2020	
	AMSU-A and MHS	Jun 2003 -	
	ATMS	Nov 2016 -	
	SAPHIR	Jul 2014 - Jan 2022	
	CSR	Jun 2005 -	
JMA/MSC	Reprocessed CSRs from *GMS-5*, *GOES 9*, *MTSAT-1R*	Jul 1995 - Dec 2009	
JAXA	Recalibrated TMI V05A (corresponded to V8)	Feb 1998 - Apr 2015	https://www.eorc.jaxa.jp/GPM/en/archives_v6.html
	Recalibrated AMSR-E V4.400.400	Jun 2002 - Oct 2011	https://www.eorc.jaxa.jp/AMSR/datacatalog/tb/index_en.html
	Recalibrated AMSR2 V2.220.220	Jul 2012 - Aug 2016	https://www.eorc.jaxa.jp/AMSR/datacatalog/tb/index_en.html
	Recalibrated GMI V05A	Mar 2014 - May 2017	https://www.eorc.jaxa.jp/GPM/en/archives_v6.html
EUMETSAT	SSM/T-2, AMSU-B, MHS FCDR v4.1	Jul 1994 - Dec 2017	Hans et al. (2019)
	Reprocessed *Meteosat-7* CSR	May 2000 - Dec 2000	https://navigator.eumetsat.int/product/EO:EUM:DAT:MFG:CSR1
	Meteosat CSR	Jan 2001 - Aug 2009	https://navigator.eumetsat.int/product/EO:EUM:DAT:MFG:CSR-IODC https://navigator.eumetsat.int/product/EO:EUM:DAT:MSG:CSR

EUMETSAT CM SAF	SSM/I,SSMIS FCDR E3	Jul 1987 - Dec 2015	doi:10.5676/EUM_SAF_CM/FCDR_MWI/V003
AMV			
ECMWF	Meteosat, GMS, GOES	Jan 1979 - Jan 1996	Uppala et al. (2005)
JMA	Meteosat, GOES, Himawari	Jan 2001 -	
	AVHRR, MODIS	Jun 2004 -	
JMA/MSC	Reprocessed GMS	Jan 1979 - Nov 1979	
	Reprocessed *GMS-3* to *-4*	Mar 1987 - Jun 1995	
	Reprocessed *GMS-5*, *GOES 9*, MTSAT	Jun 1995 - Jul 2015	Abe et al. (2018)
EUMETSAT	Reprocessed *Meteosat-2* to *-7*	May 1982 - Dec 2000	van de Berg et al. (2002)
	Meteosat-5 to *-7*	Jan 2001 - Feb 2001	
CIMSS	Reprocessed GOES	Jan 1995 - Jul 2015	Wanzong et al. (2014)
Scatterometer ocean surface winds			
EUMETSAT OSI SAF	ERS/AMI CDR	Mar 1992 - Jan 2001	doi:10.15770/EUM_SAF_OSI_0009
	QuikSCAT/SeaWinds CDR	Jul 1997 - Nov 2009	doi:10.15770/EUM_SAF_OSI_0002
	Metop-A/ASCAT CDR	Jan 2007 - Mar 2014	doi:10.15770/EUM_SAF_OSI_0006
JMA	Metop/ASCAT	Apr 2014 -	
GNSS-RO bending angles			
EUMETSAT ROM SAF	CHAMP CDR v1.0	Sep 2001 - Sep 2008	doi:10.15770/EUM_SAF_GRM_0004
	COSMIC CDR v1.0	Apr 2006 - Dec 2016	doi:10.15770/EUM_SAF_GRM_0003
	Metop CDR v1.0	Oct 2006 - Dec 2016	doi:10.15770/EUM_SAF_GRM_0002
	Metop ICDR	Jan 2017 - Jul 2019	doi:10.15770/EUM_SAF_GRM_0006
	GRACE CDR v1.0	Feb 2007 - Dec 2016	doi:10.15770/EUM_SAF_GRM_0005
JMA	COSMIC,Metop,GRACE, TerraSAR-X,TanDEM-X	Jan 2017 -	